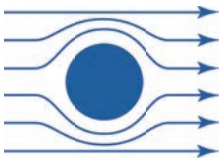

TECHNISCHE UNIVERSITÄT MÜNCHEN

WALTHER-MEISSNER-INSTITUT FÜR TIEF-TEMPERATURFORSCHUNG

BAYERISCHE AKADEMIE DER WISSENSCHAFTEN

Magnon-Phonon Coupling in Ferromagnetic Thin Films

Diploma thesis

Matthias Pernpeintner

Advisor: PD Dr. Sebastian T. B. Gönnenwein

Garching, October 2012

Contents

Introduction

Since the famous experiment by Stern and Gerlach [1, 2] was performed for the first time in 1922, the *spin* of electrons and nuclei has been subject to extensive experimental and theoretical investigation. The proof of the spin-statistics theorem by Pauli in 1940 [3] and the discovery and determination of the anomalous magnetic moment of the electron [4, 5] in the 1950s are only two examples of important contributions to the understanding of spin and spin-related phenomena, which also have had an enormous impact on physics in general.

Besides, spin-related physics has become more and more relevant in application and industry: Nuclear Magnetic Resonance (NMR), for example, first realized in 1946 by Bloch [6, 7] and Purcell [8], is nowadays an important tool for the imaging of organs and tissue in medical diagnosis as well as for the non-destructive material analysis in applied science. The giant magnetoresistance (GMR) effect, discovered by Grünberg [9] and Fert [10] in 1988, is exploited in today's hard disks to read out large amounts of data efficiently.

In recent years, the fields of *spin electronics* (short: *spintronics*), *spin caloritronics* and *spin mechanics* have been established, which deal with the systematic control of electron/nucleon spins via electric/magnetic fields, temperature gradients and elastic properties of solids [11–14]. A detailed understanding of the coupling of spins to their environment and the development of distinct controlling mechanisms could be the basis for a fundamental change in information technology, where data processing, transfer and storage are based on electron spins instead of charges [15]. This would enable further miniaturization of computing devices involving increasing computing power and storing capacities as well as a reduction in energy consumption and heat generation.

The present thesis deals with a particular issue of spin mechanics, namely the coupling between quantized lattice vibrations, i. e. *phonons*, and coherent spin excitations in a ferromagnet, called *magnons*. This *magnon-phonon coupling* was studied using hybrid devices which consist of a piezoelectric crystal onto which a ferromagnetic thin

film was deposited. On the surface of the piezoelectric crystal, surface acoustic waves (SAWs) are excited, which induce radio-frequency strains in the ferromagnetic film. These strains interact with the magnetization in the FM via magnetoelastic coupling and excite a so-called *acoustically driven ferromagnetic resonance* (ADFMR) [16, 17]. In this thesis, the coupling between SAW and magnetization was studied experimentally and theoretically.

Chapter 1 gives an analytical description of the SAW propagation on piezoelectric crystals. It is shown that the type of surface wave is determined by the material properties as well as by the surface cut direction of the used crystal. Moreover, we demonstrate that it is possible to excite different SAW types on one and the same crystal, which can be distinguished by their propagation speed.

Chapter 2 presents three modelling approaches to ADFMR, based on an effective field ansatz which considers magnetoelastic coupling via its contribution to the free-enthalpy density of the FM. These models differ in their range of validity as well as in their numerical complexity. Besides, it is shown that ADFMR qualitatively differs from conventional FMR [18, 19].

Chapter 3 deals with the experimental investigation of ADFMR. We measure the change in complex transmission due to ADFMR as a function of orientation and strength of the external static magnetic field for different frequencies. We use different surface waves types to excite ADFMR and compare their characteristic signatures. It is shown that the presented ADFMR models are consistent with one another and able to quantitatively describe the experimental results.

Besides the experimental and theoretical investigation of ADFMR, preliminary work for future ADFMR experiments with SAW resonators has been done. Resonators for surface acoustic waves are well-known and have been used, e. g., as narrowband frequency filters for about 40 years [20–24]. Yet, we show that for our purposes it is necessary to have a possibility to in-situ tune the resonator, which means to change its acoustic length by an external control parameter. Thus, the so-called *flipchip* design was chosen, which allows to mechanically shift the reflectors of the resonator against each other. In Chapter 4, the working principle and the fabrication of the tuneable resonator and preliminary experiments are shown. Furthermore, the tuneable resonator is characterized and its functionality is demonstrated.

In Chapter 5, the obtained results are summarized and several ideas for further

studies of ADFMR and related phenomena are presented together with some preliminary calculations.

Finally, we would like to mention that the SAW experiments, together with the theoretical modelling – performed in collaboration with L. Dreher and M. Brandt at the Walter-Schottky-Institut of the Technical University Munich – have resulted in a manuscript submitted to Physical Review B [17].

Chapter 1

Surface acoustic waves on piezoelectric substrates

In this thesis, acoustically driven ferromagnetic resonance (ADFMR) [16] is investigated using different types of surface acoustic waves (SAWs) propagating on substrate/ferromagnetic thin film bilayers. Depending on the type of acoustic wave and the corresponding strains induced in the FM thin film, qualitatively different ADFMR signatures arise as will be shown in Chap. 3. Here, we first calculate the wave types propagating on the used piezoelectric crystals and determine the strains induced. The derivation hereby follows [25] and [23].

1.1 Equations of motion

We start with the most general form of the equations of motion for elastic deformation in a solid without external forces [25, 26]:

$$\rho \frac{\partial^2 u_i}{\partial t^2} = \sum_j \frac{\partial \sigma_{ij}}{\partial x_j}, \qquad i,j \in \{1,2,3\}, \tag{1.1}$$

with density ρ, elastic deformation u_i and stress tensor σ_{ij}. In a piezoelectric crystal, σ_{ij} is a function of the stiffness tensor c_{ijkl}, the strain components ε_{kl}, the piezoelectric tensor e_{ijk} and the electric field $\boldsymbol{E}$:

$$\sigma_{ij} = \sum_{k,l} c_{ijkl}\varepsilon_{kl} - \sum_k e_{kij}E_k \tag{1.2}$$

with

$$\varepsilon_{kl} = \frac{1}{2}\left(\frac{\partial u_k}{\partial x_l} + \frac{\partial u_l}{\partial x_k}\right). \tag{1.3}$$

The electric displacement $\boldsymbol{D}$ in a piezoelectric material is given by

$$D_i = \sum_j \epsilon_{ij} E_j + \sum_{j,k} e_{ijk}\varepsilon_{jk}, \tag{1.4}$$

where ϵ_{ij} denotes the dielectric tensor. As the velocity of elastic deformation propagation (i. e. the speed of sound) is about five orders of magnitude smaller than the speed of light, we can assume the electric field to be quasi-static so that it can be written as the gradient of a potential function ϕ:

$$\boldsymbol{E} = -\boldsymbol{\nabla}\phi. \tag{1.5}$$

Using Eqs. (1.2) and (1.5), the equation of motion (1.1) becomes

$$\rho\frac{\partial^2 u_i}{\partial t^2} = \sum_{j,k}\left[e_{kij}\frac{\partial^2\phi}{\partial x_j \partial x_k} + \sum_l c_{ijkl}\frac{\partial^2 u_k}{\partial x_j \partial x_l}\right]. \tag{1.6}$$

As we are dealing with insulating substrates, there are no free charges and Maxwell's equations give us $\operatorname{div}\boldsymbol{D} = 0$. Applying this to Eq. (1.4) leads to

$$\sum_{i,j}\left[\epsilon_{ij}\frac{\partial^2\phi}{\partial x_i \partial x_j} - \sum_k e_{ijk}\frac{\partial^2 u_j}{\partial x_i \partial x_k}\right] = 0. \tag{1.7}$$

Equations (1.6) and (1.7) yield four equations relating the four unknown quantities $\boldsymbol{u}$ and ϕ. Together with appropriate boundary conditions, this allows a complete description of the coupled acoustic and electrical wave in a piezoelectric solid.

1.2 Boundary conditions

In the following, the piezoelectric crystal is modelled as an anisotropic, piezoelectric medium with infinite extent in the x- and y-directions and a surface at $z = 0$. The half-space $z \leq 0$ is filled by the crystal, while $z > 0$ is vacuum.

In this model, appropriate boundary conditions have to be specified for the surface at $z = 0$. First, we have the mechanical boundary condition for a free surface, that

accounts for the fact that there are no stresses on the surface of the solid:

$$\sigma_{xz} = \sigma_{yz} = \sigma_{zz} = 0 \quad \text{at} \quad z = 0. \tag{1.8}$$

Second, for piezoelectric materials, an electrical boundary condition is necessary which defines the electrical field at the surface. Usually two qualitatively different cases are considered: First, a free surface, where the space above the substrate is assumed to be vacuum. As there are no free charges at the surface, the normal component of the electric displacement D_z has to be continuous. For $z \leq 0$, D_z is given by (1.4), while in the upper half-space (i. e. $z > 0$), $\epsilon = 1$ and therefore

$$D_z = -\epsilon_0 \frac{\partial \phi}{\partial z} \quad \text{for } z > 0. \tag{1.9}$$

The second case considered is the metallized-surface one: Here, we assume the piezoelectric half-space to be covered with an infinitely thin, perfectly conducting metal. In this case, the electrical potential is constant at the surface $z = 0$ and per definition set to zero:

$$\phi = 0 \quad \text{at} \quad z = 0. \tag{1.10}$$

1.3 Surface-confined plane-wave solutions

As we are particularly interested in surface wave solutions of Eq. (1.6) and (1.7), we make a plane-wave ansatz, which decays exponentially within the substrate. For convenience we choose a coordinate system such that $\boldsymbol{x}$ is along the SAW propagation direction, $\boldsymbol{z}$ is normal to the film plane and $\boldsymbol{y}$ is in the film plane so that (x, y, z) is a right-handed frame of reference. Then, the mentioned surface-confined plane-wave ansatz can be written as

$$\boldsymbol{u}(\boldsymbol{x}, t) = \boldsymbol{u}_0 \exp(i\gamma z) \exp(i\beta x - i\omega t) \tag{1.11}$$

$$\phi(\boldsymbol{x}, t) = \phi_0 \exp(i\gamma z) \exp(i\beta x - i\omega t). \tag{1.12}$$

Here, ω denotes the angular frequency and β the wave number of the SAW, which is assumed to be real. γ describes the z-dependence of the acoustic wave and is complex in general.

Using (1.11), we can specify the boundary condition (1.9) for the free-surface case.

As the electrical potential ϕ is continous at the surface $z = 0$, it has the form

$$\phi = \phi_0 f(z) \exp(i\beta x - i\omega t), \tag{1.13}$$

where the z-dependence is given by $f(z)$. In addition, $\phi(z > 0)$ satisfies Laplace's equation $\boldsymbol{\nabla}^2\phi = 0$ and has to vanish for $z = +\infty$, which results in $f(z) = \exp(-\beta z)$. Inserting this into Eqs. (1.13) and (1.9) gives

$$D_z = \epsilon_0 \beta \phi \quad \text{at } z = 0. \tag{1.14}$$

To find SAW solutions, the plane-wave ansatz (1.11) is substituted into the equations of motion (1.6) and (1.7), which form a homogeneous system of four equations in the four variables $\boldsymbol{u}$ and ϕ. Setting the determinant of coefficients $\mathcal{D}_1$ to zero gives a relation between γ and β. In general, $\mathcal{D}_1$ is a eighth-degree polynomial in γ, so there are eight complex solutions for γ, depending on the parameter β. As we are only interested in surface-confined wave solutions, we set the additional condition $\operatorname{Im}\gamma < 0$, which guarantees exponential decay of the acoustic wave for $z \to -\infty$ and excludes half of the found values. The remaining, valid solutions shall be labeled γ^α, with an upper greek index $\alpha \in \{1, 2, 3, 4\}$.

In order to get a SAW solution which meets the boundary conditions, a superposition ansatz is made:

$$\boldsymbol{u}_{\text{tot}}(\boldsymbol{x}, t) = \sum_\alpha A_\alpha \boldsymbol{u}^\alpha(\boldsymbol{x}, t) \tag{1.15}$$

$$\phi_{\text{tot}}(\boldsymbol{x}, t) = \sum_\alpha A_\alpha \phi^\alpha(\boldsymbol{x}, t). \tag{1.16}$$

The coefficients A_α have to be chosen such that (1.8) and (1.14) resp. (1.10) are satisfied. These conditions lead to another determinant $\mathcal{D}_2$ which has to be zero. $\mathcal{D}_2$, however, will be zero only if the correct value for β has been chosen in the plane-wave ansatz (1.11). So, solving $\mathcal{D}_2(\beta) = 0$ iteratively finally gives us a SAW solution which satisfies the equations of motion as well as the boundary conditions.

Having found the correct β, the SAW velocity is $v = \omega/\beta$ and the coefficients A_α can be determined by solving the linear equation system given by the boundary conditions (1.8) and (1.14) resp. (1.10).

1.4 Surface acoustic waves on YZ-$LiNbO_3$ and 36°YX-$LiTaO_3$

$LiNbO_3$ and $LiTaO_3$ are widely used in industrial SAW-based applications in the field of communication, signal processing and sensing. Both materials are piezoelectric and pyroelectric insulators, exhibit trigonal crystal symmetry and belong to the 3m point group [27,28]. Because of the anisotropy of $LiNbO_3$ and $LiTaO_3$, the crystal cut direction defines if and which acoustic wave can propagate on the surface of the crystal. To specify the crystal cut, the *crystal coordinate system* (X, Y, Z) is introduced, where $\boldsymbol{Z}$ is along the c-axis of the crystal, $\boldsymbol{X}$ is parallel to one of the a-axes and $\boldsymbol{Y}$ is such that (X, Y, Z) is orthogonal and right-handed. Y-cut $LiNbO_3$ – which means that the surface normal is parallel to $\boldsymbol{Y}$ – is known to support Rayleigh waves[1] along the Z-axis with a sound velocity of about 3488 m/s (see Fig. 1.1a) [30, 31]. The comparatively high coupling factor[2] $\kappa^2 = 4.5\%$ [30] between electrical and acoustic field allows the efficient excitation of surface acoustic waves via electrical fields applied to the crystal. Therefore $LiNbO_3$ is very well suited as a SAW-carrying crystal for frequency filters, Fourier convolvers, oscillators etc.

Apart from the well-known Rayleigh waves, there is a variety of other surface wave types as, e. g., Love waves or Bleustein-Gulyaev waves, as well as pseudo-surface or leaky surface waves [25]. One technologically interesting wave type is the *shear horizontal* (SH) wave, whose displacement is mainly in the surface plane and perpendicular to the propagation direction of the wave (see Fig. 1.1b). Shear waves are used for biosensing applications (see e. g. [32–34]) as they propagate also at interfaces to liquid media and are sensitive to the mechanical and electrical properties of the adjacent liquid. Shear horizontal waves can be excited, e. g., on ST-quartz [33], certain piezoelectric ceramics [35] and 36°Y-cut $LiTaO_3$[3], which has been used in the present work.

[1] As illustrated in Fig.1.1a, Rayleigh waves are characterized by a phase shift of $\pi/2$ between normal and longitudinal displacement component (u_z resp. u_x) and a vanishing transverse component u_y. Rayleigh waves are named after Lord Rayleigh, who first discovered them in 1885 [29].

[2] The electromechanical coupling coefficient κ^2 is a measure of the coupling between electrical and elastic part of the SAW [30]. If the SAW is excited using interdigital transducers (IDTs), as it is the case here, κ^2 determines the efficiency of the SAW excitation because IDTs directly couple to the electrical field of the SAW only.

[3] For 36°-rotated Y-cut X-propagating $LiTaO_3$, as it is commonly used, the relation between the crystal axes (X, Y, Z) and the sample coordinate system (x, y, z) is rather complicated and can be found in [36].

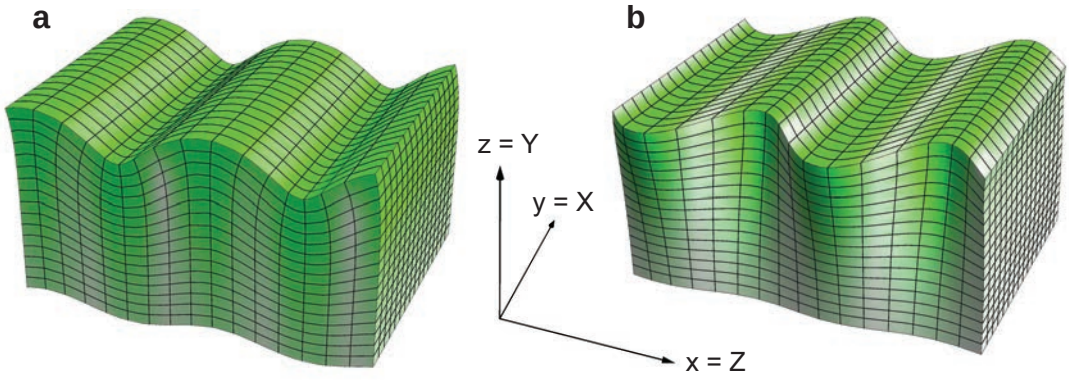

Figure 1.1: Schematic, highly exaggerated illustration of (**a**) Rayleigh and (**b**) shear-horizontal wave, propagating along the x-axis. The color code shows the real, i. e. physically relevant, part of the mechanical displacement, $|\mathrm{Re}(\boldsymbol{u})|$. The coordinate system shows the orientation of the crystal axes X, Y and Z and their mapping to the sample frame of reference (x, y, z) introduced in Sect. 1.2.

1.4.1 Material constants

The elastic properties of a solid are mainly characterized by the stiffness tensor c_{ijkl} and the density ρ. The dielectric tensor ϵ_{ij} describes the response of the solid to electromagnetic fields, while the piezoelectric tensor e_{ij} relates both acoustic and electrical fields. To simplify notation and reduce the number of indices, we use Voigt notation [37, 38] for the material tensors. Then, the stiffness tensor for trigonal 3m crystals has the form [31]

$$C = \begin{pmatrix} c_{11} & c_{12} & c_{13} & c_{14} & 0 & 0 \\ c_{12} & c_{11} & c_{13} & -c_{14} & 0 & 0 \\ c_{13} & c_{13} & c_{33} & 0 & 0 & 0 \\ c_{14} & -c_{14} & 0 & c_{44} & 0 & 0 \\ 0 & 0 & 0 & 0 & c_{44} & c_{14} \\ 0 & 0 & 0 & 0 & c_{14} & (c_{11} - c_{12})/2 \end{pmatrix}. \tag{1.17}$$

The piezoelectric tensor is given by

$$e = \begin{pmatrix} 0 & 0 & 0 & 0 & e_{15} & -e_{22} \\ -e_{22} & e_{22} & 0 & e_{15} & 0 & 0 \\ e_{31} & e_{31} & e_{33} & 0 & 0 & 0 \end{pmatrix}. \tag{1.18}$$

		$LiNbO_3$	$LiTaO_3$	
Density	ρ	4640	7454	kg/m^3
Elastic constants	c_{11}	2.03	2.328	$\times 10^{11}\,N/m^2$
	c_{12}	0.53	0.465	$\times 10^{11}\,N/m^2$
	c_{13}	0.75	0.836	$\times 10^{11}\,N/m^2$
	c_{14}	0.09	−0.105	$\times 10^{11}\,N/m^2$
	c_{33}	2.45	2.759	$\times 10^{11}\,N/m^2$
	c_{44}	0.60	0.949	$\times 10^{11}\,N/m^2$
Piezoelectric constants	e_{15}	3.774	2.64	C/m^2
	e_{22}	2.53	1.86	C/m^2
	e_{31}	0.194	−0.22	C/m^2
	e_{33}	1.32	1.71	C/m^2
Dielectric constants	ϵ_{11}	44.3	40.9	
	ϵ_{33}	27.9	42.5	

Table 1.1: Material constants for $LiNbO_3$ and $LiTaO_3$, taken from [27] and [39], respectively. As the piezoelectric tensor e_{ij} is not given explicitly in [27], it has been calculated using the relation $e_{ij} = d_{ik}c_{kj}$ from [26] (The d_{ik} are called *piezoelectric strain constants*).

Finally, the dielectric tensor is

$$\epsilon = \begin{pmatrix} \epsilon_{11} & 0 & 0 \\ 0 & \epsilon_{11} & 0 \\ 0 & 0 & \epsilon_{33} \end{pmatrix}. \tag{1.19}$$

In Tab. 1.1, literature values of the material parameters for $LiNbO_3$ and $LiTaO_3$ are listed.

All material constants are given in the crystal coordinate system (X, Y, Z) and have to be transformed into the sample frame of reference introduced in Sect. 1.3. Due to the simplified Voigt notation, specific transformation matrices have to be used for the tensors c_{ij} and e_{ij}, which can, e. g., be found in [26].

1.4.2 Rayleigh Waves on YZ-$LiNbO_3$

Using an implementation of the algorithm explained in Sect. 1.3 in *Mathematica* and the literature material constants from Tab. 1.1, displacements and strains of the

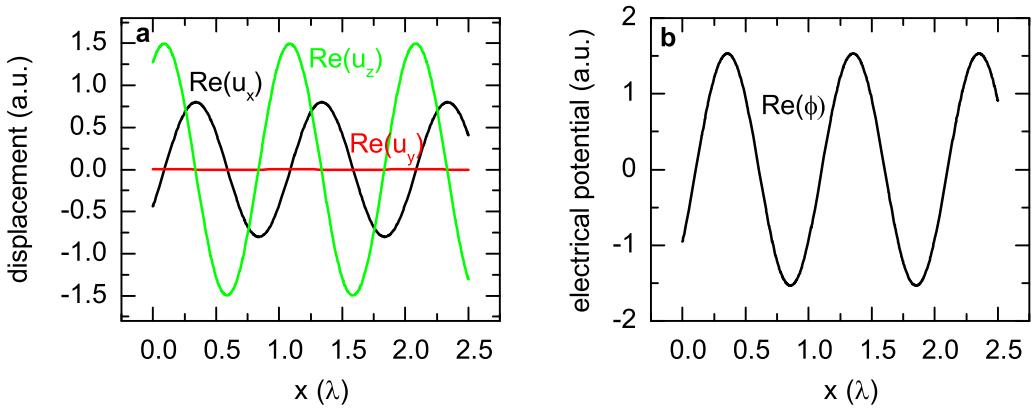

Figure 1.2: x-dependence of (**a**) displacement and (**b**) electrical potential of a Rayleigh wave propagating on YZ-$LiNbO_3$, assuming a metallized surface. λ is the SAW wavelength, and z was taken as zero. Here, the physically relevant real part of $\boldsymbol{u}$ and φ is plotted instead of the magnitude in order to show the phase shift between the u_i.

Rayleigh wave propagating on YZ-$LiNbO_3$ have been calculated. In Fig. 1.2, the mechanical displacement $\boldsymbol{u}$ and the electrical potential ϕ are plotted against the SAW propagation direction x, whereas Figs. 1.3 and 1.4 show $\boldsymbol{u}$ and ϕ as a function of the surface normal z for metallized and free surface boundary conditions, together with literature data from [25]. In x-direction, we see a sine oscillation with a phase shift of $\pi/2$ between the longitudinal (u_x) and normal (u_z) displacement. The transversal component of the displacement, u_y, is zero within numerical limits. In z-direction, we observe an exponential decay of displacement and potential on the scale of the wavelength λ, and a zero crossing of $|u_x|$ at $z \approx -\lambda/5$. Regarding $\mathrm{Re}(u_x)$ or $\mathrm{Im}(u_x)$ instead of its absolute value reveals that u_x changes sign at the mentioned point. This means that the motion of a single particle in the solid changes its rotation direction from clockwise (for $z > -\lambda/5$) to counterclockwise (for $z < -\lambda/5$), which can also be seen in Fig. 1.1.

Comparing literature data and calculation results, as shown in Figs. 1.3 and 1.4, yields full quantitative agreement.

Figures 1.3 and 1.4 illustrate the influence of the electrical boundary condition on the SAW, as they show the calculated $\boldsymbol{u}$ and ϕ for a metallized and free surface, respectively. As one can see, the change in $\boldsymbol{u}$ is comparatively small, whereas ϕ differs remarkably near the surface. Moreover, the sound velocity of the SAW decreases by

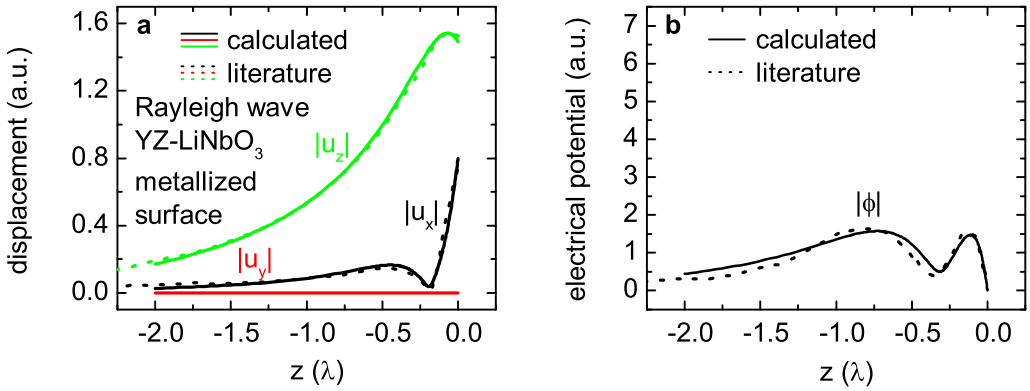

Figure 1.3: z-dependence of (**a**) displacement and (**b**) electrical potential of a Rayleigh wave propagating on YZ-LiNbO$_3$, assuming a metallized surface. The solid and dashed line show calculation results and literature data, respectively. λ is the SAW wavelength, $z = 0$ corresponds to the surface of the crystal.

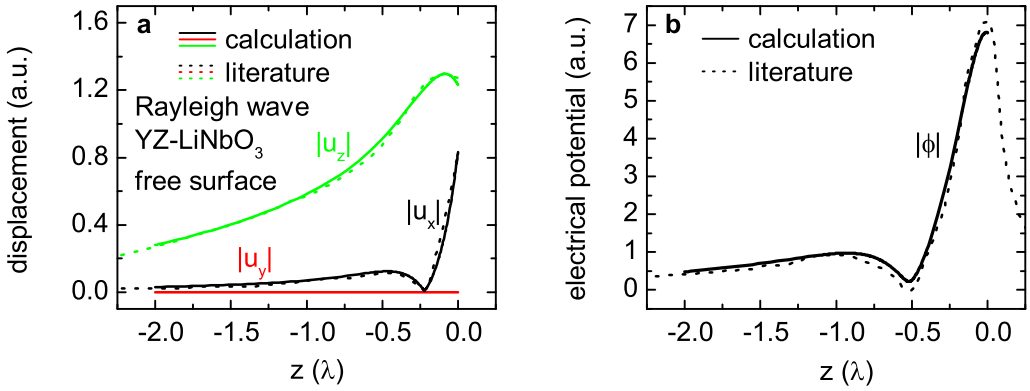

Figure 1.4: z-dependence of (**a**) displacement and (**b**) electrical potential of a Rayleigh wave propagating on YZ-LiNbO$_3$, assuming a free surface. The solid and dashed line show calculation results and literature data, respectively. λ is the SAW wavelength, $z = 0$ corresponds to the surface of the crystal.

		Rayleigh wave
sound velocity	v_{met}	3433 m/s
strains	ε_{xx}	1
	ε_{yy}	0
	ε_{zz}	$-0.33 - 0.09i$
	ε_{yz}	0
	ε_{xz}	$-0.05 - 0.19i$
	ε_{xy}	0

Table 1.2: Calculated sound velocity and strains for a Rayleigh wave on YZ-$LiNbO_3$ (metallized surface).

about 2.5%. The difference in the speed of sound Δv is crucial for the excitation of SAWs with interdigital transducers as $\kappa^2 = -2\Delta v/v$ [30].

Having calculated displacement and electrical potential of the SAW, we can substitute $\boldsymbol{u}_{\mathrm{tot}}$ and ϕ_{tot} given by Eqs. (1.15) and (1.16) into Eq. (1.3) to determine the strains induced by the SAW. The calculated values are listed in Tab. 1.2. In Fig. 1.5, the three non-vanishing strain components ε_{xx}, ε_{zz} and ε_{xz} are shown by a color code. If the (bulk) $LiNbO_3$ crystal is covered with a thin ferromagnetic film, these strains can be taken as an approximation of the strains in the FM film driving the magnetization precession via magnetoelastic coupling [16].

Comparing the calculated sound velocity to the literature value $v_{\mathrm{met}} = 3410\,\mathrm{m/s}$, which will be given in Tab. 3.2, shows the expected agreement.

1.4.3 Shear horizontal waves and Rayleigh Waves on 36°YX-$LiTaO_3$

According to [40], 36°Y-cut $LiTaO_3$ does support not only shear horizontal waves, but also Rayleigh waves, with a distinctly lower speed of sound and a much weaker coupling κ^2 between electrical and mechanical wave component. In sensing devices, the effects of this Rayleigh wave mode are usually neglected. Concerning the study of acoustically driven FMR (Chap. 3), however, 36°Y-cut $LiTaO_3$ allows to investigate FMR driven by two different SAW types in one and the same sample. In Sect. 2.1.2, we will see that the virtual driving field $\boldsymbol{h}$ of FMR is proportional to the strain induced by the acoustic wave, which is qualitatively different for Rayleigh and SH waves. So

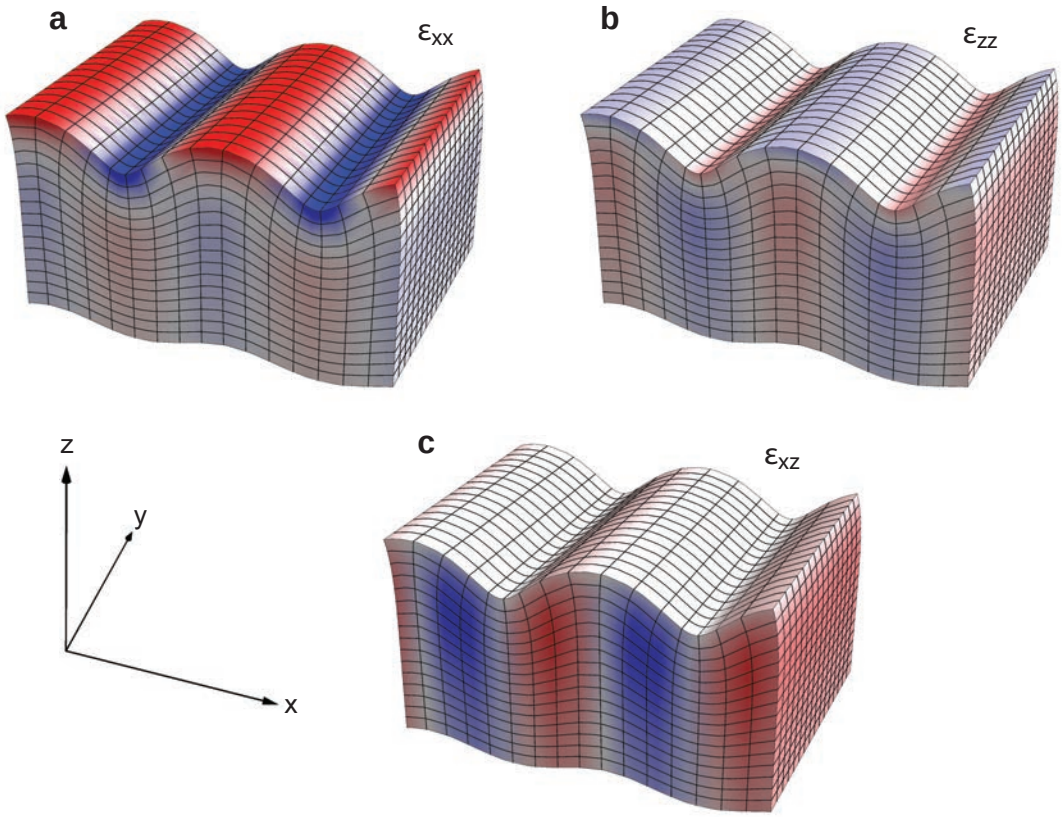

Figure 1.5: Three-dimensional plot of the dominant strain components induced by a Rayleigh wave on YZ-$LiNbO_3$. The propagation direction of the SAW is along the x-axis, $\boldsymbol{z}$ is the surface normal. The color code shows the real part of (**a**) ε_{xx}, (**b**) ε_{zz} and (**c**) ε_{xz}, where red and blue color denotes positive and negative strain, respectively. The scaling of the color code is the same for the three figures. Similar to Fig. 1.1, the displacement has been exaggerated strongly.

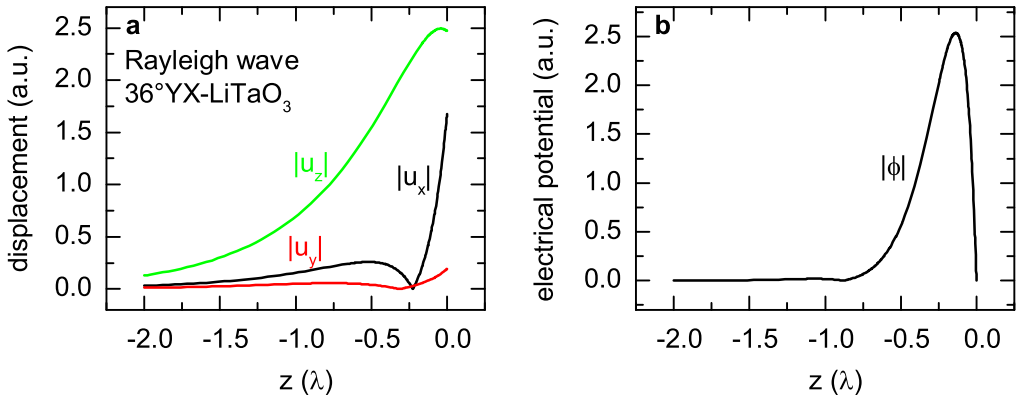

Figure 1.6: z-dependence of (**a**) displacement and (**b**) electrical potential of a Rayleigh wave propagating on 36°YX-$LiTaO_3$, assuming a metallized surface. λ is the SAW wavelength, $z = 0$ corresponds to the surface of the crystal.

we expect the signature of ADFMR to depend on the type of surface wave.

In Figs. 1.6 and 1.7, $\boldsymbol{u}$ and ϕ of both Rayleigh and SH wave are plotted as a function of z, assuming a metallized surface of the $LiTaO_3$ crystal. One can see that for the SH-wave case the u_y-component of the SAW dominates, accompanied by a small contribution of longitudinal and normal displacement. In the Rayleigh-wave case, the elastic part of the SAW, i. e. the displacements, looks quite similar to the Rayleigh wave on $LiNbO_3$, while the electrical potential differs remarkably (see Fig. 1.3). Of course, we do not expect a perfect agreement as the material constants of $LiNbO_3$ and $LiTaO_3$ differ considerably (cf. Tab. 1.1).

Regarding the calculated strains listed in Tab. 1.3, the shear strain ε_{xy} dominates in the SH wave case, whereas for the Rayleigh wave case ε_{xy} is small compared to the longitudinal strain ε_{xx}. For both wave types, we observe phase shifts close to $\pi/2$ or π between the dominant strain components. This can also be seen from Figs. 1.8 and 1.9, where the dominant strain components are plotted in a three-dimensional representation similar to Fig. 1.5.

The calculated strains as well as the displacements and the electrical potential shown in Figs. 1.6 and 1.7 demonstrate the differing character of Rayleigh and SH wave, which we will exploit in our ADFMR measurements.

Again, the comparison with the literature sound velocities given in Tab. 3.2 and with literature displacement calculations (see [40]) shows perfect agreement, which

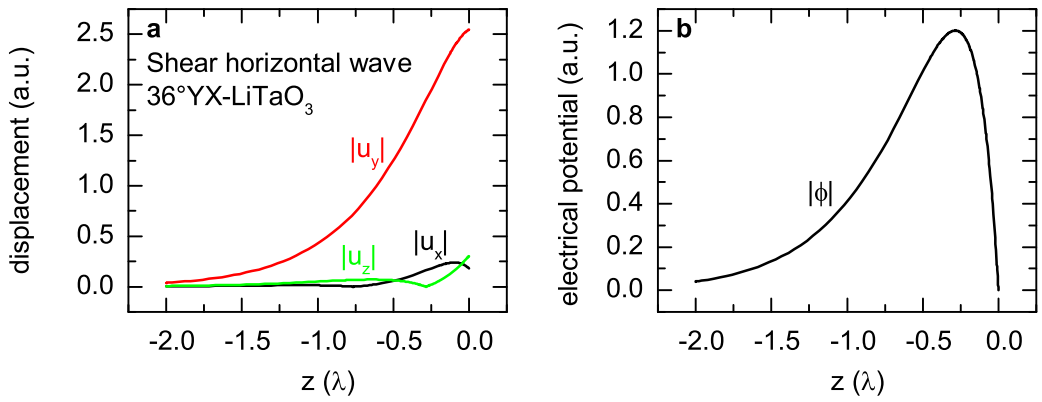

Figure 1.7: z-dependence of (**a**) displacement and (**b**) electrical potential of a SH wave propagating on 36°YX-$LiTaO_3$, assuming a metallized surface. λ is the SAW wavelength, $z = 0$ corresponds to the surface of the crystal.

		SH wave	Rayleigh wave
sound velocity	v_{met}	4108 m/s	3124 m/s
strains	ε_{xx}	$-0.14i$	1
	ε_{yy}	0	0
	ε_{zz}	$0.21i$	-0.12
	ε_{yz}	$0.05i$	-0.07
	ε_{xz}	0.03	0
	ε_{xy}	1	$0.06i$

Table 1.3: Calculated sound velocity and strains for SH and Rayleigh wave on 36°YX-$LiTaO_3$, assuming a metallized surface.

indicates the correctness of the used algorithms.

1.5 Summary

In this chapter, the basis for a fully quantitative description of ADFMR has been layed. We have presented a general theory of SAW propagation, which holds for any piezoelectric crystal and arbitrary crystal cut and which allows to calculate the mechanical displacement, the electrical potential and the strains induced by the SAW. The presented theory was applied to YZ-$LiNbO_3$ and 36°YX-$LiTaO_3$ and the differing

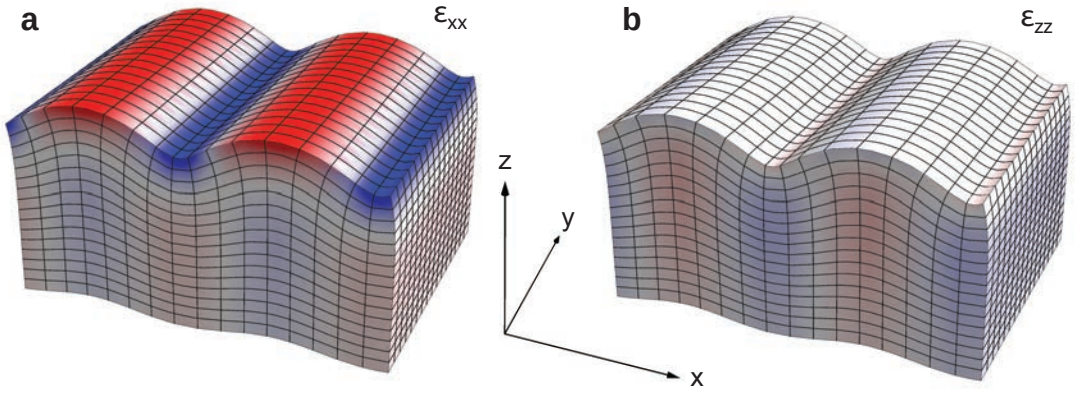

Figure 1.8: Three-dimensional plot of the dominant strain components induced by a Rayleigh wave on 36°YX-$LiTaO_3$. The propagation direction of the SAW is along the x-axis, $\boldsymbol{z}$ is the surface normal. The color code shows the real part of (**a**) ε_{xx} and (**b**) ε_{zz}, where red and blue color denotes positive and negative strain, respectively. The scaling of the color code is the same for both figures. Similar to Fig. 1.1, the displacement has been exaggerated strongly.

character of Rayleigh and shear-horizontal wave as well as the influence of the surface boundary condition – free or metallized surface – was demonstrated. Comparing the calculation results to literature values showed the expected agreement and proved the reliability of the presented theory and its implementation in *Mathematica*.

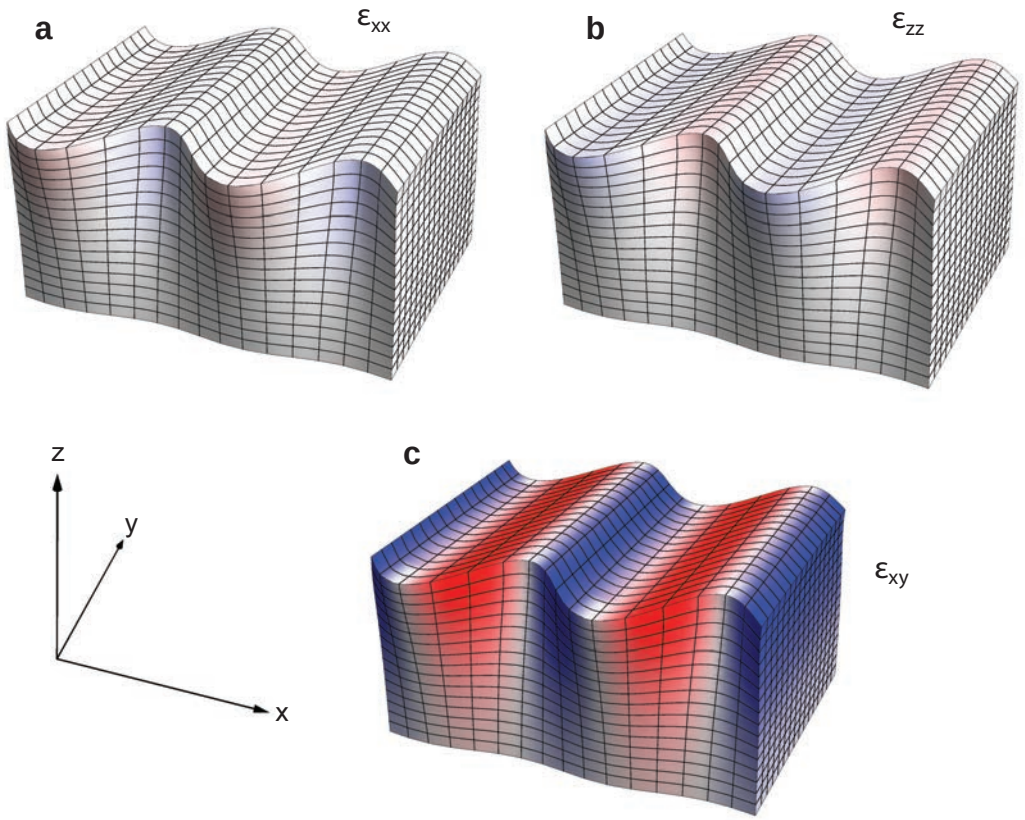

Figure 1.9: Three-dimensional plot of the dominant strain components induced by a shear-horizontal wave on 36°YX-$LiTaO_3$. The propagation direction of the SAW is along the x-axis, $\boldsymbol{z}$ is the surface normal. The color code shows the real part of (**a**) ε_{xx}, (**b**) ε_{zz} and (**c**) ε_{xy}, where red and blue color denotes positive and negative strain, respectively. The scaling of the color code is the same for the three figures. Similar to Fig. 1.1, the displacement has been exaggerated strongly.

Chapter 2

Modelling of acoustically driven FMR

In this chapter, three ways of describing acoustically driven FMR are presented. The first approach is based on the Landau-Lifshitz-Gilbert equation of motion for the magnetization in a ferromagnet, introduced by L. Landau and E. Lifshitz in 1935 [41] and modified by T. L. Gilbert in 2004 [42]. The second model extends this approach and takes into account the backaction of the magnetization precession in the ferromagnet on the SAW, which allows to calculate the change in SAW transmission due to ADFMR. Both models have been developed by L. Dreher and M. Weiler [16,17,43]. The discussion of these models in Secs. 2.1 and 2.2 follows [16] and [17].

The third approach to ADFMR combines the SAW propagation theory presented in Chap. 1 with the methods used in the backaction model in order to describe the magnetization dynamics in the ferromagnet coupled to the acoustic wave propagating in the ferromagnet/piezoelectric crystal hybrid. In this way, the damping effect of ADFMR on the SAW can be fully accounted for.

While the LLG model is comparatively simple but instructive to show the physics of ADFMR, the backaction model allows a more detailed description of the transmitted acoustic wave and is therefore more powerful than the LLG approach. The SAW model is an extension of the backaction model. It enlarges its range of validity and describes the full hybrid system consisting of FM and piezoelectric crystal, but is numerically expensive. For this reason, it is useful to consider all three presented approaches when modelling ADFMR.

2.1 Landau-Lifshitz-Gilbert approach

2.1.1 Landau-Lifshitz-Gilbert equation and free-enthalpy density

For a phenomenological description of acoustically driven FMR, we start from the well-known LLG equation [41, 42], which is the equation of motion for the magnetization in a ferromagnet (FM) and widely used in magnetization dynamics:

$$\partial_t \boldsymbol{m} = -\gamma \boldsymbol{m} \times \mu_0 \boldsymbol{H}_{\text{eff}} + a \boldsymbol{m} \times \partial_t \boldsymbol{m}. \tag{2.1}$$

Here, $\boldsymbol{m} = \frac{\boldsymbol{M}}{M_\text{s}}$ denotes the magnetization vector normalized to the saturation magnetization M_s, and γ and a are the gyromagnetic ratio and a phenomenological damping parameter, respectively. $\boldsymbol{H}_{\text{eff}}$ is the effective magnetic field, which exerts a force on the spins in the FM and in this way excites the magnetization precession. In the following, we derive this effective magnetic field $\boldsymbol{H}_{\text{eff}}$.

We begin by writing down the Gibbs free-energy density in the FM, considering elastic and magnetoelastic contributions. In absence of elastic strains, the Gibbs free-energy density of the FM – normalized to the saturation magnetization M_s – can be calculated using a macro-spin approach[1]:

$$G = -\mu_0 \boldsymbol{H} \cdot \boldsymbol{m} + B_\text{d} m_z^2 + B_\text{u} (\boldsymbol{m} \cdot \boldsymbol{u})^2 - \mu_0 \boldsymbol{H}_\text{ex} \cdot \boldsymbol{m}. \tag{2.2}$$

Here, $\boldsymbol{H}$ denotes the static external magnetic field, B_d represents the shape anisotropy of the ferromagnetic thin film, and B_u is the uniaxial in-plane anisotropy along the unit vector $\boldsymbol{u}$ [17, 43]. $\mu_0 \boldsymbol{H}_\text{ex}$ describes the exchange interaction between the electron spins which can be written as $\mu_0 \boldsymbol{H}_\text{ex} = D_\text{s} \Delta \boldsymbol{m}$ with the exchange stiffness D_s and the Laplacian operator $\Delta = \partial_x^2 + \partial_y^2 + \partial_z^2$ [19, 45]. In the following, we neglect the exchange interaction as its contribution to the free-enthalpy density can be shown to be small compared to the other terms in Eq. (2.2) (see Sect. 3.4.3).

The magnetoelastic contribution to the free-energy density is given by[2] [46]

$$G^\text{me} = b_1 \varepsilon_{ij} m_i m_j, \tag{2.3}$$

with the magnetoelastic coupling constant b_1 and the strain tensor $\varepsilon_{ij} = \frac{1}{2}\left(\frac{\partial u_i}{\partial x_j} + \frac{\partial u_j}{\partial x_i}\right)$,

[1] The *macro-spin* model describes a single-domain approximation of the FM, where the electron spins are assumed to all be aligned in parallel due to ferromagnetic exchange interaction (cf. [44]).
[2] Similar to Eq. (2.2), G^me has been normalized to the saturation magnetization M_s, so that $[G] = T$.

$i, j \in \{x, y, z\}$. Using the thermodynamic relation

$$\mu_0 \boldsymbol{H}_{\text{eff}} = -\boldsymbol{\nabla}_{\boldsymbol{m}} G^{\text{tot}}, \tag{2.4}$$

with $G^{\text{tot}} = G + G^{\text{me}}$ the sum of all relevant contributions to the free-energy density, we can calculate $\mu_0 \boldsymbol{H}_{\text{eff}}$ as a function of the strains ε_{ij} and the magnetization components m_i.

2.1.2 Magnetization precession and virtual driving field

Without a (radio-frequency) driving field, the magnetization is oriented in a way that G^{tot} is minimized. In polar coordinates, this equilibrium direction $\boldsymbol{m}_0$ is characterized by two angles ϕ_0 and θ_0. In the dynamic case, i. e. with a driving field, $\boldsymbol{m}$ precesses around its equilibrium direction. Throughout this thesis, we only consider small deviations from $\boldsymbol{m}_0$ [17].

It is convenient to define a new coordinate system (x_1, x_2, x_3), in which $\boldsymbol{m}_0$ is along the x_3-axis and the x_2-component of $\boldsymbol{m}$ lies in the film plane, as indicated in Fig. 2.1 [17]. Then, $\boldsymbol{m}$ can be written as:

$$\boldsymbol{m} = \underbrace{\begin{pmatrix} 0 \\ 0 \\ 1 \end{pmatrix}}_{\boldsymbol{m}_0} + \begin{pmatrix} m_1 \\ m_2 \\ 0 \end{pmatrix} + O(m_1^2, m_2^2). \tag{2.5}$$

The transformation matrix relating the two frames of reference (x, y, z) and (x_1, x_2, x_3) can be found in [17].

We expand $\nabla_{\boldsymbol{m}} G$ and $\nabla_{\boldsymbol{m}} G^{\text{me}}$ in terms of (m_1, m_2), considering that $\frac{\partial G}{\partial m_1}|_{\boldsymbol{m}=\boldsymbol{m}_0} = \frac{\partial G}{\partial m_2}|_{\boldsymbol{m}=\boldsymbol{m}_0} = 0$ by definition of $\boldsymbol{m}_0$. This leads to

$$\mu_0 \boldsymbol{H}_{\text{eff}} = -\begin{pmatrix} G_{11} m_1 + G_{12} m_2 \\ G_{12} m_1 + G_{22} m_2 \\ G_3 \end{pmatrix} - \begin{pmatrix} G_1^{\text{me}} \\ G_2^{\text{me}} \\ G_3^{\text{me}} \end{pmatrix}, \tag{2.6}$$

where we use the abbreviations $G_i = \partial_{m_i} G|_{\boldsymbol{m}=\boldsymbol{m}_0}$ and $G_{ij} = \partial_{m_i} \partial_{m_j} G|_{\boldsymbol{m}=\boldsymbol{m}_0}$.

Similar to Eq. (1.11), we make a plane-wave ansatz for the transverse magnetization components, $m_i = m_i^0 \exp[i(kx - \omega t)]$, $i \in \{1, 2\}$, with angular frequency ω and wave

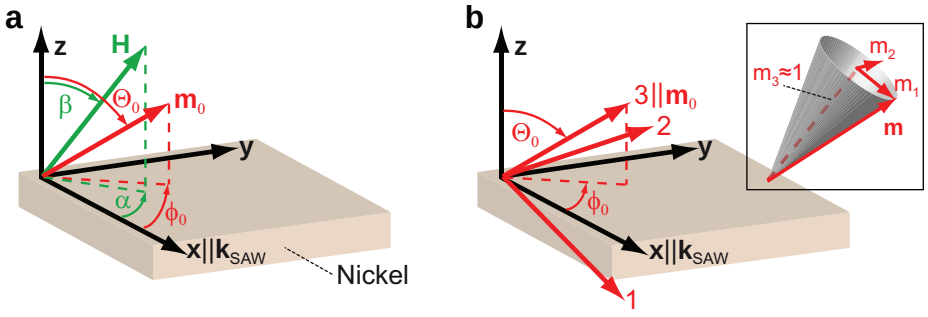

Figure 2.1: (**a**) Definition of the angles α, β, θ_0 and ϕ_0: α and β parametrize the orientation of the external magnetic field $\mu_0\boldsymbol{H}$, and θ_0 and ϕ_0 denote the equilibrium direction of the magnetization, $\boldsymbol{m}_0$. (x, y, z) is the sample coordinate system where $\boldsymbol{x}$, $\boldsymbol{y}$ and $\boldsymbol{z}$ are along the SAW propagation direction, in the film plane and normal to the film plane, respectively. Based on $\boldsymbol{m}_0$, we define a second frame of reference, (x_1, x_2, x_3), as indicated in (**b**). Here, $\boldsymbol{x_3}$ is along m_0, $\boldsymbol{x_2}$ lies in the film plane and $\boldsymbol{x_1}$ is perpendicular to $\boldsymbol{x_2}$ and $\boldsymbol{x_3}$ so that (x_1, x_2, x_3) is right-handed. Panel (**b**) has been taken from [17].

number k. With this ansatz and the linearized $\mu_0\boldsymbol{H}_{\text{eff}}$ from Eq. (2.6), the Landau-Lifshitz-Gilbert equation (2.1) can be written in matrix form. As $m_3 \approx 1$, we hereby only regard the transverse magnetization components:

$$\begin{pmatrix} G_{11} - G_3 - \frac{i\omega\alpha}{\gamma} & G_{12} + \frac{i\omega}{\gamma} \\ G_{12} - \frac{i\omega}{\gamma} & G_{22} - G_3 - \frac{i\omega\alpha}{\gamma} \end{pmatrix} \begin{pmatrix} m_1 \\ m_2 \end{pmatrix} = \mu_0 \begin{pmatrix} h_1 \\ h_2 \end{pmatrix}, \tag{2.7}$$

where $\mu_0 h_i = -G_i^{\text{d}} = -\partial_{m_i} G^{\text{d}}|_{\boldsymbol{m}=\boldsymbol{m}_0}$ are the components of the effective driving field[3]

[3]Please note that by definition the effective driving field vector $\boldsymbol{h} = (h_1, h_2)^{\text{T}}$ has only two components, in contrast to $\boldsymbol{m}$ or $\boldsymbol{H}$.

$\boldsymbol{h}$:

$$\begin{aligned}\mu_0 h_1 &= 2b_1 \sin\theta_0 \cos\theta_0 [\varepsilon_{xx} \cos^2\phi_0 + \varepsilon_{yy} \sin^2\phi_0 - \varepsilon_{zz}] \\ &\quad -2b_1 [(\varepsilon_{xz} \cos\phi_0 + \varepsilon_{yz} \sin\phi_0) \cos(2\theta_0) + 2\varepsilon_{xy} \sin\theta_0 \cos\theta_0 \sin\phi_0 \cos\phi_0] \quad (2.8) \\ \mu_0 h_2 &= 2b_1 \sin\theta_0 \sin\phi_0 \cos\phi_0 [\varepsilon_{xx} - \varepsilon_{yy}] \\ &\quad -2b_1 [\cos\theta_0 (\varepsilon_{yz} \cos\phi_0 - \varepsilon_{xz} \sin\phi_0) + \varepsilon_{xy} \sin\theta_0 \cos(2\phi_0)]. \quad (2.9)\end{aligned}$$

While in conventional FMR the driving field $\boldsymbol{h}$ is a real electromagnetic field which is applied to the FM, in ADFMR, $\boldsymbol{h}$ is purely virtual and is introduced to describe the magnetoelastic interaction between the radio-frequency elastic strain and the magnetization in the FM.

Solving Eq. (2.7) for $(m_1, m_2)^T$ gives

$$\begin{pmatrix} m_1 \\ m_2 \end{pmatrix} = \chi \begin{pmatrix} h_1 \\ h_2 \end{pmatrix} \quad (2.10)$$

with the Polder susceptibility tensor [45]

$$\chi = \begin{pmatrix} G_{11} - G_3 - \frac{i\omega\alpha}{\gamma} & G_{12} + \frac{i\omega}{\gamma} \\ G_{12} - \frac{i\omega}{\gamma} & G_{22} - G_3 - \frac{i\omega\alpha}{\gamma} \end{pmatrix}^{-1}. \quad (2.11)$$

As we can see from Eq. (2.10), the magnetization precession amplitude is the product of the virtual driving field $\boldsymbol{h}$ induced by the elastic strains in the FM and the Polder susceptibility tensor, which depends on the material parameters γ, α, B_d, B_u and the static external magnetic field $\boldsymbol{H}$. This tensor reflects the static properties of the ferromagnetic thin film as is does not depend on any time-dependent quantity. The virtual driving $\boldsymbol{h}$ field describes the dynamics of ADFMR and shows – unlike conventional FMR – a pronounced $\boldsymbol{m}_0$-dependence, which changes with the applied strain components. To illustrate this, Fig. 2.2 shows polar plots of $|\mu_0 \boldsymbol{h}|$ for different applied strains ε_{ij} and different orientations (θ_0, ϕ_0) of the equilibrium magnetization $\boldsymbol{m}_0$ with respect to the SAW propagation direction.

Regarding the first row in Fig. 2.2 (denoted as IP' configuration), we see that for a pure longitudinal strain ε_{xx}, $|\boldsymbol{h}|$ is maximum at $\phi_0 = \pm 45°$, but vanishes at 0° and $\pm 90°$, resulting in a characteristic four-fold butterfly shape. For a Rayleigh wave, ε_{xx} dominates (see Tab. 1.2), so we expect an ADFMR angle-dependence similar to

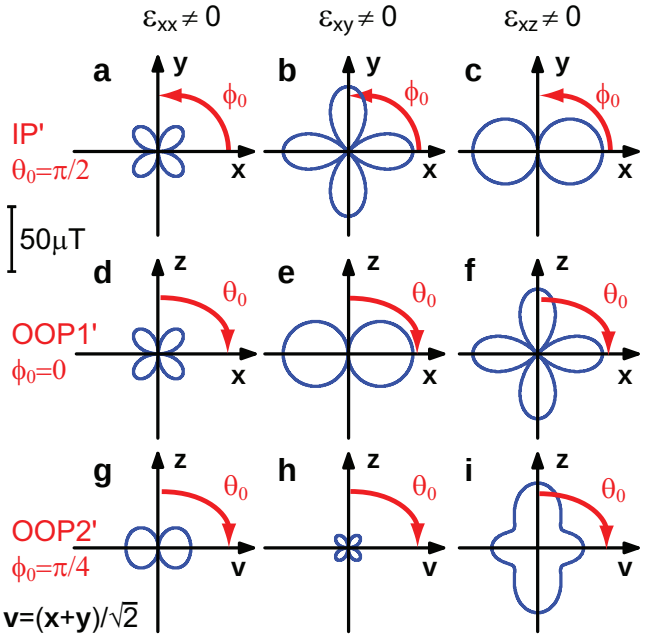

Figure 2.2: Polar plot of $|\mu_0 \boldsymbol{h}|$ for different orientations and strain components (from [17]). In Panel (**a**) to (**c**), $\boldsymbol{m}_0$ lies in the film plane ($\theta_0 = \pi/2$) at an angle of ϕ_0 to the SAW propagation direction. Panel (**d**) to (**f**) show $|\mu_0 \boldsymbol{h}|$ for a θ_0-rotation in the plane $\phi_0 = 0$, which is perpendicular to the film plane. In Panel (**g**) to (**i**), finally, $\boldsymbol{m}$ and the SAW propagation direction $\boldsymbol{x}$ enclose an angle of $\pi/4$. For vanishing anisotropy ($B_\mathrm{u} = B_\mathrm{d} = 0$), and thus $\boldsymbol{H} \parallel \boldsymbol{m}_0$, these rotation planes correspond to the IP, OOP 1 and OOP 2 configuration which will be introduced in Sect. 3.2, so they have been labeled IP', OOP', and OOP 2'. The plotted $|\mu_0 \boldsymbol{h}|$ has been calculated using Eqs. (2.8) and (2.9), setting all strain components to zero except from the one indicated ((**a**), (**d**) and (**g**): $\varepsilon_{xx} \neq 0$, (**b**), (**e**) and (**h**): $\varepsilon_{xy} \neq 0$, (**c**), (**f**) and (**i**): $\varepsilon_{xz} \neq 0$). The plotted scale bar holds for $b_1 = 25\,\mathrm{T}$ and the non-vanishing strain component $\varepsilon_{ij} = 10^{-6}$.

Fig. 2.2a. For a pure ε_{xy} strain (see Fig. 2.2b), the characteristic angle-dependence is rotated by 45°, so that $|\boldsymbol{h}|$ reaches its maximum at $\phi_0 = 0°$ and $\pm 90°$ and is zero at $\pm 45°$. As ε_{xy} is the dominant strain component for a SH wave on 36°YX-$LiTaO_3$ (see Tab. 1.3), the corresponding ADFMR signature should reflect an angle-dependence similar to Fig. 2.2b.

In Chap. 3, we will present the experimental results for Rayleigh and SH wave driven FMR, and we will show that the observed angle-dependence matches the theoretical considerations.

In conventional FMR experiments, in contrast, $|\boldsymbol{h}|$ does not depend on the orientation of the static magnetic field. Therefore, a polar plot of $|\boldsymbol{h}|$ similar to Fig. 2.2 would simply yield a circle.

2.1.3 Absorbed radio-frequency power

It is difficult to directly measure magnetization precession via microwave-based equipment. Therefore, we calculate the microwave power which is absorbed by ADFMR, as this can easily be detected by means of network analysis.

According to [47], the absorbed power P_{abs} in conventional FMR can be written as

$$P_{\mathrm{abs}} = -\frac{\omega\mu_0}{2} \int_{V_0} \mathrm{Im}\left[\left(h^*_{1,\mathrm{ext}}, h^*_{2,\mathrm{ext}}\right) \chi \begin{pmatrix} h_{1,\mathrm{ext}} \\ h_{2,\mathrm{ext}} \end{pmatrix} \right] \mathrm{d}V, \tag{2.12}$$

where V_0 is the volume of the ferromagnetic film and $\boldsymbol{h}_{\mathrm{ext}}$ denotes the external AC magnetic driving field. We adapt this formula to ADFMR by identifying $\boldsymbol{h}_{\mathrm{ext}}$ with the virtual driving field $\boldsymbol{h}$, which is due to magnetoelastic coupling. In Fig. 2.3, P_{abs} is plotted against magnitude and orientation of the external static magnetic field $\mu_0\boldsymbol{H}$, together with the virtual driving field $\mu_0\boldsymbol{h}$ and the susceptibility χ. While in conventional FMR, $\mu_0\boldsymbol{h}$ is independent of the static magnetic field orientation α and therefore the angle-dependence of P_{abs} resembles the one of the susceptibility χ, in ADFMR $\mu_0\boldsymbol{h}$ depends on the magnetization direction $\boldsymbol{m}$ as well as on the applied strains (cf. Sect. 2.1.2), so that the characteristic angle-dependence of P_{abs} in ADFMR looks qualitatively different from conventional FMR.

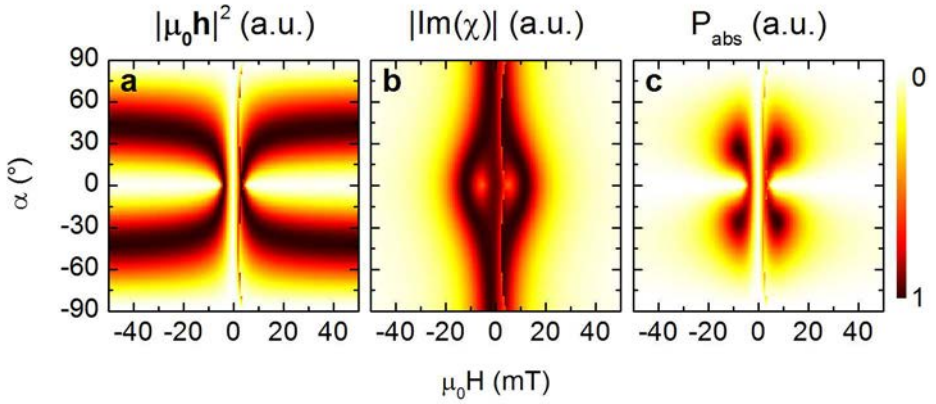

Figure 2.3: $\boldsymbol{H}$-dependence of (**a**) virtual driving field $\mu_0\boldsymbol{h}$, (**b**) susceptibility χ and (**c**) absorbed power P_{abs}, as calculated with Eqs. (2.8), (2.11) and (2.12). $\boldsymbol{H}$ lies in the film plane $\theta = 0°$, at an angle of ϕ to the SAW propagation direction $\boldsymbol{x}$. The frequency was set to $\nu = 2.24\,\mathrm{GHz}$, the anisotropy parameters are $B_{\mathrm{d}} = 400\,\mathrm{mT}$, $B_{\mathrm{u}} = 2.5\,\mathrm{mT}$ and $\boldsymbol{u} = \boldsymbol{x}$. The saturation magnetization M_{s} and the gyromagnetic ratio γ have been taken from Tab. 2.1. The strain was assumed to be purely longitudinal, i. e. only $\varepsilon_{xx} \neq 0$, and the damping parameter was taken as $a = 0.1$.

2.1.4 Effects of shear strains on ADFMR symmetry

Assuming a strain tensor ε_{ij} with $\varepsilon_{xz} = \varepsilon_{yz} = 0$, the ADFMR signature is symmetric with respect to the external field $\mu_0\boldsymbol{H}$. This means that a rotation $\mu_0\boldsymbol{H}$ by π does not change the magnetization precession amplitudes and the absorbed power. Adding one of the off-diagonal strain components ε_{xz} or ε_{yz}, however, breaks this symmetry. This is illustrated in Fig. 2.4, where the power absorption calculated with the LLG model is shown for different strains ε_{ij}.

To study the effect of ε_{xz} or ε_{yz} strains on the ADFMR symmetry theoretically, we first regard Eq. (2.2). Assuming that, for a given set of parameters B_{u}, B_{d} and $\boldsymbol{u}$, the free-enthalpy density G is minimized by some $\boldsymbol{m}_0$ at a certain field $\boldsymbol{H}_0$, then $-\boldsymbol{m}_0$ minimizes G at $\boldsymbol{H} = -\boldsymbol{H}_0$, as $G(\boldsymbol{H}, \boldsymbol{m}_0) = G(-\boldsymbol{H}, -\boldsymbol{m}_0)$. Thus, an inversion of the external field direction also reverses the equilibrium magnetization direction $\boldsymbol{m}_0$.

We now introduce a transformation $\mathcal{T}$, which describes the inversion of the equilibrium magnetization orientation $\boldsymbol{m}_0$:

$$\mathcal{T}: \quad \boldsymbol{m}_0 \to -\boldsymbol{m}_0. \tag{2.13}$$

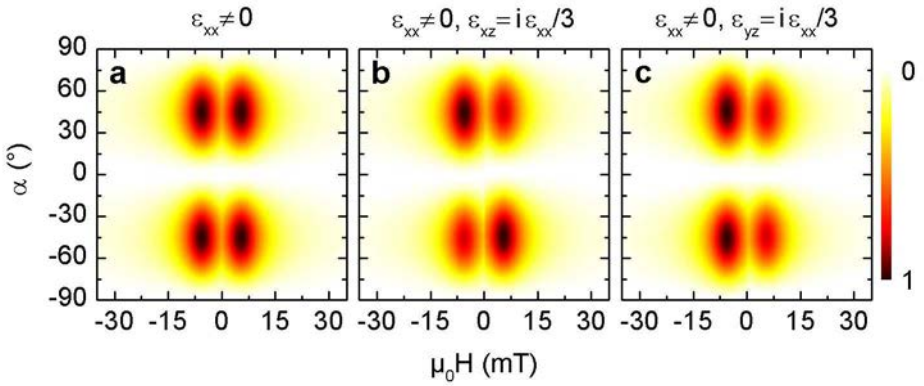

Figure 2.4: Angle-dependence of P_{abs} for different strains ε_{ij}. The simulation parameters and the angle definition is the same as in Fig. 2.3, the strains have been chosen as following: (**a**) only $\varepsilon_{xx} \neq 0$, (**b**) $\varepsilon_{xx} \neq 0$ and $\varepsilon_{xz} = i\varepsilon_{xx}/3$ and (**c**) $\varepsilon_{xx} \neq 0$ and $\varepsilon_{yz} = i\varepsilon_{xx}/3$. P_{abs} is plotted in arbitrary units and normalized to its maximum.

Regarding the angles θ_0 and ϕ_0, an inversion of $\boldsymbol{m}_0$ does not affect θ_0, but shifts ϕ_0 by π. Thus,

$$\begin{aligned} \mathcal{T}: \quad & \theta_0 \to \theta_0 \\ & \phi_0 \to \phi_0 + \pi. \end{aligned} \tag{2.14}$$

In anticipation of the next paragraph, we give the corresponding transformations of sine and cosine of θ_0 and ϕ_0:

$$\begin{aligned} \mathcal{T}: \quad & \sin(\theta_0) \to \sin(\theta_0) \\ & \cos(\theta_0) \to \cos(\theta_0) \\ & \sin(\phi_0) \to -\sin(\phi_0) \\ & \cos(\phi_0) \to -\cos(\phi_0). \end{aligned} \tag{2.15}$$

Regarding Eq. (2.8) and (2.9), we see that for a purely diagonal strain tensor ε_{ij}, i. e. $\varepsilon_{yz} = \varepsilon_{xz} = \varepsilon_{xy} = 0$, the virtual driving field $\boldsymbol{h}$ is given by $\mu_0 h_1 \propto \sin\theta_0 \cos\theta_0[\varepsilon_{xx}\cos^2\phi_0 + \varepsilon_{yy}\sin^2\phi_0 - \varepsilon_{zz}]$ and $\mu_0 h_2 \propto \sin\theta_0 \sin\phi_0 \cos\phi_0[\varepsilon_{xx} - \varepsilon_{yy}]$. Obviously, h_1 and h_2 are invariant under the transformation $\mathcal{T}$, as all factors containing ϕ_0 are of the form $\sin^2(\phi_0)$, $\cos^2(\phi_0)$ or $\sin(\phi_0)\cos(\phi_0)$, which do not change sign under $\mathcal{T}$. As the susceptibility tensor χ is invariant under $\mathcal{T}$, too, this also holds for the magnetization $(m_1, m_2)^{\mathrm{T}} = \chi\boldsymbol{h}$ and the absorbed power $P_{\mathrm{abs}} \propto \boldsymbol{h}^\dagger\chi\boldsymbol{h}$. As one can easily see from Eq. (2.8) and (2.9), the $\mathcal{T}$-invariance of $(m_1, m_2)^T$ and P_{abs} also

remains for a non-zero ε_{xy} strain component.

When introducing an additional ε_{xz} or ε_{yz} strain, however, also odd-power terms of $\sin(\phi_0)$ and $\cos(\phi_0)$ appear, which breaks the symmetry of $(m_1, m_2)^T$ and P_{abs} with respect to an inversion of $\boldsymbol{m}_0$.

2.2 Backaction of ADFMR on the SAW

In the LLG model introduced in the previous paragraph, we have calculated the magnetization precession starting from the free-enthalpy density for the FM. Moreover, we have derived a formula for the power absorption due to ADFMR which can be compared to the experiment.

In this section, the backaction of ADFMR on the acoustic wave will be examined. We thereby aim at the calculation of the complex S_{21}-parameter, which describes damping and phase shift of the acoustic wave.

As in Chap. 1, we start with the equation of motion in a solid, Eq. (1.1), to describe the elastic displacement in the ferromagnetic film:

$$\rho \frac{\partial^2 u_i}{\partial t^2} = \sum_j \frac{\partial \sigma_{ij}}{\partial x_j}, \qquad i, j \in \{1, 2, 3\}. \tag{2.16}$$

Here, $\boldsymbol{u}$ is the displacement and σ_{ij} the stress tensor in the FM. In this section, we neglect the neighboring piezoelectric crystal and its coupling to the ferromagnetic film.

In its most general form, the stress tensor σ_{ij} can be written as [25, 48]

$$\sigma_{ik} = \frac{\partial W}{\partial \varepsilon_{ik}}, \tag{2.17}$$

where W is the elastic energy density in the FM. In absence of magnetoelastic interactions, W is given by [26]

$$W^{\text{el}} = \frac{1}{2} \sum_{i,j,k,l} \varepsilon_{ij} c_{ijkl} \varepsilon_{kl}. \tag{2.18}$$

The magnetoelastic contribution to the elastic energy density has been derived in

Sect. 2.1.1 (cf. Eq. (2.3)) and is[4]

$$W^{\mathrm{me}} = G^{\mathrm{me}} M_{\mathrm{s}}. \tag{2.19}$$

As above, we make a plane-wave ansatz for the elastic displacement and the transverse magnetization components, $u_{x,y,z} = u^0_{x,y,z} \exp(ikx - i\omega t)$ and $m_{1,2} = m^0_{1,2} \exp(ikx - i\omega t)$, which is substituted into Eq. (2.16). Using $W = W^{\mathrm{el}} + W^{\mathrm{me}}$ and Eqs. (2.18) and (2.19), we get

$$\rho\omega^2 u_x = c_{11}k^2 u_x + 2ib_1 M_{\mathrm{s}} k \sin\theta_0 \cos\phi_0 \left[\sin\phi_0 m_2 - \cos\theta_0 \cos\phi_0 m_1\right] \tag{2.20}$$

$$\rho\omega^2 u_y = c_{44}k^2 u_y - 2ib_1 M_{\mathrm{s}} k \sin\theta_0 \left[2\sin\phi_0 \cos\phi_0 \cos\theta_0 m_1 + \cos(2\phi_0) m_2\right] \tag{2.21}$$

$$\rho\omega^2 u_z = c_{44}k^2 u_z + 2ib_1 M_{\mathrm{s}} k \left[\sin\phi_0 \cos\theta_0 m_2 - \cos(2\theta_0) \cos\phi_0 m_1\right]. \tag{2.22}$$

As we have assumed an elastically isotropic ferromagnetic film, the stiffness tensor has only two independent components, c_{11} and c_{44}. These are related to the commonly used Lamé constants λ and μ by $c_{11} = \lambda + 2\mu$ and $c_{44} = \mu$ [37].

The linearized LLG equation (2.10) and Eqs. (2.20) to (2.22) form a system of five linear equations for the unknown quantities u_x, u_y, u_z, m_1 and m_2. The determinant of this system of equations has to vanish to get a non-trivial solution, which allows to determine the wave number k.

To be able to proceed analytically, we neglect transverse and normal displacement component in the following (i. e., assume $u_y = u_z = 0$) and consider a purely longitudinal acoustic wave. Substituting Eqs. (2.8) to (2.11) into Eq. (2.20), we get

$$\left[\omega^2 - v_{\mathrm{l}}^2 \left(1 - \frac{F b_1^2}{v_{\mathrm{l}}^2 \mu_0 \rho} \left\{\chi_{11} w_1^2 + \chi_{22} w_2^2 - (\chi_{12} + \chi_{21}) w_1 w_2\right\}\right) k^2\right] u_x = 0 \tag{2.23}$$

with the abbreviations $w_1 = 2\sin\theta_0 \cos\theta_0 \cos^2\phi_0$, $w_2 = 2\sin\theta_0 \cos\phi_0 \sin\phi_0$ and $v_{\mathrm{l}} = \sqrt{c_{11}/\rho}$. Here, we have introduced a filling factor $F < 1$, which accounts for the fact that only a small fraction of the volume in which the SAW propagates is ferromagnetic and which therefore reduces the coupling between FMR and SAW. As the penetration depth of the SAW is of the order of the wavelength λ, F is of the order of t_{Ni}/λ, where t_{Ni} is the thickness of the ferromagnetic film.

[4] G and G^{me} from Chap. 1 have been normalized to the saturation magnetization M_{s}. As W^{me} is meant to be an energy density, i. e. energy per volume, an additional factor M_{s} appears in Eq. (2.19).

Without magnetoelastic coupling, the wave number is $k = k_0 = \frac{\omega}{v_\mathrm{l}}$. Assuming that magnetoelastic coupling involves only small changes in the elastic wave mode, we write $k = k_0 + \Delta k$, with $\Delta k \ll k_0$, and neglect higher orders of Δk in Eq. (2.23). Then, we get

$$\Delta k = F \frac{\omega b_1^2}{2 v_\mathrm{l}^3 \mu_0 \rho} \{\chi_{11} w_1^2 + \chi_{22} w_2^2 - (\chi_{12} + \chi_{21}) w_1 w_2\}. \tag{2.24}$$

Substituting Eq. (2.24) into the plane-wave ansatz $u_x = u_x^0 \exp(ikx - i\omega t)$ yields the complex transmission coefficient

$$S_{21} := \frac{u_x(x = l_\mathrm{Ni})}{u_x(x = 0)} = e^{i \Delta k l_\mathrm{Ni}}, \tag{2.25}$$

where l_Ni is the length of the ferromagnetic film. S_{21} describes damping and phase shift of the acoustic wave due to ADFMR and is normalized so that $S_{21} = 1$ off resonance.

It can be shown [17] that for small Δk and pure longitudinal strain (i. e. $\varepsilon_{xx} \neq 0$ only) the backaction model is equivalent to the Landau-Lifshitz-Gilbert approach introduced in Sect. 2.1. Phase changes of the order of $\pi/2$, as they are observed in the experiment (see Secs. 3.4 and 3.5), are beyond the limits of the backaction model and cannot be reproduced. This is due to the first-order expansion of Eq. (2.23), which is necessary to get an analytical expression for Δk. This constraint could be avoided using numerical calculations instead of an analytical approach, but as the consistency of LLG and backaction model only holds for small Δk, as shown in [17], even an exact solution of Eq. (2.23) would not extend the range of validity of the backaction model significantly.

2.3 Surface acoustic wave model

In the backaction model presented in Sect. 2.2, we have studied the effects of magnetoelastic coupling on the elastic wave in a ferromagnetic thin film and calculated the complex S_{21}-parameter. The interaction of the elastic wave in the FM with the SAW propagating on the piezoelectric crystal, however, was considered only via a phenomenological filling factor $F < 1$. Moreover, the derivation of the complex transmission in the backaction model required the assumption of low damping/dispersion,

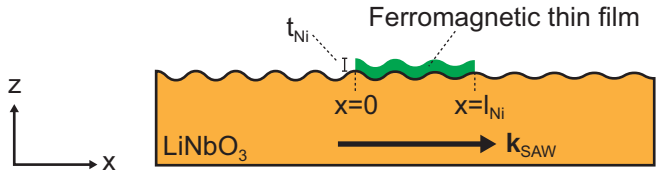

Figure 2.5: Schematic of the FM/piezoelectric crystal hybrid, as modelled in Chap. 2.3. t_{Ni} and l_{Ni} denote the thickness and the length of the ferromagnetic film, respectively.

which is not satisfied in practice.

In this section, we want to extend the backaction model to achieve a quantitative description of the elastic displacement in both piezoelectric crystal and ferromagnetic thin film including the magnetization dynamics in the FM.

2.3.1 Equations of motion and plane-wave ansatz

As illustrated in Fig. 2.5, we consider a piezoelectric crystal covered with a thin ferromagnetic metallic layer, which we assume to be isotropic concerning its elastic properties[5] and perfectly conducting. For clarity of notation, in the following $\boldsymbol{u}$ and $\boldsymbol{v}$ denote the elastic displacement in the piezoelectric crystal and the FM, respectively. All other quantities, like γ, σ_{ij} and the stiffness constants c_{ijkl} are marked with a "Ni" when referring to the ferromagnetic film; otherwise, they are related to the piezoelectric. The wave number in the piezoelectric crystal and in the ferromagnetic film is the same, and therefore the symbols β and k are equivalent in the following.

The equations of motion for the piezoelectric have been derived in Sect. 1.1 and are given by Eqs. (1.6) and (1.7). For the FM, the displacement $\boldsymbol{v}$ obeys Eq. (2.16) from Sect. 2.2. Together with Eqs. (2.17) to (2.19), we get

$$\rho_{\mathrm{Ni}} \frac{\partial^2 v_i}{\partial t^2} = \sum_{j,k,l} c^{\mathrm{Ni}}_{ijkl} \frac{\partial^2 v_k}{\partial x_j \partial x_l} + \sum_j \frac{\partial \sigma^{\mathrm{me}}_{ij}}{\partial x_j}, \qquad i \in \{1,2,3\} \tag{2.26}$$

with

$$\sigma^{\mathrm{me}}_{ij} = \frac{\partial (G^{\mathrm{me}} M_{\mathrm{s}})}{\partial \varepsilon_{ij}}. \tag{2.27}$$

As in Chap. 1, we use a plane-wave ansatz for $\boldsymbol{u}$, $\boldsymbol{v}$ and ϕ with propagation direction

[5] In the experiment, we use nickel thin films with a thickness of 50 nm, which are polycrystalline and therefore macroscopically isotropic regarding their elastic properties.

$\boldsymbol{x}$ and exponential z-dependence:

$$\boldsymbol{u}(\boldsymbol{x},t) = \boldsymbol{u}_0 \exp(i\gamma z)\exp(i\beta x - i\omega t) \tag{2.28}$$

$$\boldsymbol{v}(\boldsymbol{x},t) = \boldsymbol{v}_0 \exp(i\gamma_{\mathrm{Ni}} z)\exp(i\beta x - i\omega t) \tag{2.29}$$

$$\phi(\boldsymbol{x},t) = \phi_0 \exp(i\gamma z)\exp(i\beta x - i\omega t). \tag{2.30}$$

Due to the coupling of the wave in the piezoelectric crystal and the FM at $z = 0$, the wave number β is the same in both media, as already mentioned. The z-dependence of $\boldsymbol{u}$ and $\boldsymbol{v}$ may be different, which is reflected by two independent parameters γ and γ_{Ni}. As above, we set the additional constraint $\operatorname{Im}\gamma < 0$ to guarantee exponential decay of the acoustic wave in the piezoelectric crystal. This condition is not necessary for γ_{Ni} due to the finite thickness of the FM.

Substituting the ansatz (2.28) to (2.30) into the equations of motion (1.6), (1.7) and (2.26) yields two homogeneous systems of linear equations whose determinants are polynomials of 8^{th} degree in γ and 6^{th} degree in γ_{Ni}, respectively. Because of $\operatorname{Im}\gamma < 0$, we get four solutions for γ and six solutions for γ_{Ni} (cf. Sect. 1.3), which we denote γ^α and $\gamma^\alpha_{\mathrm{Ni}}$.

2.3.2 Interface and boundary conditions

The acoustic wave in the layered crystal system is a superposition of the fundamental solutions, given by Eqs. (2.28) to (2.30) and the γ^α and $\gamma^\alpha_{\mathrm{Ni}}$ calculated above:

$$\boldsymbol{u}_{\mathrm{tot}}(\boldsymbol{x},t) = \sum_{\alpha=1}^{4} A_\alpha \boldsymbol{u}^\alpha(\boldsymbol{x},t) \tag{2.31}$$

$$\boldsymbol{v}_{\mathrm{tot}}(\boldsymbol{x},t) = \sum_{\alpha=1}^{6} B_\alpha \boldsymbol{v}^\alpha(\boldsymbol{x},t) \tag{2.32}$$

$$\phi_{\mathrm{tot}}(\boldsymbol{x},t) = \sum_{\alpha=1}^{4} A_\alpha \phi^\alpha(\boldsymbol{x},t). \tag{2.33}$$

The superposition coefficients A_α and B_α have to be chosen such that the appropriate interface and boundary conditions are satisfied. First, the elastic displacement has to be continuous at the interface $z = 0$:

$$\boldsymbol{u}_{\mathrm{tot}} = \boldsymbol{v}_{\mathrm{tot}} \quad \text{at} \quad z = 0. \tag{2.34}$$

As we have assumed the ferromagnetic film to be perfectly conducting, the electrical potential in the piezoelectric crystal vanishes at the interface:

$$\phi_{\mathrm{tot}} = 0 \quad \text{at} \quad z = 0. \tag{2.35}$$

Next, the forces acting on an infinitesimal volume element at the interface have to sum up to zero. Therefore, the normal component of the stress tensor σ has to be continuous:

$$\sigma_{iz} = \sigma_{iz}^{\mathrm{Ni}} \quad \text{at} \quad z = 0, \quad i \in \{x, y, z\}. \tag{2.36}$$

Finally, at the surface, the normal component of the stress tensor vanishes as there are no forces normal to the surface (cf. Chap. 1):

$$\sigma_{iz}^{\mathrm{Ni}} = 0 \quad \text{at} \quad z = t_{\mathrm{Ni}}, \quad i \in \{x, y, z\}, \tag{2.37}$$

where t_{Ni} is the thickness of the ferromagnetic thin film.

In total, we have ten equations which are linear with respect to the unknown coefficients A_α and B_α. Again, this yields a determinant $\mathcal{D}'_2$ which has to be zero to get a non-vanishing SAW solution[6]. Using an iterative algorithm to find the correct wave number, β turns out to be complex now, with a small negative imaginary part which describes the damping of the SAW by ADFMR.

2.3.3 Calculation results

In this section, some exemplary calculation results are shown which were obtained with the SAW model.

First, the damping of the SAW is calculated for a Rayleigh wave propagating on YZ-$LiNbO_3$, covered with a $t_{\mathrm{Ni}} = 50\,\mathrm{nm}$ thick and $l_{\mathrm{Ni}} = 0.57\,\mathrm{mm}$ long nickel film. The material parameters for $LiNbO_3$ have been taken from Tab. 1.1, those of nickel are listed in Tab. 2.1. For simplicity, we neglect uniaxial anisotropy, i. e. set $B_{\mathrm{u}} = 0$, and assume $B_{\mathrm{d}} = \mu_0 M_{\mathrm{s}}/2 = 230\,\mathrm{mT}$ [46]. The frequency was chosen $\nu = 1.55\,\mathrm{GHz}$, and the damping parameter was taken as $a = 0.1$.

The magnetoelastic coupling constant was assumed to be 14 T and thus was inten-

[6] While an approach similar to Chap. 1, i. e. solving $\mathcal{D}'_2(\beta) = 0$ numerically, is mathematically correct, it is not the best way to determine the A_α and B_α. Instead, we present an alternative algorithm in Appendix A which yields more exact and numerically stable results and therefore has been used for the calculations shown below.

Density	ρ	8900	$\mathrm{kg/m^3}$
Lamé constants	λ_{Ni}	1.75	$\times 10^{11}\,\mathrm{N/m^2}$
	μ_{Ni}	0.74	$\times 10^{11}\,\mathrm{N/m^2}$
Saturation magnetization	M_{s}	370	$\mathrm{kA/m}$
Magnetostriction constant	λ_{s}	-3.8	$\times 10^{-5}$
Gyromagnetic ratio	γ	$2.185\mu_{\mathrm{B}}/\hbar$	

Table 2.1: Material constants for the polycrystalline nickel film, taken from [51] (density), [52] (Lamé constants), [53] (saturation magnetization), [54] (magnetostriction constant) and [55] (gyromagnetic ratio). The Lamé constants have been calculated from Young's modulus $E = 2.00 \times 10^{11}\,\mathrm{N/m^2}$ and the shear modulus $G = 0.74 \times 10^{11}\,\mathrm{N/m^2}$ given in [52], using the relations $G = \mu$ and $E = \mu(3\lambda + 2\mu)/(\lambda + \mu)$ from [37].

tionally chosen smaller than the literature value, which is given by $b_1 = -3\lambda_{\mathrm{s}}\mu_{\mathrm{Ni}} = 23\,\mathrm{T}$ [46] with the isotropic magnetostriction constant λ_{s} and the Lamé constant μ_{Ni} from Tab. 2.1. The reason is that due to pinning of the electron spin at the surface [18, 49, 50] and the ferromagnetic exchange interaction between the spins, the magnetization precession amplitude is effectively reduced. To treat this phenomenon exactly would require solving a coupled system of partial equations instead of algebraic equations, which is much more complex and numerically costly. To avoid this, the effective reduction in magnetization motion was taken into account by introducing an *effective magnetoelastic coupling constant* $\tilde{b}_1 = 14\,\mathrm{T}$. In Appendix B, an estimate of the pinning effects on the magnetization precession amplitude is given.

Figure 2.6 shows the displacement magnitude and phase, $|\boldsymbol{u}|$ and $\arg(\boldsymbol{u})$, of the SAW having crossed the nickel film, i. e. at $x = l_{\mathrm{Ni}}$. This is plotted for two different external magnetic fields: The solid lines show the simulated displacement components for $\mu_0 H = 150\,\mathrm{mT}$ (*off resonance*), while the dashed lines correspond to $\mu_0 H = 7\,\mathrm{mT}$, which is the resonance field at the chosen frequency. The plotted magnitude data are normalized to the maximum displacement at the surface and the beginning of the nickel film, $|u_z(x = 0, z = 0)|$. The angle between the external magnetic field and the SAW propagation direction was $\alpha = 45°$, as for this orientation, the driving field is maximum for a dominant ε_{xx} strain (see Fig. 2.2).

We can see that off resonance the SAW is not damped at all, as $|u_z(x = l_{\mathrm{Ni}}, z = 0)| = |u_z(0, 0)|$. In resonance, we observe a strong decrease in amplitude for all

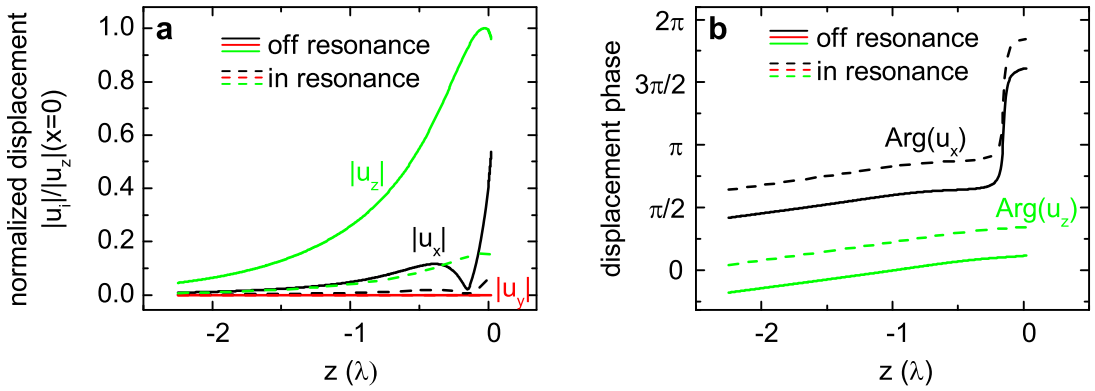

Figure 2.6: (**a**) Magnitude and (**b**) phase of the displacement $\boldsymbol{u}$ at $x = l_{\mathrm{Ni}} = 1.2\,\mathrm{mm}$ as a function of z for a Rayleigh wave on YZ-$LiNbO_3$ ($\nu = 1.55\,\mathrm{GHz}$, $\alpha = 45°$). The solid and dashed lines show the cases $\mu_0 H = 150\,\mathrm{mT}$ (*off resonance*) and $\mu_0 H = 5\,\mathrm{mT}$ (*in resonance*), respectively. As $|u_y| = 0$ within numerical errors, the phase is undefined and therefore not shown in (**b**).

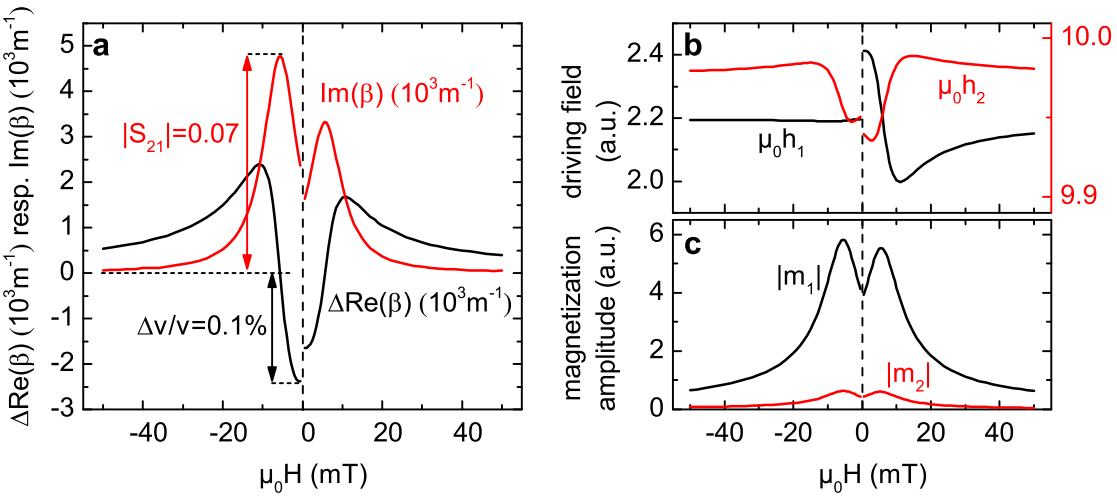

Figure 2.7: Field-dependence of (**a**) wave number β, (**b**) virtual driving field $\boldsymbol{h}$ and (**c**) magnetization precession amplitude (m_1, m_2), calculated at $x = l_{\mathrm{Ni}} = 1.2\,\mathrm{mm}$. The calculation parameters and the substrate are the same as in Fig. 2.6.

displacement components, and a phase shift of about $\pi/4$, which is uniform regarding z. The strong z-dependence of $\arg(u_x)$ around $z \approx -\lambda/6$ is due to the zero crossing of u_x at this point.

Figure 2.7a shows the field-dependent variation of the wave number β for the same configuration as above. The change of $\mathrm{Re}(\beta)$, which is proportional to the phase of the wave, indicates a variation of the propagation velocity of the wave, which is at most $\Delta v/v = -\Delta\beta/\beta \approx 0.1\%$. $\mathrm{Im}(\beta)$ corresponds to the damping of the wave via $|S_{21}| \propto \exp(-\mathrm{Im}(\beta) l_{\mathrm{Ni}})$, yielding $|S_{21}| \approx 7\%$ at $\mu_0 H_{\mathrm{res}} = -5\,\mathrm{mT}$.

In Fig. 2.7b and c, the virtual driving field $\mu_0 \boldsymbol{h}$ and the magnetization amplitude (m_1, m_2) are plotted as a function of the external field $\mu_0 H$. Obviously, the field-dependence of $\boldsymbol{h}$ is strongly asymmetric, while (m_1, m_2) is nearly symmetric and shows clear peaks at the resonance fields, with m_1 being the dominant component.

The discontinuity of β, $\boldsymbol{h}$ and $\boldsymbol{m}$ at $\mu_0 H = 0$ is due to the fact that in this model the equilibrium magnetization $\boldsymbol{m}_0$ is constant in magnitude but abruptly changes sign at $\mu_0 H = 0$. At $\mu_0 H = 0$, $\boldsymbol{m}_0$ is undefined.

The asymmetry of β, $\boldsymbol{h}$ and $\boldsymbol{m}$ with respect to the external field $\mu_0 H$ results from the shear strain ε_{xz} induced by the Rayleigh wave and has been discussed in Sect. 2.1.4.

Figure 2.8 shows the characteristic angle-dependence of the wave number β in ADFMR (on YZ-$LiNbO_3$), using the parameters given above. The driving field and therefore also the ADFMR signal is strongest at $\alpha = \pm 45°$, whereas it vanishes at 0° and ±90° (cf. Sect. 2.1.2).

To study the effects of the SAW type on the ADFMR signature, the angle-dependence of β has been calculated for a 50 nm thin nickel film on 36°YX-$LiTaO_3$ at 780 MHz and 1.04 GHz, which corresponds to the 5$^{\mathrm{th}}$ harmonic of Rayleigh and SH wave, respectively. The simulation parameters were $\tilde{b}_1 = 8\,\mathrm{T}$ and $a = 0.16$ (Rayleigh wave) resp. 0.5 (SH wave), with $B_{\mathrm{u}} = 0$ and $B_{\mathrm{d}} = 230\,\mathrm{mT}$ as above. The results are plotted in Figs. 2.9 and 2.10. For the Rayleigh wave, we notice a maximum change in β at $\alpha = \pm 45°$ and a vanishing $\Delta\beta$ at 0° and ±90°. For the SH wave, this characteristic signature is shifted by 45°, as $\Delta\beta$ is maximum at 0° and ±90°, but vanishes for $\alpha = \pm 45°$. This confirms the theoretical considerations from Sect. 2.1.2, where the characteristic ADFMR signature was predicted based on the angle-dependence of $\mu_0 \boldsymbol{h}$.

2.4 Summary

In this chapter, we have introduced three different approaches to model ADFMR. In the first method, called LLG approach, we derived an effective driving field $\mu_0 \boldsymbol{h}$ from the magnetoelastic contribution to the free-enthalpy density G^{tot}. Substituting $\mu_0 \boldsymbol{h}$ into the Landau-Lifshitz-Gilbert equation, the magnetization precession and the

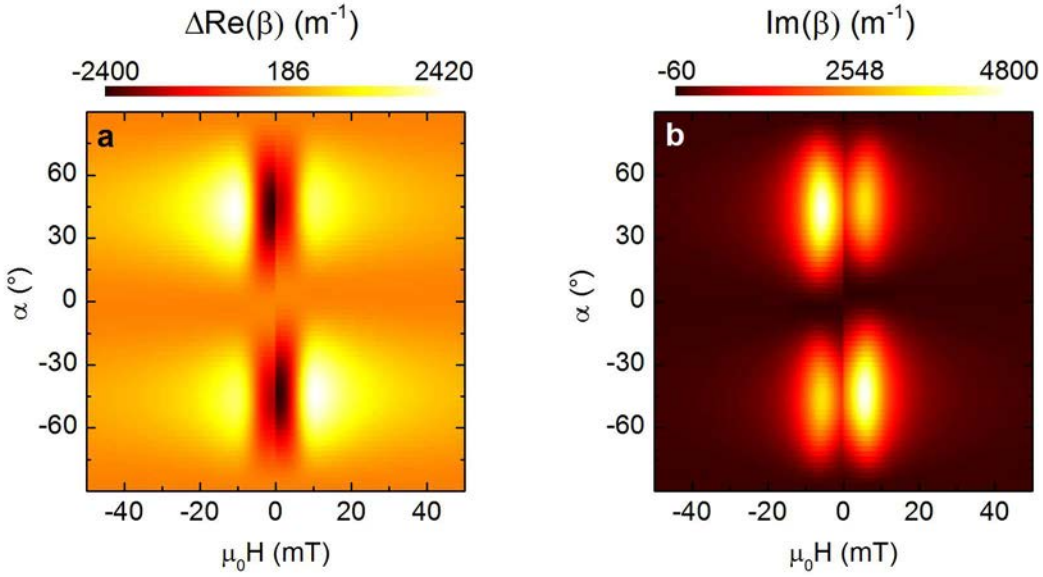

Figure 2.8: Angle-dependence of (**a**) real and (**b**) imaginary part of the wave number β, calculated with the SAW model. $\mu_0 \boldsymbol{H}$ lies in the film plane, α denotes the angle between $\mu_0 \boldsymbol{H}$ and $\boldsymbol{k}_{\mathrm{SAW}}$ (cf. Fig. 2.1a). The parameters used for the calculation are given in the text. The SAW is assumed to be a Rayleigh wave, propagating on YZ-$LiNbO_3$.

absorbed power P_{abs} can be calculated. In the backaction model, the effects of the magnetization precession on the acoustic wave in the FM are considered. To this end, a system of coupled equations has been established, describing the magnetization components m_1 and m_2 as well as the elastic displacement $\boldsymbol{u}$ induced by the acoustic wave. The self-consistent solution of this coupled system yields the magnetization precession and the corresponding change in $\boldsymbol{u}$, which can be expressed in the complex transmission parameter S_{21}.

The third model combines the backaction model with the SAW propagation theory presented in Chap. 1. Thus, not only the acoustic wave in the ferromagnetic thin film is considered, but the combined system of a SAW on the crystal, the accompanying acoustic wave in the FM *and* the induced magnetization precession is solved self-consistently. The particular type of SAW and the backaction of the magnetization precession on the SAW are inherently considered.

From a theory perspective, the SAW-FM interaction thus is described on different levels of sophistication in the three models. What remains to be addressed in future work is a quantitative treatment of the SAW excitation using interdigital transducers.

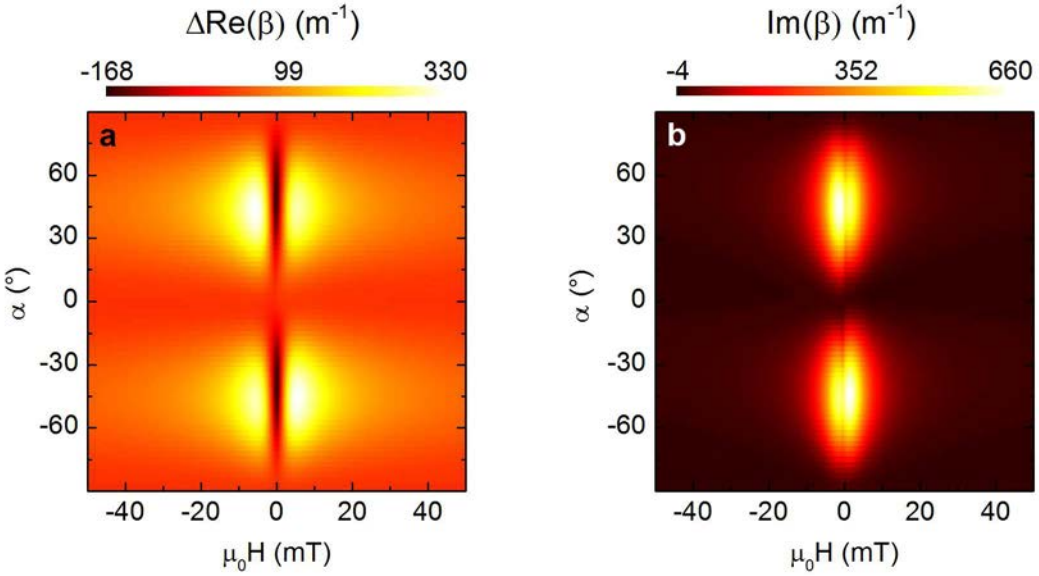

Figure 2.9: Angle-dependence of (**a**) real and (**b**) imaginary part of the wave number β, calculated with the SAW model. $\mu_0\boldsymbol{H}$ lies in the film plane, α denotes the angle between $\mu_0\boldsymbol{H}$ and $\boldsymbol{k}_{\mathrm{SAW}}$ (cf. Fig. 2.1a). The parameters used for the calculation are given in the text. The SAW is assumed to be a Rayleigh wave, propagating on 36°YX-$LiTaO_3$.

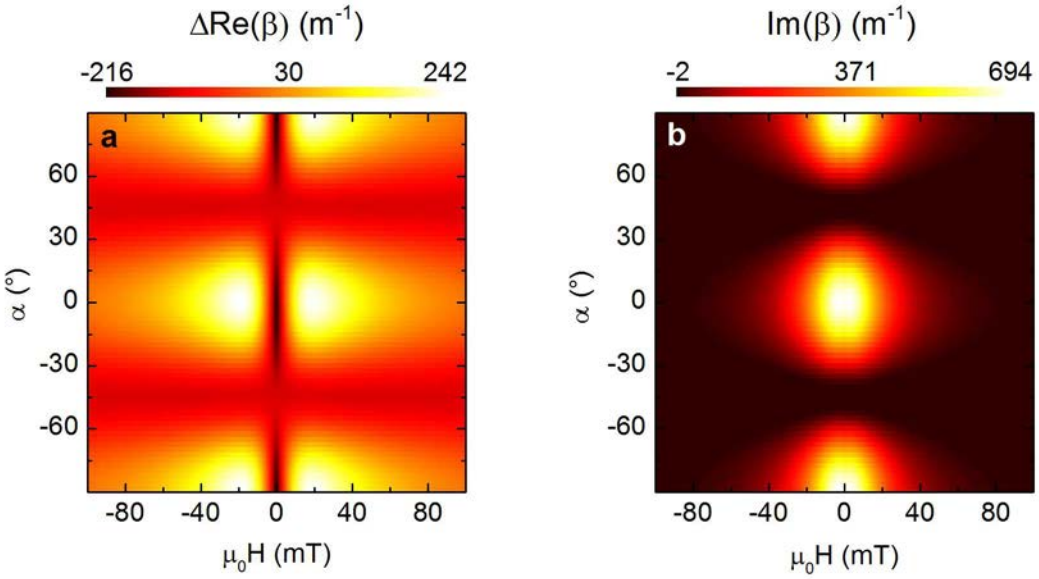

Figure 2.10: Angle-dependence of (**a**) real and (**b**) imaginary part of the wave number β, calculated with the SAW model. $\mu_0\boldsymbol{H}$ lies in the film plane, α denotes the angle between $\mu_0\boldsymbol{H}$ and $\boldsymbol{k}_{\mathrm{SAW}}$ (cf. Fig. 2.1a). The parameters used for the calculation are given in the text. The SAW is assumed to be a shear-horizontal wave, propagating on 36°YX-$LiTaO_3$.

Chapter 3

Acoustically driven FMR: Experimental study and comparison to theory

Having derived three theoretical approaches to model ADFMR in the previous chapter, we now turn to the experiment. In the following, we first introduce the samples and the experimental setup. Then a physical interpretation of the measured reflection and transmission coefficient is given and the data post-processing is explained. Finally, we present the experimental data and compare them to the calculation results obtained using the models from Chap. 2.

3.1 Samples

For the acoustically driven FMR (ADFMR) measurements, the Ni/Al-hybrid samples LNOC119, denoted as Sample 1 in the following, and LNO-36Y-14 [1] (Sample 2), were used. Sample 1 was fabricated by H. Söde [56] and is shown in [57]. Sample 2 was fabricated as a part of this thesis; a photograph of Sample 2 is given in Fig. 3.1. Both devices consist of a 1 mm thick, one-side polished piezoelectric crystal, Y-cut $LiNbO_3$ resp. 36°-rotated Y-cut $LiTaO_3$, on which a pair of aluminium interdigital transducers (IDTs) was patterned using optical lithography and e-beam evaporation. The width

[1] This sample has been chosen for the ADFMR measurements as the quality of the lithographically defined IDTs is very good, so that not only the fundamental SAW frequency but also higher harmonics can be observed (as it will be shown below).

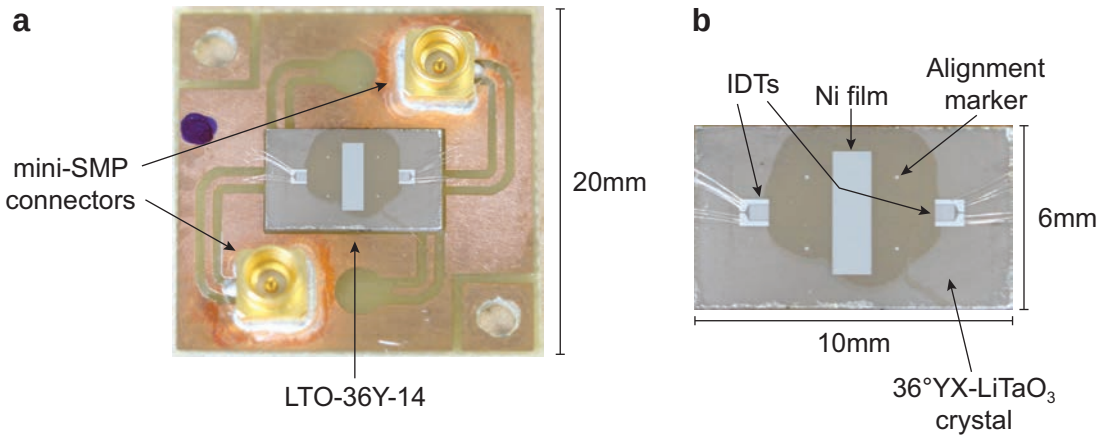

Figure 3.1: (**a**) Photograph of Sample 2, mounted on a chipcarrier which has been designed for ADFMR and acoustic spin pumping measurements. (**b**) Enlarged view of Sample 2. As the crystal is transparent, the glue used to mount the sample onto the chipcarrier appears as a clear spot.

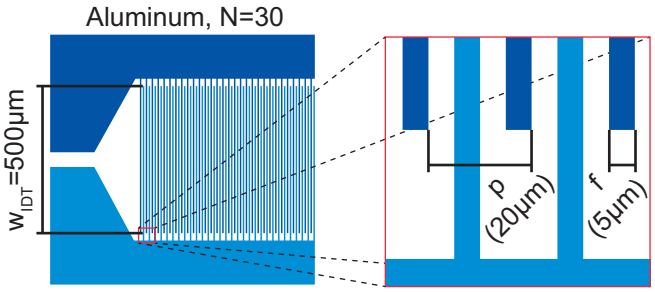

Figure 3.2: Schematic of the IDT design used in this work. f and p are the width of the IDT fingers and the periodicity of the fingers, respectively. N denotes the number of finger pairs of an IDT, and w_{IDT} is the aperture of the IDT, i. e. the length of the IDT fingers.

of the IDT fingers is 5 μm, with a metallization ratio[2] of $r = 2f/p = 50\%$, leading to a fundamental wavelength of 20 μm (see Fig. 3.2)[3]. As shown in Fig. 3.3, a $t_{\mathrm{Ni}} = 50\,\mathrm{nm}$ thin polycrystalline nickel[4] film of rectangular shape was deposited on the delayline between the IDTs using e-beam evaporation.

In Tab. 3.1, the most important geometric dimensions of both samples are listed. The fabrication parameters can be found in Appendix C and in [56, 57], respectively.

[2] As indicated in Fig. 3.2, f and p denote the width of a IDT finger and the periodicity of the fingers, respectively.
[3] For a detailed explanation of the working principle of IDTs, we refer to [43].
[4] Nickel has a high magnetostriction constant and a comparatively low coercive field, which makes it well suited for ADFMR experiments.

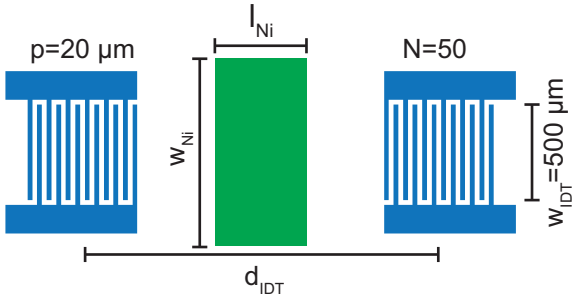

Figure 3.3: Schematic of the ADFMR samples. w_{Ni} and l_{Ni} denote width and length of the nickel thin film, and d_{IDT} is the distance between the IDT centers. f, p, N and w_{IDT} are defined in Fig. 3.2.

	t_{IDT} nm	d_{IDT} mm	t_{Ni} nm	l_{Ni} mm	w_{Ni} mm
Sample 1	70	1.4	50	0.57	0.4
Sample 2	50	5.8	50	1.2	4.0

Table 3.1: Geometric dimensions of IDTs and nickel films on Sample 1 and Sample 2.

In Tab. 3.2, the key parameters of the SAWs propagating on Sample 1 and Sample 2 are summarized from literature [40, 58].

Besides the fundamental SAW mode with a wavelength of 20 μm, IDTs also allow the excitation of higher harmonics, depending on the metallization ratio r. Assuming exactly $r = 1/2$, only each forth harmonic can be observed [59]. It will be shown

	substrate	prop. dir.	wave type	κ^2 %	v_{free} m/s	v_{met} m/s
Sample 1	Y-cut $LiNbO_3$	Z	Rayleigh	4.5	3488	3410
Sample 2	36°-rot. Y-cut $LiTaO_3$	X	SH	4.7	4212	4112
			Rayleigh	0.046	3232	3231

Table 3.2: Literature SAW properties of Sample 1 and Sample 2. κ^2 is the electromechanical coupling factor, v_{free} and v_{met} denote the sound velocity of the respective SAW, assuming a free or metallized surface. Values for κ^2, v_{free} and v_{met} have been taken from [58] ($LiNbO_3$) and [40] ($LiTaO_3$). As v_{met} for $LiNbO_3$ is not given explicitly in [58], it has been calculated from v_{free} and $\kappa^2 = -2(v_{\mathrm{met}} - v_{\mathrm{free}})/v_{\mathrm{free}}$ [58].

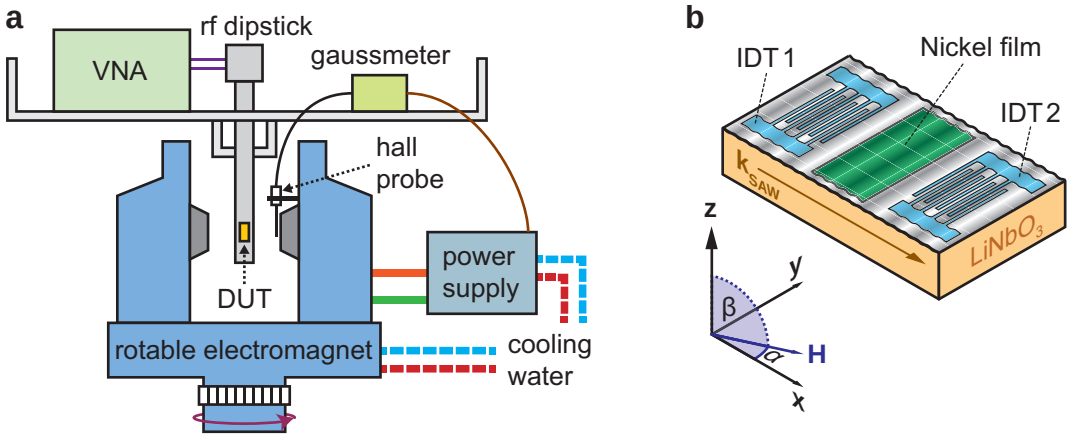

Figure 3.4: (**a**) Schematic of the ADFMR setup. (**b**) Enlarged view of the DUT. The mounting orientation of the sample in the rf dipstick can be varied using different adaptor units. Thus, the magnetic field direction relative to the SAW propagation direction can be rotated in different planes.

below (see Fig. 3.10 and 3.15) that this is fulfilled quite well in the above samples.

3.2 Experimental setup

The setup for the ADFMR measurements has been constructed by M. Weiler [16, 43]. Here, only a short overview of the experimental setup is given; a more detailed description can be found in [43].

The main components of the ADFMR setup are:

- a radio-frequency (rf) dipstick, which contains the device under test (DUT) and provides connectors for the microwave cables
- a rotable electromagnet for the generation of the static external magnetic field
- a vector network analyser (VNA), which is used to measure the transmission and reflection coefficients S_{ij} of the DUT

A schematic view of the ADFMR setup is shown in Fig. 3.4.

In order to avoid any movement of sample and microwave cables which would influence the high-frequency measurement, the rf dipstick is fixed to the rack. The DUT is mounted at the lower end of the dipstick so that is located between the pole shoes of the electromagnet. The magnet can be rotated by about 200°, which allows

to rotate the magnetic field direction with respect to the DUT. The DUT is fixed to a chipcarrier providing two rf mini-SMP connectors which are bonded to the IDTs on the DUT. Via semi-rigid coaxial cables in the rf dipstick and SMA connectors at the top end of the dipstick, the DUT is connected to the vector network analyser.

The VNA, a Rohde & Schwarz ZVB 8, covers a frequency range from 300 kHz up to 8 GHz and provides a maximum microwave output power of 30 dBm. In order to avoid thermal drift and nonlinear effects, power was chosen as low as possible, depending on the magnitude and the signal-to-noise ratio of the measured transmission signal (see below).

The external static magnetic field is generated by a Oerlikon electromagnet, which is connected to a LakeShore 642 PowerSupply. With a maximum output of 40 V and 70 A, DC fields up to 1.2 T can be generated. The power supply is feedback-controlled by a LakeShore 475 DSP Gaussmeter and a Hall sensor mounted between the pole shoes of the electromagnet.

The reflection and transmission coefficients S_{ij} measured by the VNA are defined as

$$S_{ij} = \frac{b_j}{a_i}, \tag{3.1}$$

where a_i and b_i denote the emitted and detected AC voltage at port i. Usually, $|S_{ij}|$ is expressed in logarithmic units [57]:

$$|S_{ij}|\,(\mathrm{dB}) = 20 \log |S_{ij}|. \tag{3.2}$$

As already mentioned, the electromagnet can be rotated around its vertical axis. In this way, the relative orientation between $\mu_0 \boldsymbol{H}$ and $\boldsymbol{k}_{\mathrm{SAW}}$ can be varied. The rotation plane is determined by the mounting orientation of the sample in the rf dipstick.

To simplify the interpretation of the experimental data, we define three physically interesting rotation planes, as illustrated in Fig. 3.5: In the *in-plane configuration*, the external field lies in the nickel film plane. In the *out-of-plane 1* and *out-of-plane 2 configuration*, $\mu_0 \boldsymbol{H}$ is rotated in a plane perpendicular to the nickel film, with an angle of 0° resp. 45° to $\boldsymbol{k}_{\mathrm{SAW}}$.

All measurements were performed at room temperature and standard ambient conditions.

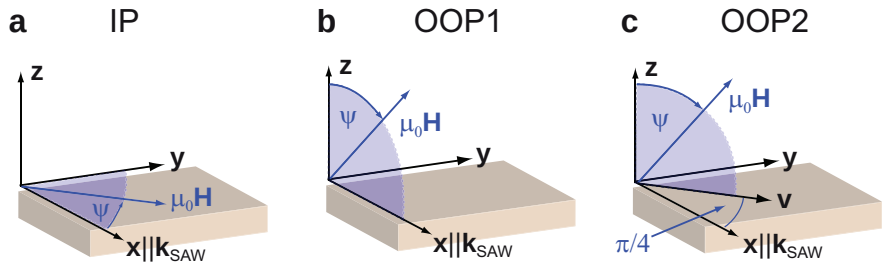

Figure 3.5: Measurement configurations employed in the ADFMR experiments (taken from [17]): (**a**) In the in-plane configuration (IP), the external magnetic field $\mu_0 \boldsymbol{H}$ is rotated in the film plane. (**b**) and (**c**) In the out-of-plane 1 (OOP 1) and out-of-plane 2 (OOP 2) configuration, the external field is rotated in a plane defined by the surface normal $\boldsymbol{z}$ and the vector $\boldsymbol{x}$ resp. $\boldsymbol{v} = (\boldsymbol{x} + \boldsymbol{y})/\sqrt{2}$.

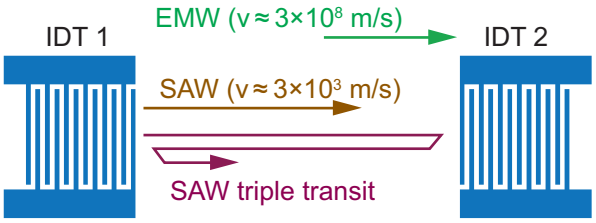

Figure 3.6: Main contributions to the measured transmission coefficient S_{21}: Crosstalk of the electromagnetic wave (EMW), SAW pulse and triple transit.

3.3 Data processing

3.3.1 SAW transmission

Earlier work by M. Weiler [16, 43] and C. Heeg [57] showed that the frequency-dependent transmission S_{21}, i. e. the ratio of the voltage detected at IDT 2 over the voltage applied to IDT 1, can be described as a superposition of different signals, as indicated in Fig. 3.6:[5]

First, the *electromagnetic crosstalk*, which arises from the fact that only a small fraction of the microwave power applied to IDT 1 is converted to a SAW, while the rest is reflected or emitted as a free-space electromagnetic wave. Due to reciprocity [59], this electromagnetic wave is detected by IDT 2 and contributes to the measured

[5] In the following, the SAW is always assumed to propagate from IDT 1 to IDT 2, i. e. IDT 1 is the emitter and IDT 2 the detector of the SAW.

transmission signal. The electromagnetic wave propagates with the speed of light $c \approx 3 \times 10^8\,\mathrm{m/s}$ and therefore arrives almost instantaneously, i. e. within about 10 ps, at IDT 2.

Second, the main SAW pulse, which is launched by IDT 1, travels with speed of sound $v_{\mathrm{SAW}} \approx 3 \times 10^3\,\mathrm{m/s}$ and thus can be observed at IDT 2 about $t = \frac{d_{\mathrm{IDT}}}{v_{\mathrm{SAW}}} \approx 0.4\,\mu\mathrm{s}$ after it has been launched.

Third, as an IDT also acts as a (bad) reflector, the SAW pulse is reflected at IDT 2, travels back to IDT 1, is reflected there again and arrives at IDT 2 at $t' \approx 3t$. This secondary SAW pulse is called *triple transit*.

Apart from these, there are several more spurious signals due to reflections of the SAW pulse at the edges of the substrate and due to the electromagnetic crosstalk caused by reflected SAW pulses passing IDT 1.

While all these signal components interfere in frequency domain and in this way distort the transmission signal of the main SAW pulse, they can be separated in time domain as they arrive at IDT 2 with different delay. To this end, the following steps are applied (cf. [57]):

1. Fourier transformation of the measured S_{21} data to time domain.

2. Application of a time gate which excludes all signal components with a delay $t < t_{\mathrm{start}}$ or $t > t_{\mathrm{stop}}$. In this way, electromagnetic crosstalk and triple transit are eliminated, as indicated in Fig. 3.7b.

3. Backtransformation of the time-gated data to frequency domain.

In Fig. 3.7a, raw and processed frequency domain data are plotted to show the effects of the time gate. While in the raw transmission data, the SAW transmission maximum around $\nu = 1.55\,\mathrm{GHz}$ is superimposed with some oscillating signal, the processed data reveal a clear maximum and the expected $|\sin(\nu)/\nu|$-dependence[6].

All $|S_{21}|$ data presented in the following are post-processed data, as just explained.

In presence of a static external magnetic field, $|S_{21}|$ changes measurably, as can be seen from Fig. 3.8a. Plotting $|S_{21}|$ against the magnetic field strength leads to

[6] The observed $|\sin(\nu)/\nu|$-dependence reflects the so-called *response function* of the IDT. It describes the frequency-dependent SAW excitation efficiency of the IDT, and can be written as the Fourier transform of the weighting function of the IDT fingers. For a finite number of equal fingers with constant overlap, the weighting function is a rectangle function, whose Fourier transform is given by $\sin(x)/x$, with $x = \nu/\nu_0$ and some constant ν_0 [59, 60].

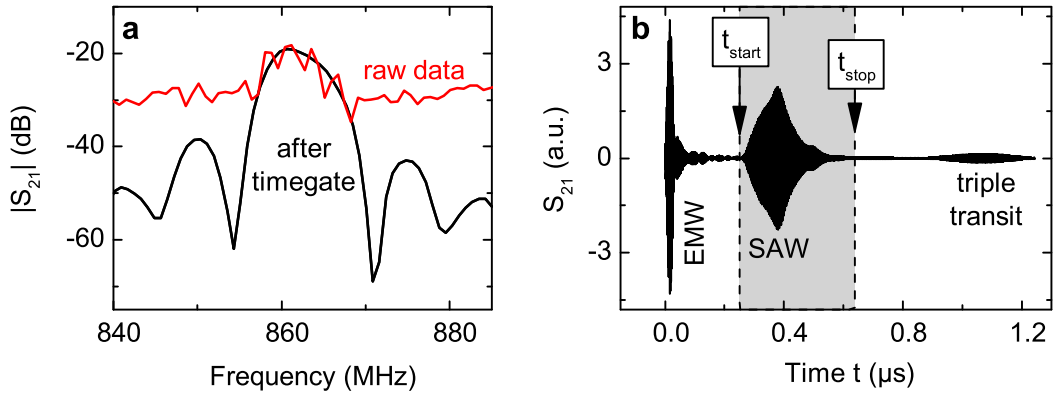

Figure 3.7: (**a**) Raw (red) and time-gated (black) transmission data $|S_{21}|$. (**b**) S_{21} as a function of time, obtained by Fourier transformation of the frequency-domain transmission data. EMW is the abbreviation for "electromagnetic wave" and denotes the electromagnetic crosstalk.

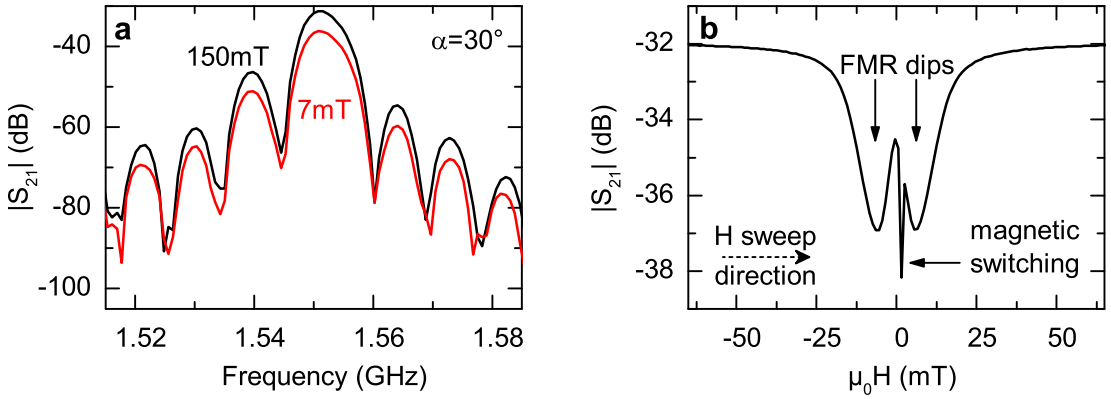

Figure 3.8: Change of the SAW transmission in a static external magnetic field. In Panel (**a**), $|S_{21}|$ is plotted against the frequency for two different external fields $\mu_0 H = 7\,\mathrm{mT}$ and $150\,\mathrm{mT}$. Panel (**b**) shows the field-dependence of $|S_{21}|$ at the center frequency of the SAW passband, $\nu = 1.551\,\mathrm{GHz}$, at $\alpha = 30°$.

characteristic transmission curves like Fig. 3.8b[7]: In resonance, i. e. for $\mu_0 H \approx \pm 7\,\mathrm{mT}$, a strong decrease in transmission of about $-5\,\mathrm{dB}$ can be observed, which corresponds to an effective damping of about $90\,\mathrm{dB/cm}$ caused by ADFMR. This means that FMR can effectively be excited by acoustic phonons in a ferromagnet.

Besides the two dips in $|S_{21}|$ around $\mu_0 H \approx \pm 7\,\mathrm{mT}$, we observe a sharp dip at $\mu_0 H \approx 2\,\mathrm{mT}$. This dip stems from magnetic switching, i. e. the switching of the magnetic moments of the nickel when changing the external magnetic field direction [43], and occurs at $\mu_0 H = \pm \mu_0 H_{\mathrm{coer}}$, where $\mu_0 H_{\mathrm{coer}} = 2\,\mathrm{mT}$ is the coercive field of nickel [43]; the sign depends on the sweep direction of $\mu_0 H$.

As the ADFMR signal due to magnetic switching corresponds to *non-resonant* interaction between acoustic wave and magnetization, it was not examined further in this thesis. Comparing experiment and calculations, one has to consider that the ADFMR models presented in Secs. 2.1, 2.2 and 2.3 do not include magnetic switching, so that experiment and calculation do not agree at $\mu_0 H_{\mathrm{coer}}$. The *resonant* coupling between SAW and ferromagnet usually occurs at higher fields than $\mu_0 H_{\mathrm{coer}}$, thus the comparison of measured and calculated resonant ADFMR signature is not disturbed by magnetic switching.

3.3.2 SAW power

While the transmission coefficient S_{21} allows to calculate the damping of the SAW, the reflection coefficient S_{11} can be used to determine the power carried by the SAW.

For frequencies outside the SAW passband, the output power P_0 of the VNA is partly reflected in IDT 1 and partly emitted in the form of electromagnetic radiation. Within the SAW passband, the reflection coefficient $|S_{11}|$ decreases remarkably due to the energy transport of the SAW, as shown in Fig. 3.9a. With $|S_{11}(\mathrm{EMW})|^2 = 0.36$ and $|S_{11}(\mathrm{EMW} + \mathrm{SAW})|^2 = 0.17$ from Fig. 3.9a, the power of the SAW is [43]

$$P_{\mathrm{SAW}} = \frac{P_0}{2}\eta, \tag{3.3}$$

where we have defined $\eta := |S_{11}(\mathrm{EMW})|^2 - |S_{11}(\mathrm{EMW} + \mathrm{SAW})|^2$. The factor $1/2$ in Eq. (3.3) accounts for the fact that there are two SAWs launched by IDT 1, propagating in opposite directions [43].

[7] In order to reduce the noise level, Fig. 3.8b does not show the field-dependence of *one single* frequency point at $\nu = 1.551\,\mathrm{GHz}$, but the averaged field-dependence of eight datapoints between $1.547\,\mathrm{GHz}$ and $1.555\,\mathrm{GHz}$. A similar averaging was applied to all data presented in the following.

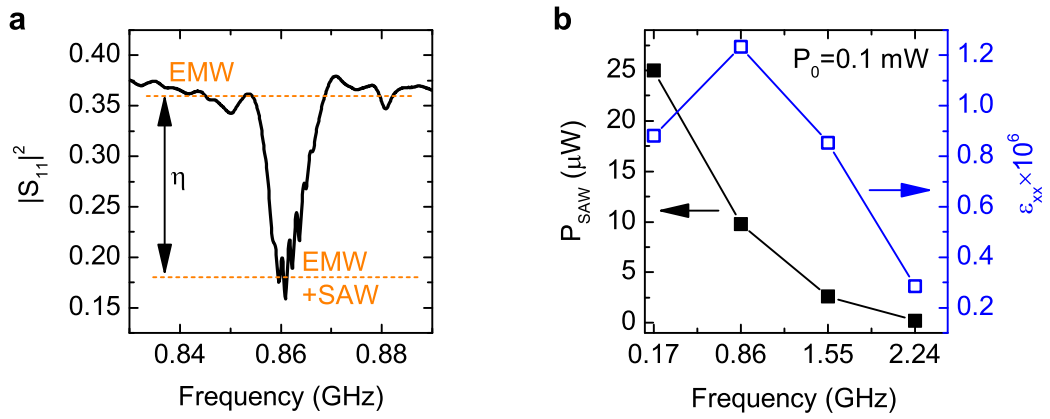

Figure 3.9: (**a**) Square of the reflection coefficient, $|S_{11}|^2$, measured around the 5$^{\text{th}}$ harmonic at 860 MHz. η is the power conversion efficiency of the IDT. (**b**) SAW power and calculated longitudinal strain ε_{xx} for the four SAW passbands at a microwave power of $P_0 = 0.1\,\text{mW}$.

Besides the elastic displacement, also the electrical field induced by the SAW contributes to P_{SAW}. Hereby, the acoustic power of the SAW is $P_{\text{acoustic}} = \kappa^2 P_{\text{SAW}}$ [59,61] with the electromechanical coupling factor κ^2 (see Sect. 1.4). Robbins [61] derived an approximative formula which relates the acoustic power of the SAW with the normal component u_z of the mechanical displacement:

$$u_z^2 = \frac{P_{\text{acoustic}}}{2M\pi\nu W}\,, \tag{3.4}$$

with $M = 1.4 \times 10^{11}\,\text{Jm}^3$ for $LiNbO_3$ [61] and the delayline width[8] $W = 500\,\mu\text{m}$. For Rayleigh waves, longitudinal and normal displacement component are related by $|u_x| \approx \frac{2}{3}|u_z|$ (cf. Fig. 1.2). Thus, for a plane wave $u_x \propto \exp(ikx)$, the pure strain $\varepsilon_{xx} = \frac{\partial u_x}{\partial x}$ is

$$|\varepsilon_{xx}| = k|u_x| = \frac{2}{3}\,k\,\frac{P_{\text{acoustic}}}{2M\pi\nu W}\,. \tag{3.5}$$

In Fig. 3.3b, the magnitude of ε_{xx} is plotted for the four SAW passbands. The strains induced by the SAW are in the order of 10^{-6} corresponding to displacements in the picometer range. The maximum strain is reached at the 5$^{\text{th}}$ harmonic.

Because of several approximations in the derivation of Eq. (3.5) and the disregard of

[8]Here, we assume the delayline width to be identical with the IDT aperture w_{IDT}, neglecting the divergence of the wave. This is a good approximation, as for the given crystal cuts, the SAW automatically tends to propagate along the destined direction due to the beam steering effect [59].

the z-dependence of $\boldsymbol{u}$, Eq. (3.5) is not suitable for an exact calculation of the strains induced by the SAW. Instead, the strains ε_{ij} appearing in the LLG and backaction model were treated as free parameters and fitted to the experimental results. It will be shown below (cf. Tab. 3.3) that the deviation of the present estimate from the fitted strains is less than 30%. This is quite remarkable, considering the fact that Eq. (3.5) is an a priori estimate which uses only the variation in $|S_{11}|$ and the output power of the VNA to predict the SAW displacement.

3.3.3 Normalized transmission coefficient and absorbed power

As one can see from Fig. 3.8, $|S_{21}| \ll 1$ even off resonance, e. g. for $\mu_0 H = 150\,\mathrm{mT}$. The reason is that the microwave provided by the VNA has to be converted into a SAW in IDT 1, propagate from IDT 1 to IDT 2, and be converted back to a AC voltage in IDT 2. While the propagation loss of the SAW can be neglected[9], the conversion of a radio-frequency voltage into a SAW and vice versa in the IDTs is comparatively inefficient, leading to a field-independent contribution to the damping of the microwave. As we are only interested in the ADFMR-related SAW damping, which is field-dependent and vanishes for very low/high fields, the measured S_{21} is normalized by

$$S_{21}^{\mathrm{norm}}(\mu_0 H) := \frac{S_{21}(\mu_0 H)}{S_{21}(\mu_0 H_{\mathrm{off}})}\,, \tag{3.6}$$

where $\mu_0 H_{\mathrm{off}}$ is large compared to the occurring resonance fields.

This normalization has been applied to all experimental data shown in the following. Nevertheless, we keep the symbol S_{21} instead of S_{21}^{norm} for a clearer notation.

The power absorbed in ADFMR can be derived from the power carried by the SAW (see Eq. (3.3)) and the normalized transmission coefficient S_{21} (see Eq. (3.6)) and is given by

$$P_{\mathrm{abs}} = \left(1 - |S_{21}|^2\right) P_{\mathrm{SAW}}. \tag{3.7}$$

[9] For Rayleigh waves on YZ-$LiNbO_3$, e. g., the attenuation coefficient is about $1\,\mathrm{dB}/\mu\mathrm{s}$ at $\nu = 1\,\mathrm{GHz}$ [25].

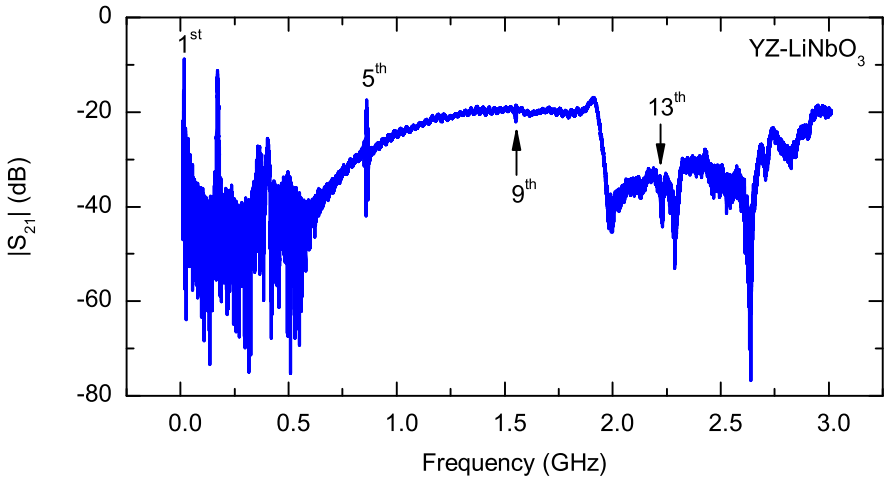

Figure 3.10: Transmission spectrum of Sample 1. Besides the SAW frequencies 172 MHz, 860 MHz, 1.55 GHz and 2.24 GHz (the latter are more clear in a zoom-in spectrum), we observe other peaks which are due to resonances in the measurement setup (radio-frequency dipstick, microwave cables, chipcarrier etc.).

3.4 Rayleigh wave driven ADFMR

3.4.1 SAW transmission of Sample 1

In Fig. 3.10, the transmission spectrum of Sample 1 is shown. As expected we do not see only the fundamental SAW frequency at 172 MHz, but also the 5^{th}, 9^{th} and 13^{th} harmonics. This allows us to study acoustically driven FMR at different frequencies.

The measurements presented in the following are confined to a small range of 100 MHz around the SAW passband center frequencies 860 MHz, 1.55 GHz and 2.24 GHz. The fundamental frequency 172 MHz is too low to satisfy the resonance condition for FMR (cf. [18]), so we do not consider this SAW passband further.

The measured transmission data – evaluated as described in Sect. 3.3 – show a distinct magnetic field-dependence, which varies with the angle between external magnetic field $\mu_0 \boldsymbol{H}$ and the SAW propagation direction $\boldsymbol{x}$. Therefore, in the following sections, magnitude and phase of S_{21} are plotted against magnetic field strength and orientation in order to show the full characteristic signature of ADFMR.

3.4.2 Comparison of the experimental data with the ADFMR models

Before the experimental results are shown for all investigated frequencies and all magnetic field orientations, we first present a comparison of one exemplary ADFMR trace with the modelling approaches presented in Chap. 2. To this end, in Fig. 3.11, $|S_{21}|$ as a function of magnetic field strength and orientation is plotted for $\nu = 1.55\,\mathrm{GHz}$ and IP configuration, together with the simulation results obtained with the LLG, backaction and SAW model, respectively. ψ denotes the angle between $\mu_0\boldsymbol{H}$ and the SAW propagation direction $\boldsymbol{x}$, as indicated in Fig. 3.5. For a better understanding of the color code in Fig. 3.11, we refer to Fig. 3.8b, which shows a single ADFMR trace (at $\alpha = 30°$) out of Fig. 3.11b.

The simulations require a set of parameters $\{B_\mathrm{d}, B_\mathrm{u}, a\}$, which has to be determined from the comparison of experimental and calculated data. We found that $B_\mathrm{d} = 400\,\mathrm{mT}$ and $B_\mathrm{u} = 2.5\,\mathrm{mT}$ along $\boldsymbol{u} = \boldsymbol{x}$ allow to consistently describe the experimental results (see Figs. 3.12 to 3.14). The damping parameter was found to be $a = 0.1$, which is a factor of two larger than typical literature values for polycrystalline nickel films [62]. The reason for the larger a-value could be the excitation of higher spin wave modes[10] which cannot be resolved, or non-Gilbert-type damping contributions. Besides, surface pinning of the electron spins affects the magnetization excitation and has been reported to broaden the FMR line [49,63]. This effect increases with the wave number k and therefore could make a relevant contribution in ADFMR, where we are dealing with comparatively short wavelengths and high wave numbers. Therefore, further studies of ADFMR at higher frequencies are required.

The material parameters for the nickel film have been taken from Tab. 2.1. The magnetoelastic coupling constant b_1, used in the backaction model, has been calculated via $b_1 = -3\lambda_\mathrm{s}\mu_\mathrm{Ni} = 23\,\mathrm{T}$ [46] with the isotropic magnetostriction constant λ_s and the Lamé constant μ_Ni from Tab. 2.1. The thickness of the nickel film in Sample 1 is $t_\mathrm{Ni} = 50\,\mathrm{nm}$ (see Tab. 3.1). The strains fitted with the LLG and backaction model and the filling factor used in the backaction model are given in Tab. 3.3.

The material constants for $LiNbO_3$, which have been used in the SAW model, are given in Tab. 1.1. The effective magnetoelastic coupling constant for the SAW model was chosen $\tilde{b}_1 = 14\,\mathrm{T}$.

[10] In the presented models, we assumed a uniform magnetization with all electron spins precessing in phase. This corresponds to the fundamental (collective) spin wave mode.

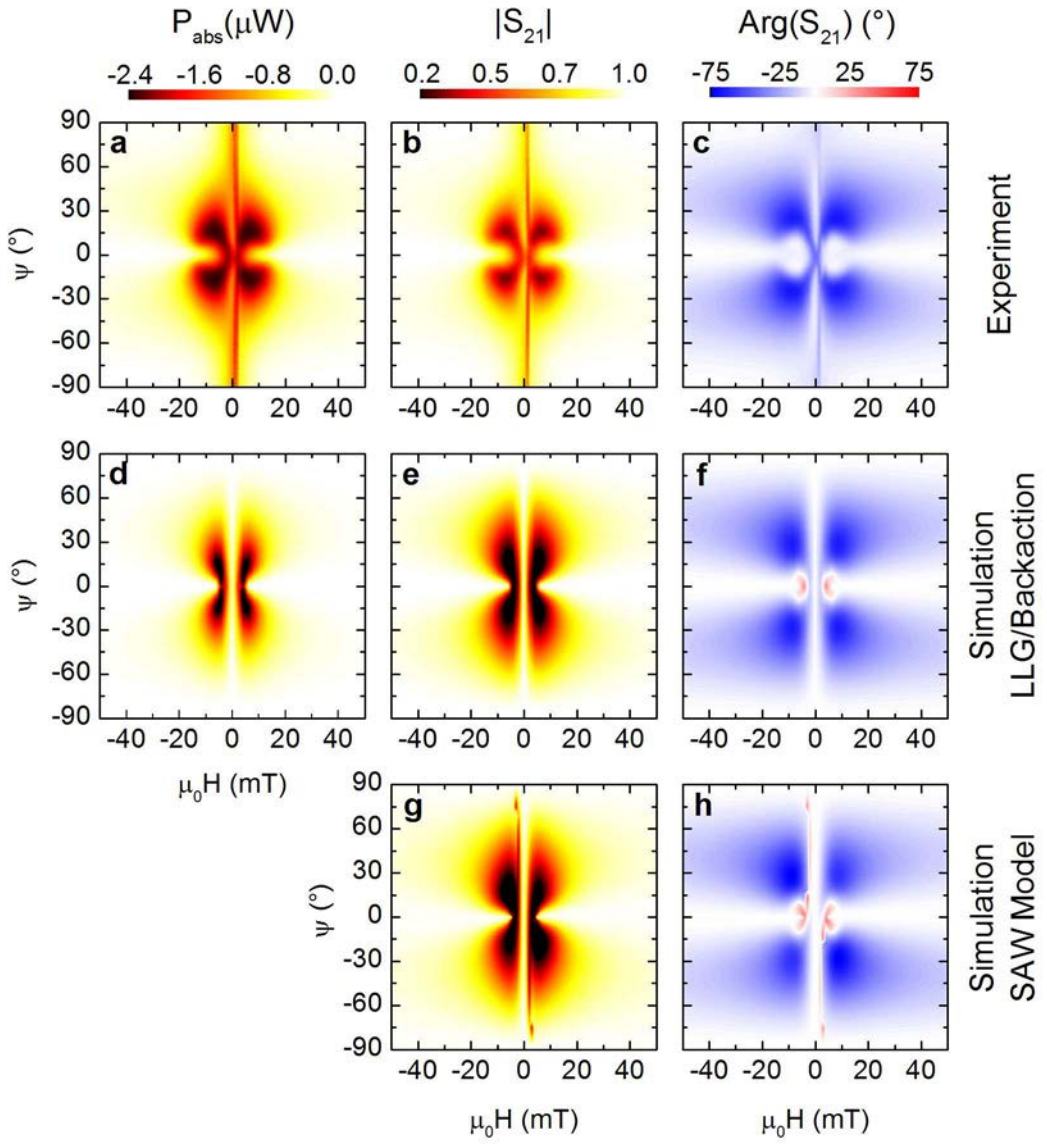

Figure 3.11: Comparison between measured and simulated angle-dependence of ADFMR in Sample 1, using the models presented in Chap. 2. Panel (**a**) to (**c**) show P_{abs}, $|S_{21}|$ and $\arg(S_{21})$ plotted versus magnetic field orientation and strength for IP configuration and $\nu = 1.55\,\mathrm{GHz}$. In Panel (**d**), the power absorption calculated with the LLG approach (see Eq. (2.12)) is shown. In Panel (**e**) and (**f**), $|S_{21}|$ and $\arg(S_{21})$ are plotted as calculated using the backaction model (see Eq. (2.25)). Panel (**g**) and (**g**), finally, show $|S_{21}|$ and $\arg(S_{21})$ calculated with the SAW model. The parameters used for the simulations are listed in the text and in Tab. 3.3. As magnitude and phase of S_{21} already contain the full information about ADFMR, we have renounced on the additional calculation of the power absorption with the SAW model.

As one can see from Fig. 3.11, the main features of the experimentally determined ADFMR signature are reproduced in the models[11]. Besides, the results obtained by the different ADFMR models are very similar, demonstrating that the presented modelling approaches are principally consistent. Therefore, for the detailed discussion of Rayleigh wave driven FMR in the rest of this section, we use the LLG and backaction model to reproduce the measured data. We renounce on showing the results from the more complex SAW model as they would give no additional insights into the physics of Rayleigh wave driven FMR.

For the comparison of shear and Rayleigh wave driven FMR (see Sect. 3.5), we use the SAW model as it inherently includes the different strains induced by SH and Rayleigh wave. Accordingly, the strains are not treated as fit parameters (as it is the case for the LLG and backaction model) but are directly determined in the SAW model calculations.

3.4.3 Angle-dependent ADFMR

In this section, the complete set of measurement and simulation data for the Rayleigh wave driven FMR experiments with Sample 1 is shown. In Fig. 3.12, the measured and simulated angle-dependence of ADFMR in IP configuration (cf. Fig. 3.5) is plotted for the 5^{th}, 9^{th} and 13^{th} harmonic frequency, corresponding to $\nu = 860\,\text{MHz}, 1.55\,\text{GHz}$ and $2.24\,\text{GHz}$.

The experimental data were obtained using the microwave power $P_0 = -10\,\text{dBm}$ and the IF bandwidth of $2\,\text{kHz}$ (at $860\,\text{MHz}$ and $1.55\,\text{GHz}$) resp. $1\,\text{kHz}$ (at $2.24\,\text{GHz}$).

As expected [48, 49], the resonance shifts to higher fields $\mu_0 H$ with increasing frequency, as can be seen in Fig. 3.12. For small frequencies, the quantitative agreement between simulation and experiment is very good, whereas for higher frequencies, P_{abs} and $|S_{21}|$ are overestimated in the simulations. The reason is that the fit parameters were chosen such that the phase quantitatively agrees with the experiment. The quantitative comparison of the magnitude then shows some deviations, but we observe a quite reasonable agreement as well.

Besides, we notice a slight asymmetry in the experimental data, which goes back to the contribution of the shear strain ε_{xz} and can be reproduced in the LLG model (see Sect. 2.1.4). For the backaction model, however, it is hard to consider a shear strain

[11] As explained in Sect. 3.3.1, the magnetic switching at about $\mu_0 H = 2\,\text{mT}$ is non-resonant and not accounted for in the ADFMR models.

	0.86 GHz	1.55 GHz	2.24 GHz
ε_{xx} (10^{-6})	1.8	1.15	0.36
ε_{xz} (10^{-6})	$0.09i$	$0.0575i$	$0.018i$
ε_{zz} (10^{-6})	0.18	0.115	0.036
F (d/λ)	0.26	0.35	0.38

Table 3.3: Frequency-dependent fit parameters used for the simulations in Fig. 3.11, 3.12, 3.13 and 3.14.

in addition to the dominant longitudinal strain ε_{xx}. Therefore, ε_{xz} was assumed to be zero yielding symmetric ADFMR signatures.

Regarding the phase of S_{21}, we experimentally observe phase shifts up to 115°. As explained in Sect. 2.2, the backaction model, as presented here, only holds in the limit of small interaction between SAW and FM, which implies a transmission $|S_{21}|$ near 1 and a phase shift which is small compared to 90°. Thus, the observed strong interaction between SAW and FM is beyond the validity of the backaction model.

In order to justify the disregard of the ferromagnetic exchange interaction in the ADFMR models (see Sect. 2.1.1), we calculate its contribution $\mu_0 \boldsymbol{H}_{\mathrm{ex}} \cdot \boldsymbol{m}$ to the free-enthalpy density G, which is given by Eq. (2.2). With $\mu_0 \boldsymbol{H}_{\mathrm{ex}} = D_{\mathrm{s}} \Delta \boldsymbol{m}$ [19, 45] and $D_{\mathrm{s}} = 2.1 \times 10^{-17}\,\mathrm{Tm}^2$ [64], we get a resonance shift of only 0.4 mT even at the highest examined SAW frequency $\nu = 2.24\,\mathrm{GHz}$. This is small compared to the other contributing terms in Eq. (2.2) and therefore does not change the ADFMR signature significantly.

In Fig. 3.13 and 3.14, the experimental and simulated ADFMR data are plotted for the OOP 1 and OOP 2 configuration. These data are one key result of this thesis, as to our knowledge no such SAW driven ADFMR experiments have been published before. For the calculation, the same set of parameters was used as for the IP configuration. Instead of the butterfly shape observed in IP configuration, we now see a cross-like signature, with an approximately four-fold symmetry as well. The small asymmetry with respect to the angle ψ is due to a slight misalignment of the sample, which was about 1.7° in OOP 1 configuration and 0.6° in OOP 2 configuration[12], and which could

[12]This means that the real rotation plane of the magnetic field was not exactly perpendicular but slightly tilted towards the film plane, which is due to an imprecise mounting of the sample in the rf dipstick. The misalignment could not be measured directly but was determined by fitting the rotation plane in the simulation to the measured ADFMR data.

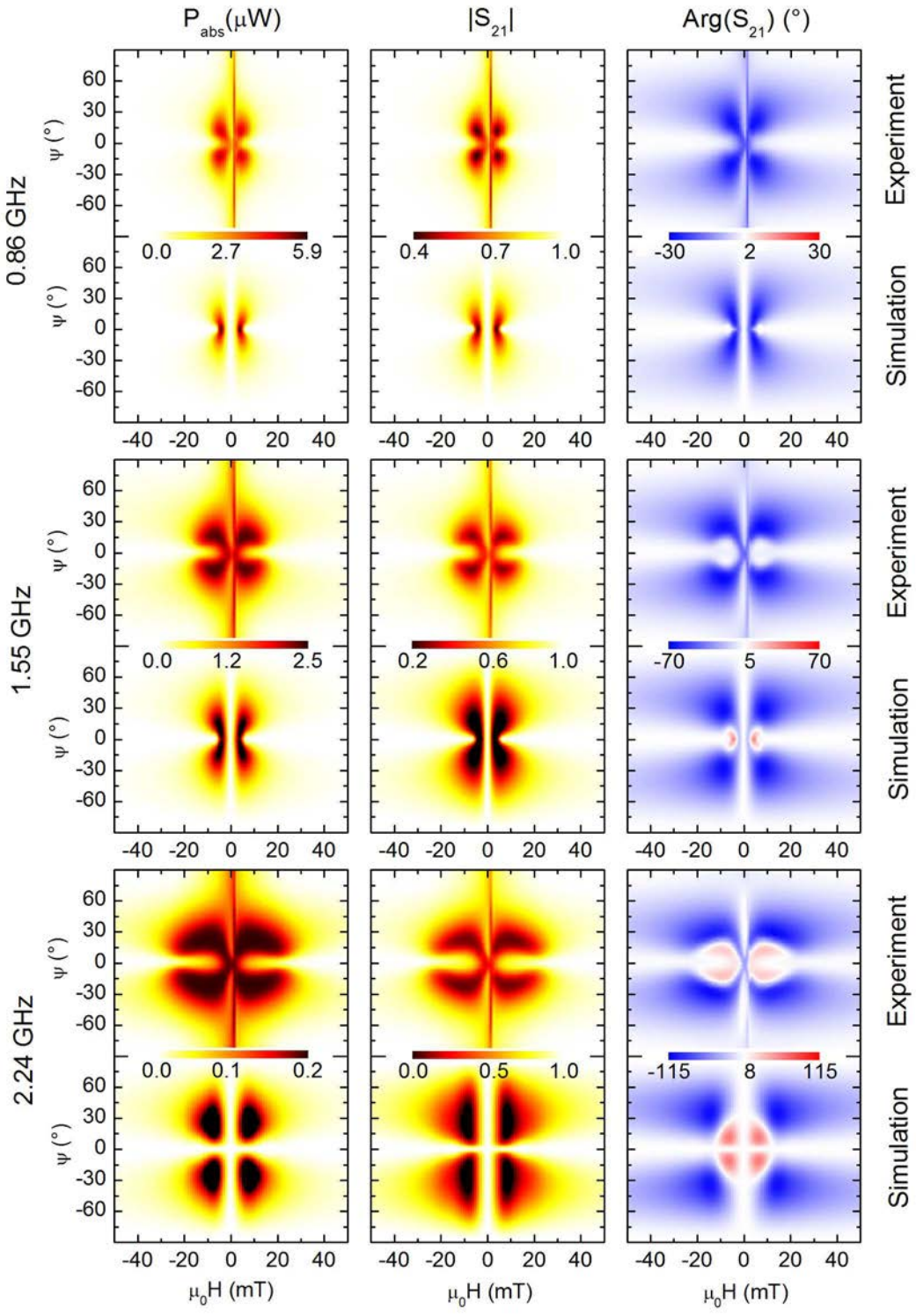

Figure 3.12: Measured and simulated angular-dependence of ADFMR in IP configuration (cf. Fig. 3.5) in Sample 1, for the SAW frequencies 860 MHz, 1.55 GHz and 2.24 GHz. The three columns show P_{abs}, $|S_{21}|$ and $\arg(S_{21})$ plotted versus magnetic field orientation and strength. The simulated power absorption was calculated using the LLG approach (see Eq. (2.12)), magnitude and phase of S_{21} were obtained from the backaction model (see Eq. (2.25)). The used parameters are listed in the text and in Tab. 3.3.

be reproduced in the simulation very well.

As in IP configuration, we observe a sign change of $\arg(S_{21})$ for higher frequencies, which is also reflected by the calculation results.

Comparing the strain estimated from S_{11} (see Fig. 3.9) with the fitted longitudinal strain listed in Tab. 3.3 shows a good agreement with deviations of 30% or less and confirms the choice of the fit parameters ε_{ij} a posteriori.

In conclusion, we observe an excellent agreement of the experimental data with the calculation results. Except from the damping parameter a, which has been discussed above, all simulation parameters have been chosen consistent with literature. Moreover, all investigated magnetic field configurations (IP, OOP 1 and OOP 2) were calculated using one set of parameters, which demonstrates the reliability of the presented ADFMR models.

3.5 Comparison of shear-horizontal and Rayleigh wave ADFMR

3.5.1 SAW transmission of Sample 2

Besides a detailed study of Rayleigh wave driven FMR on YZ-$LiNbO_3$, in this thesis the effects of the SAW type on the ADFMR signature were investigated. As already mentioned in Chap. 1, 36°YX-$LiTaO_3$ supports SH waves as well as Rayleigh waves, but the coupling factor κ^2 for the Rayleigh wave is about two orders of magnitude smaller than for the SH wave. Therefore, the Rayleigh wave mode is usually neglected in SAW applications. Nevertheless, by adjusting microwave power, IF bandwidth and other measurement parameters, it was possible to reduce the noise level sufficiently to get a clean ADFMR signal not only for the SH wave, but also for the Rayleigh wave in Sample 2. Thereby, for the latter, the transmission at 780 MHz (the 5^{th} harmonic of the Rayleigh fundamental frequency) was not more than −60 dB.

Figure 3.15 shows an overview of the transmission spectrum of Sample 2 (36°YX-$LiTaO_3$ with a 50 nm thin Ni film) with the frequencies indicated at which either Rayleigh or shear horizontal waves are excited. In Fig. 3.16, an enlarged view of the transmission spectrum around the 5^{th} harmonic of the Rayleigh wave and the 5^{th} and 9^{th} harmonic of the SH wave is shown. One can see that the Rayleigh wave is very

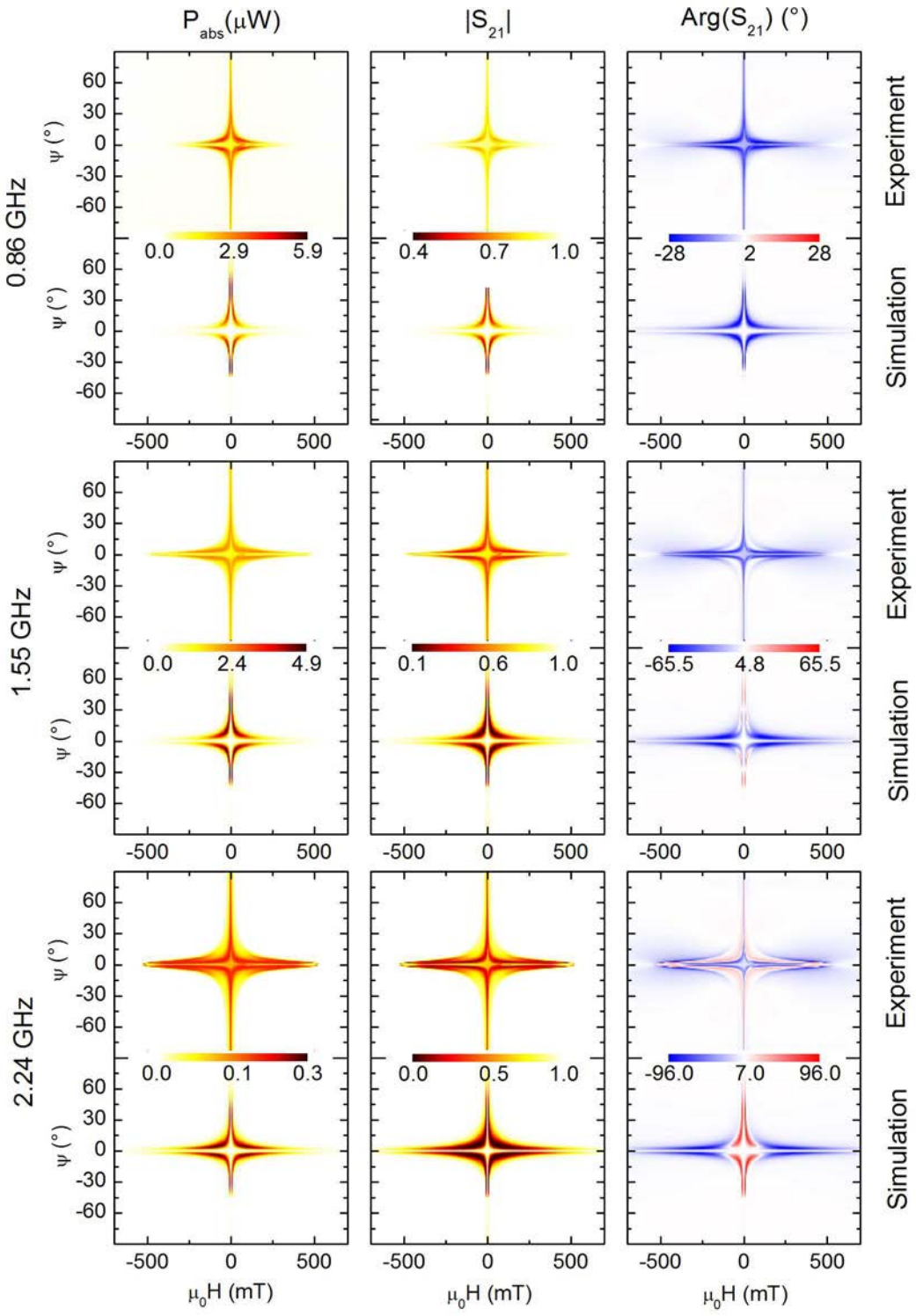

Figure 3.13: Measured and simulated angular-dependence of ADFMR in OOP 1 configuration (cf. Fig. 3.5) in Sample 1, for the SAW frequencies 860 MHz, 1.55 GHz and 2.24 GHz. The three columns show P_{abs}, $|S_{21}|$ and $\arg(S_{21})$ plotted versus magnetic field orientation and strength. The simulated power absorption was calculated using the LLG approach (see Eq. (2.12)), magnitude and phase of S_{21} were obtained from the backaction model (see Eq. (2.25)). The used parameters are listed in the text and in Tab. 3.3.

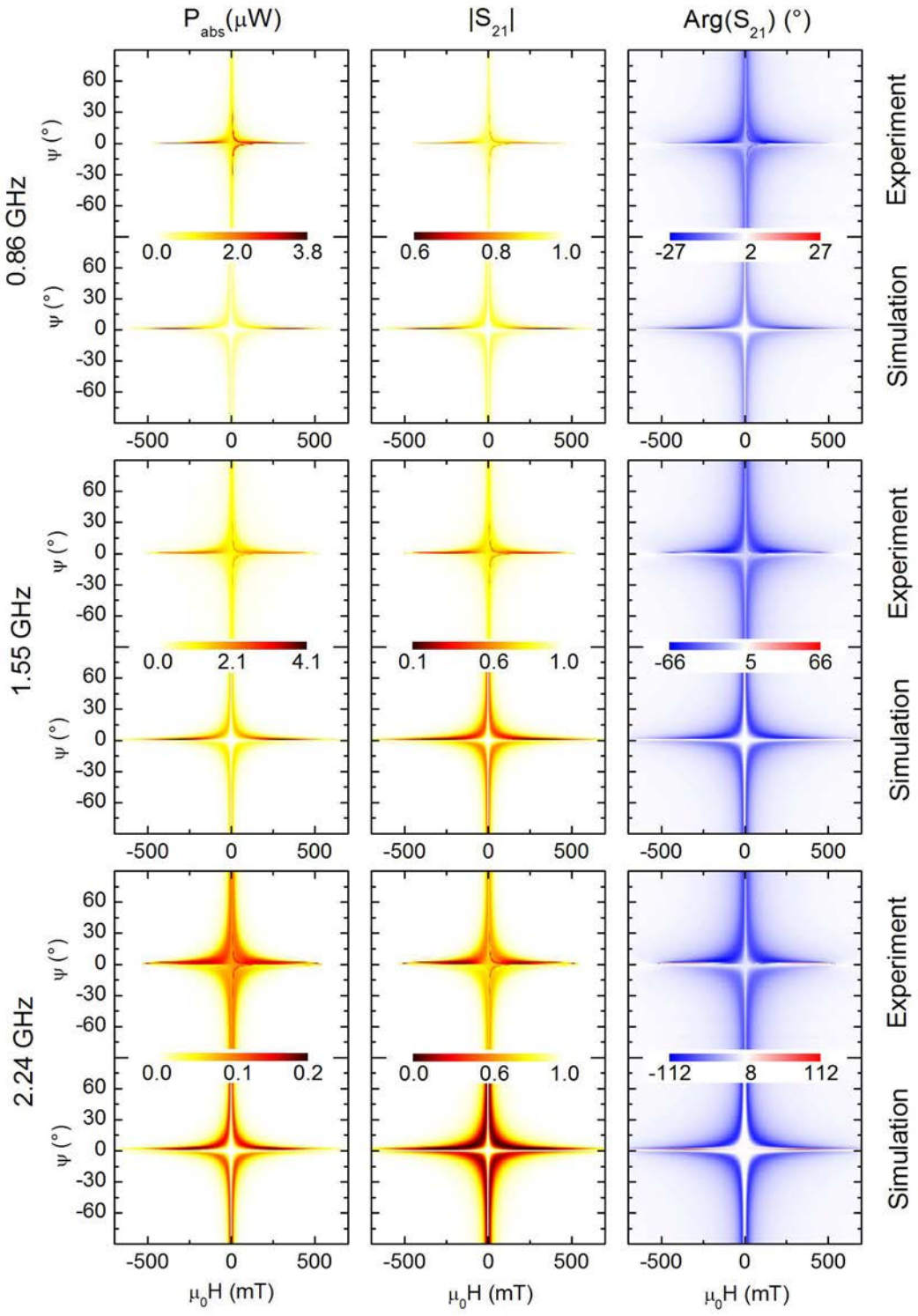

Figure 3.14: Measured and simulated angular-dependence of ADFMR in OOP 2 configuration (cf. Fig. 3.5) in Sample 1, for the SAW frequencies 860 MHz, 1.55 GHz and 2.24 GHz. The three columns show P_{abs}, $|S_{21}|$ and $\arg(S_{21})$ plotted versus magnetic field orientation and strength. The simulated power absorption was calculated using the LLG approach (see Eq. (2.12)), magnitude and phase of S_{21} were obtained from the backaction model (see Eq. (2.25)). The used parameters are listed in the text and in Tab. 3.3.

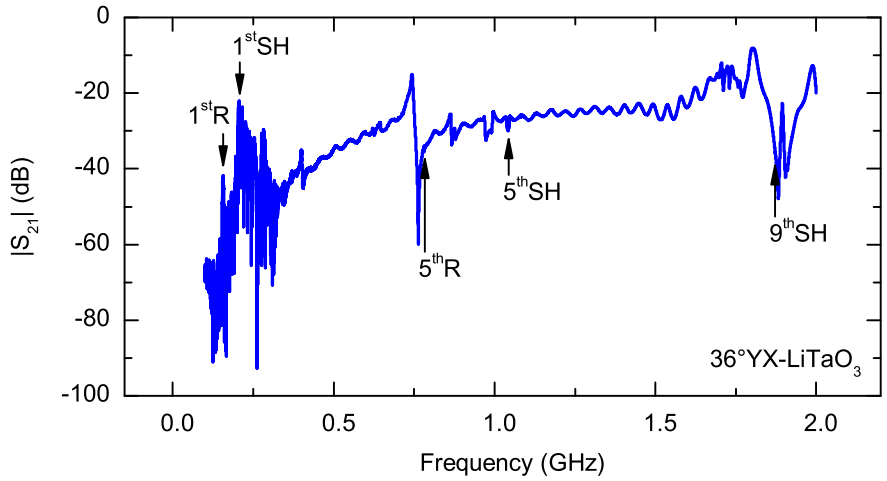

Figure 3.15: Transmission spectrum of Sample 2. The fundamental and the 5$^{\text{th}}$ harmonic of the Rayleigh wave (at 156 MHz and 780 MHz) are indicated, as well as the fundamental, 5$^{\text{th}}$ and 9$^{\text{th}}$ harmonic of the shear-horizontal wave (at 206 MHz, 1.04 GHz and 1.87 GHz). Similar to Fig. 3.10, there are other peaks stemming from resonances in the measurement setup.

weak compared to the SH wave at 1.04 GHz[13]. Nevertheless, Fourier transformation and time-gating, as described in Sect. 3.3.1, reveals a transmission maximum at about 780 MHz.

In order to demonstrate that we really observe two different surface wave types on one and the same sample, the transmission S_{21} for the passbands around 780 MHz, 1.04 GHz and 1.87 GHz is plotted as a function of time in Fig. 3.17. From the time-domain transmission, we can read off the delay t of the respective wave and in this way derive its speed of sound $c_{\text{sound}} = d_{\text{IDT}}/t$. The obtained values for t and c_{sound} are listed in Tab. 3.4. Comparing the sound velocities with literature data (e.g. [40]) shows that the wave excited at 780 MHz is Rayleigh-type, whereas the SAWs at 1.04 GHz and 1.87 GHz are SH waves.

3.5.2 Angle-dependent ADFMR

For a comparison between Rayleigh and SH wave driven FMR, the 5$^{\text{th}}$ harmonics of both wave types at 780 MHz resp. 1.04 GHz were studied in IP and OOP 1 configura-

[13]The 9$^{\text{th}}$ harmonic of the SH wave is very weak, too, but this is due to the fact that the SAW excitation efficiency of an IDT decreases for higher harmonics.

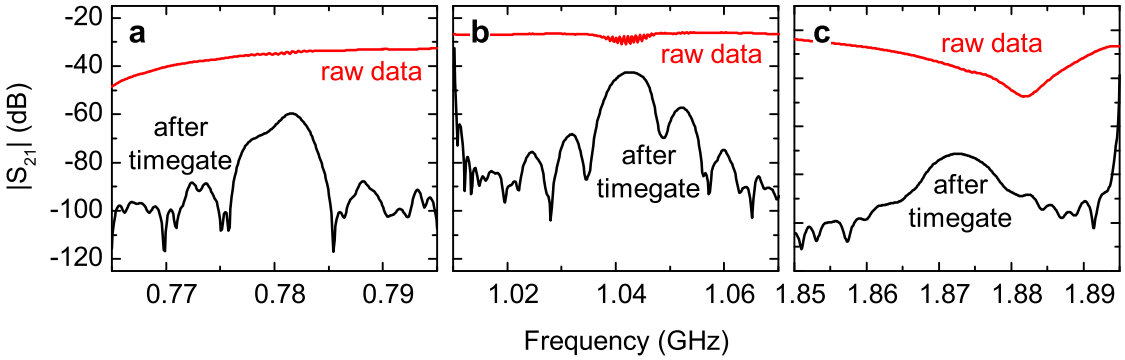

Figure 3.16: Magnitude of the SAW transmission of Sample 2 as a function of the microwave frequency ν for (**a**) the Rayleigh-wave passband around 780 MHz, (**b**) the SH-wave passband around 1.04 GHz and (**c**) the SH-wave passband around 1.87 GHz. The red and black lines show the raw and the time-gated transmission data, respectively.

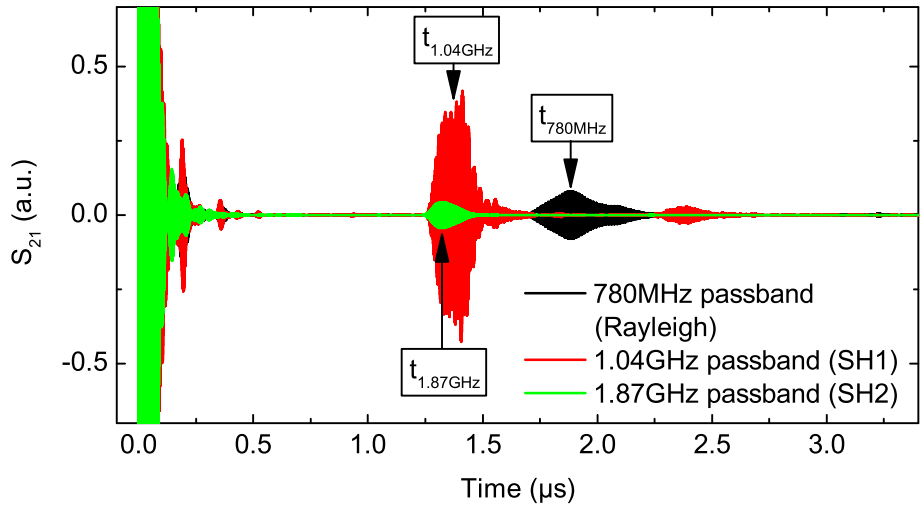

Figure 3.17: S_{21} as a function of time (Sample 2). The black, red and green line denote the SAW passbands around 780 MHz, 1.04 GHz and 1.87 GHz, respectively. This plot reveals different delay times of the examined SAWs and in this way allows to determine the type of the excited waves.

frequency ν GHz	delay t μs	c_{sound} m/s	wave type
0.78	1.89	$\approx 3.1 \times 10^3$	Rayleigh
1.04	1.38	$\approx 4.2 \times 10^3$	Shear horizontal
1.87	1.30	$\approx 4.4 \times 10^3$	Shear horizontal

Table 3.4: SAW delay t, determined from Fig. 3.17, and calculated sound velocity $c_{\text{sound}} = d_{\text{IDT}}/t$, with $d_{\text{IDT}} = 5.8\,\text{mm}$ (cf. Tab. 3.1). The wave type was found by comparing c_{sound} with the literature data in Tab. 3.2.

		5^{th} R	5^{th} SH	9^{th} SH	
frequency	ν	0.78	1.04	1.87	GHz
wavelength	λ	20/5	20/5	20/9	μm
VNA power	P_0	5	0	5	dBm
IF bandwidth		4	10	4	kHz

Table 3.5: Measurement parameters used for the Rayleigh and SH wave driven FMR experiments on Sample 2.

tion. For the IP configuration, also the 9^{th} harmonic of the SH wave at 1.87 GHz was investigated. The measurement parameters are listed in Tab. 3.5.

Figure 3.18 shows the experimentally determined angle-dependence of ADFMR in IP configuration, driven by Rayleigh and shear-horizontal wave and measured in Sample 2. It confirms the calculation results from Sect. 2.3.3 regarding the different angle-dependence of Rayleigh and SH wave driven FMR: While the Rayleigh wave FMR signature (first column in Fig. 3.18) resembles the ADFMR measurements on $LiNbO_3$[14] (cf. Figs. 3.12), SH wave FMR shows maximum signal at 0° and ±90° and a minimum around ±50°. This can be understood regarding the different angle-dependence of the virtual driving field $\mu_0 \boldsymbol{h}$, depending on the wave type, as discussed in Sect. 2.1.2.

Besides, SH wave driven FMR shows an astonishing behaviour regarding two as-

[14] As already mentioned in Sect. 1.4.3, the Rayleigh wave on 36°YX-$LiTaO_3$ is not completely equal to the one on YZ-$LiNbO_3$, so we do not expect a perfect agreement. In particular, on YZ-$LiNbO_3$, the only non-vanishing shear strain component is ε_{xz}, whereas on 36°YX-$LiTaO_3$, $\varepsilon_{xz} = 0$ with non-vanishing ε_{yz} and ε_{xy}. Therefore, the asymmetry in the ADFMR signature, which stems from the shear strains, looks different for the two crystals.

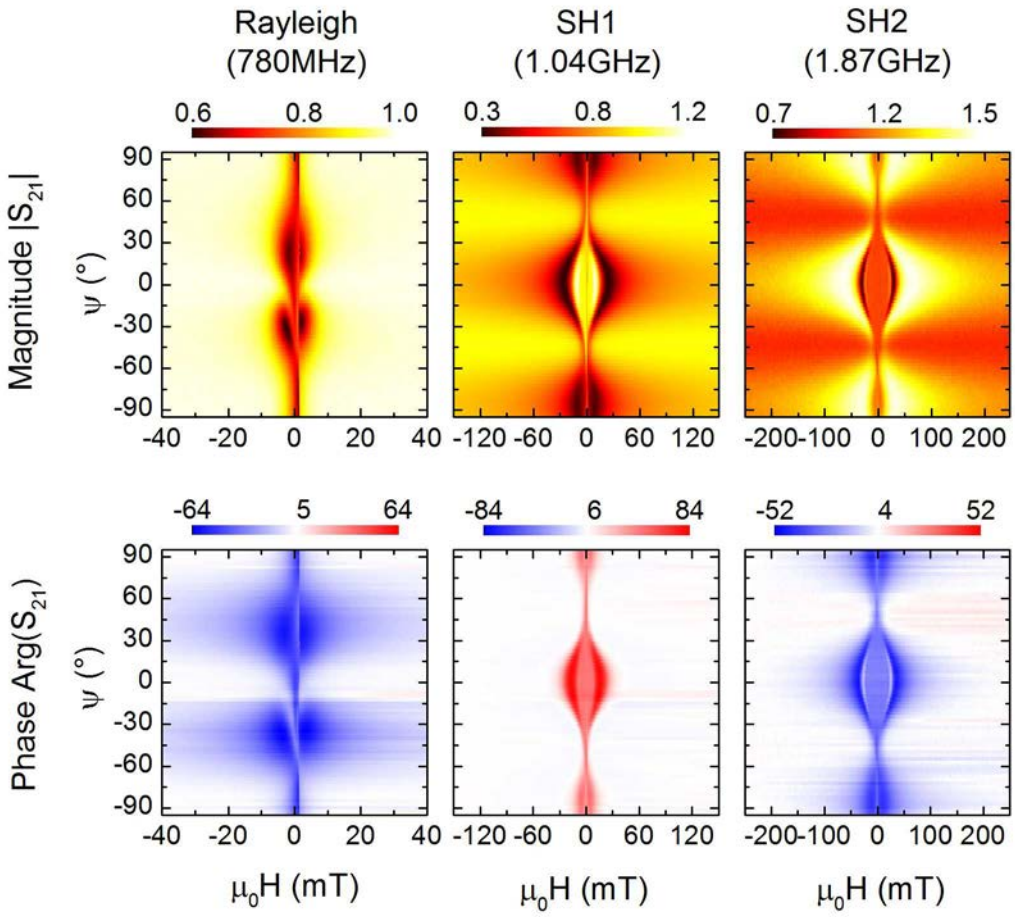

Figure 3.18: Measured angle-dependence of ADFMR in Sample 2 in IP configuration for Rayleigh wave (at 780 MHz) and SH wave (at 1.04 GHz and 1.87 GHz). In the first row, $|S_{21}|$ is plotted versus magnetic field orientation and strength, the second row shows $\arg(S_{21})$.

pects: First, we observe areas in Fig. 3.18, where the transmission magnitude $|S_{21}|$ clearly exceeds one. This means that the SAW propagation is effectively enhanced by interaction with the ferromagnetic film. The second aspect is that the 9$^{\text{th}}$ harmonic of the SH wave (at 1.87 GHz) shows to some extent the opposite behaviour of the 5$^{\text{th}}$ harmonic. Not only the sign of the phase shift is reverse (positive at 1.04 GHz, negative at 1.87 GHz; see also Fig. 3.19), also the broad resonance peaks at $\psi = 0$ and $\pm 90°$ are directed towards lower and higher transmission, respectively. Both observations do not appear in Rayleigh wave driven ADFMR and cannot be modelled yet. Nevertheless, we want to give some possible explanation approaches which could

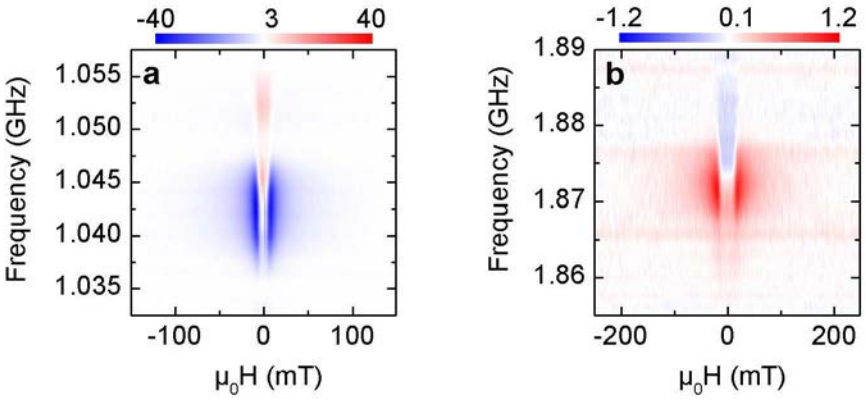

Figure 3.19: Shift of transmission, $\Delta|S_{21}| := |S_{21}| - |S_{21}|(\mu_0 H_{\text{off}})$, with respect to the external magnetic field, as a function of frequency (Sample 2). Panels (**a**) and (**b**) show the 5^{th} and the 9^{th} harmonic of the SH wave, respectively. $\mu_0 H_{\text{off}}$ was taken as $-150\,\text{mT}$ for the 5^{th} harmonic and $-250\,\text{mT}$ for the 9^{th} harmonic. As one can see, the field- and frequency-dependent phase shift looks very similar for 5^{th} and 9^{th} harmonic of the SH wave, except for the different sign.

account for these phenomena:

The observation of a normalized transmission coefficient $|S_{21}| > 1$ suggests that there are other, non-resonant damping mechanisms in addition to the resonant damping due to ADFMR. It seems plausible that the AC shear strains in the nickel film lead to a considerable mechanical damping, which occurs independently of FMR. This is not accounted for in the ADFMR models as we assume an ideal harmonic coupling between the nickel atoms without any dissipative terms. It is known [65–67] that in FMR the elastic constants of the FM can change; this phenomenon is called ΔE-effect [65]. According to [68], the relative variation of the elastic modulus of nickel can be up to 18% depending on the magnetization state. We thus speculate that the change in the material constants is such that it counteracts the dissipative terms and in this way reduces the effective damping of the acoustic wave in FMR. As the experimental data are normalized such that off resonance $|S_{21}| = 1$, this yields transmission values greater than 1 in FMR.

Another issue which has not been completely understood yet is the excitation and detection of shear waves using IDTs. For a Rayleigh wave the response of the piezoelectric crystal to the AC electric field of the IDT can easily be explained (see e. g. [43]), as the piezoelectric crystal is compressed and strained in the direction of the electric

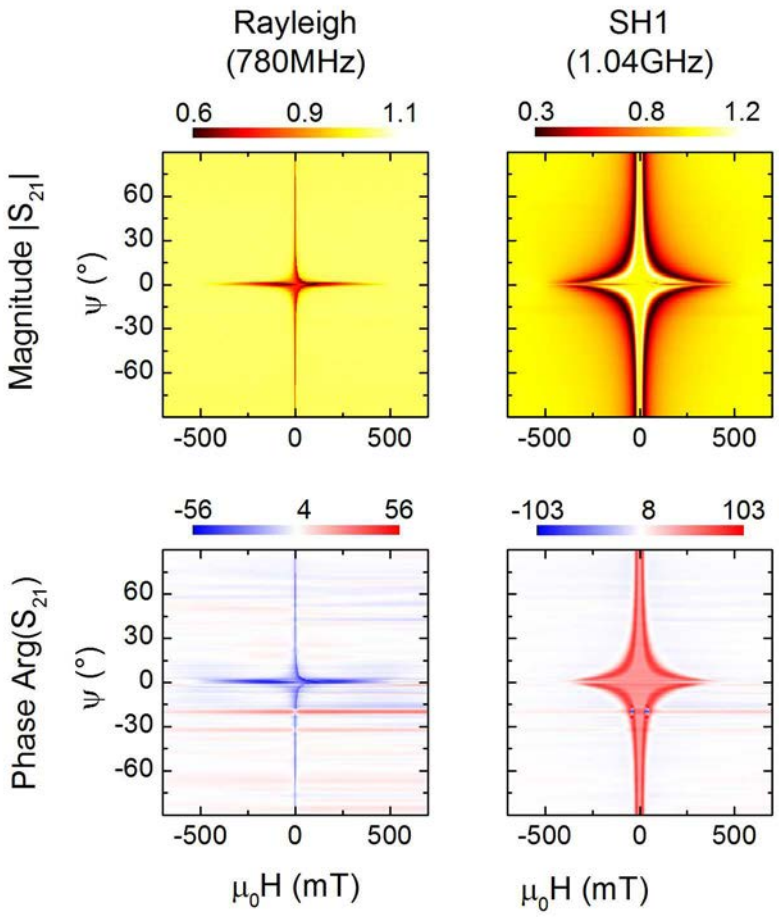

Figure 3.20: Measured angle-dependence of ADFMR in OOP 1 configuration for Rayleigh wave (at 780 MHz) and SH wave (at 1.04 GHz) in Sample 2. In the first row, $|S_{21}|$ is plotted versus magnetic field orientation and strength, the second row shows $\arg(S_{21})$.

field. For shear waves, however, the dominant displacement is *perpendicular* to the electric field direction. Hence, coupling between shear wave and electrical field is presumably mediated by a longitudinal/normal acoustic wave, which, however, decays exponentially along the surface. The surprising behaviour of the phase shift (see Figs. 3.18 and 3.19) is possibly due to such a rather complicated interaction mechanism of IDT and shear wave. To clarify this issue would require a further experimental and theoretical study of the working principle of IDTs for shear waves.

Concerning the OOP 1 configuration, which is plotted in Fig. 3.20, the difference between Rayleigh and SH wave FMR is less distinct. In both cases, we observe

a cross-like signature with its center at $\psi = 0$ (corresponding to $\boldsymbol{H} \parallel \boldsymbol{k}_{\mathrm{SAW}}$) and $\mu_0 H = 0$. Nevertheless, for a fixed angle ψ, the resonance fields of SH wave driven FMR are much higher than those of Rayleigh wave FMR. This again reflects the different angle-dependence of the virtual driving field for Rayleigh and SH wave.

The phase (second row in Fig. 3.20), shows similar angle-dependence as $|S_{21}|$, where the phase shift is negative for the Rayleigh wave and positive for the SH wave, as already observed in IP configuration.

3.5.3 Comparison of the experimental data to the SAW Model

Having shown the measured angle-dependence of Rayleigh and SH wave driven FMR in Sample 2, we use the SAW model to simulate the experimental data. Thereby, we do not have to make any assumptions concerning the strains induced by the different wave types, as it was necessary in the backaction model. The SAW model rather includes the calculation of the wave type based on the material constants of the crystal and the applied microwave frequency. Apart from the anisotropy parameters B_{u} and B_{d}, we thus have only two free parameters, the effective magnetoelastic coupling constant $\tilde{b}_1$ and the damping parameter a, which have to be fitted to the experimental data. Hereby, B_{u}, B_{d} and $\tilde{b}_1$ reflect the material system and the geometry of the sample and are therefore independent of wave type and frequency.

For the anisotropy parameters, we use $B_{\mathrm{u}} = 0.4\,\mathrm{mT}$ along $\boldsymbol{u} = \boldsymbol{x}$ and $B_{\mathrm{d}} = 350\,\mathrm{mT}$, the effective magnetoelastic coupling constant was chosen $\tilde{b}_1 = 8\,\mathrm{T}$ and the damping parameter a was 0.16 (for the Rayleigh wave at 780 MHz) resp. 0.5 (for the SH wave at 1.04 GHz). This set of parameters turned out to yield the best agreement with the experimental data.

Figures 3.21 and 3.22 show the measured and calculated transmission $|S_{21}|$ for the 5^{th} harmonic of Rayleigh and SH wave in IP and OOP 1 configuration. As one can see, the basic angle-dependence of Rayleigh and SH wave driven FMR can be reproduced in the simulations with one and the same set of parameters, but in detail there are still differences. Nevertheless, the experimentally determined and the calculated transmission $|S_{21}|$ differ by a factor of 1.5 at most, which makes it possible to use the same color code for both experiment and simulation in Figs. 3.21 and 3.22. Besides, for the simulation of IP and OOP 1 configuration, the same set of parameters was used, demonstrating the consistency of the model with the experimental data.

Concerning the deviations between experiment and simulation, there can be several

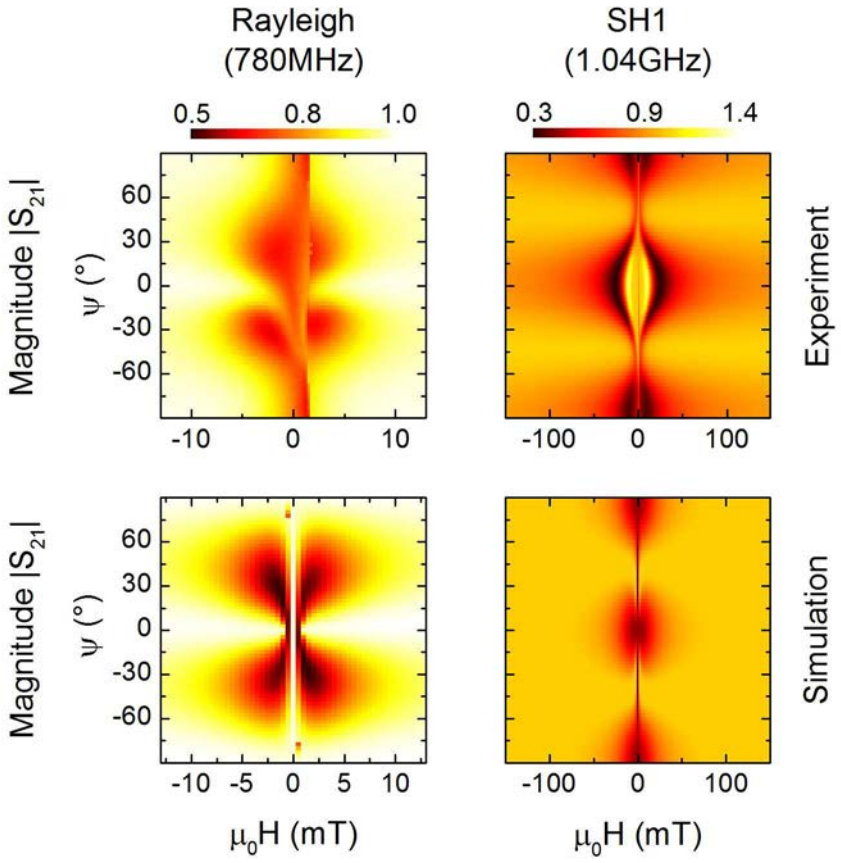

Figure 3.21: Comparison of measured and calculated ADFMR signature in IP configuration for Rayleigh wave (at 780 MHz) and SH wave (at 1.04 GHz) in Sample 2. The simulation results were obtained from the surface acoustic wave model as explained in Sect. 2.3. The parameters used for the calculation are given in the text.

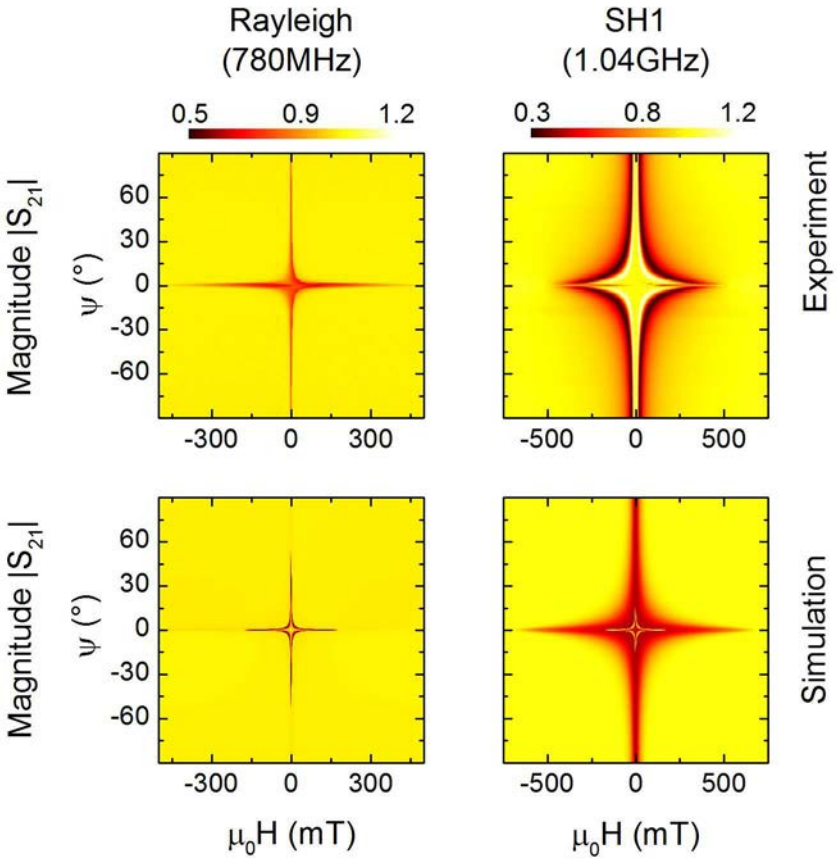

Figure 3.22: Comparison of measured and calculated ADFMR signature in OOP 1 configuration for Rayleigh wave (at 780 MHz) and SH wave (at 1.04 GHz) in Sample 2. The simulation results were obtained from the surface acoustic wave model as explained in Sect. 2.3. The parameters used for the calculation are given in the text.

reasons: First, the material parameters found in literature are not fully consistent, but show differences up to 10%. This affects the ADFMR calculation results as the displacements and strains induced by the SAW are determined by the exact material properties. Moreover, the crystal cut of the used $LiTaO_3$ substrate is given only with an accuracy of 1° and does not exactly match the ideal value found in literature, which is 34.7° for a metallized surface and 35.1° for a free surface. Also the alignment of the crystal edges and the IDTs regarding the crystal X-axis presumably comprises an error of some degrees. Finally, the conversion of an AC voltage into a SAW and vice versa in the IDTs brings about further uncertainties which are not accounted for in the ADFMR models.

3.6 Summary

In this chapter, the experimental ADFMR data have been presented and compared to the experiment. First, an extensive study of Rayleigh wave driven FMR on YZ-$LiNbO_3$ was given: We measured angle- and field-dependent ADFMR for three different frequencies between 860 MHz and 2.24 GHz and three measurement configurations (IP, OOP 1 and OOP 2), and showed that the experimental data can quantitatively be understood on the basis of the three ADFMR models introduced in Chap. 2. Considering that the original modelling and theory considerations by M. Weiler [16] were based on in-plane experiments only, the presented OOP 1 and OOP 2 measurements, studied for the first time in this thesis, are an important step forward, corrobating the current understanding of magnetoelastic interaction and ADFMR.

Furthermore, the symmetry break of the characteristic four-fold ADFMR signature, which was derived theoretically in Chap. 2, indeed could be observed in the experiment. Moreover, it has been shown, that the three ADFMR models yield very similar results and are therefore consistent in the limit of small interaction between SAW and FM. Nevertheless, they are different concerning range of validity, modelling sophistication and numerical complexity.

Besides, the effects of the SAW type on the ADFMR signature have been studied. To this end, a sample was fabricated which allows to measure Rayleigh and SH wave driven FMR at the same time in the same sample. We would like to stress that shear wave driven FMR has been reported in this thesis the first time. The fundamental differences – i. e. the observed different angle-dependence and the occurring symme-

tries – could be understood on the basis of analytical considerations (see Sect. 2.1.2) as well as numerical calculations. In detail, however, there are differences between experiment and simulation which have not been understood yet and therefore require further investigation.

Chapter 4

Tuneable surface acoustic wave resonator

4.1 SAW resonators and overview

All the ADFMR experiments presented in Chap. 3 have been performed on SAW delaylines. In other words, each sample consists of a pair of IDTs, which are used to launch and detect the SAW, respectively. As shown in Sect. 3.3.1, the SAW is partly reflected at the IDTs, which results in the observation of a triple transit SAW pulse (cf. Fig. 3.7b). Nevertheless, the reflexion coefficient of an IDT is comparatively small so that the SAW between IDT 1 and IDT 2 is mainly a travelling wave with propagation speed $v \approx 3 \times 10^3\,\mathrm{m/s}$. The amplitude of the SAW is determined by the microwave power P_0 input into IDT 1, the SAW excitation efficiency of the IDT (given by $\eta = |\Delta S_{11}|^2$, cf. Sect. 3.3.2) and the coupling coefficient κ^2 between elastic and electrical component of the SAW (cf. Sect. 1.4). Hereby, $|\Delta S_{11}|^2$ and κ^2 depend on the material system and cannot be increased directly, and P_0 is limited by the maximum current density supported by the IDT stripes.

In order to exceed these limitations and further increase the SAW amplitude one needs to go beyond the "simple" delayline concept. One attractive alternative are SAW resonators. ADFMR experiments using SAW resonators instead of conventional delaylines would entail several advantages:

First, due to the increase in mechanical displacement and induced strains, the ADFMR signal could be raised, yielding a better signal-to-noise ratio and simplifying measurement and evaluation techniques. Besides, very small ADFMR-related signals like acoustic spin pumping – DC as well as AC – could better be resolved and studied

in more detail.

Second, the increase in SAW amplitude could allow to exceed the range of small magnetization excitation $m_{1,2} \ll 1$ in order to observe and examine nonlinear effects in ADFMR and acoustic spin pumping.

Third, in a resonator, the reflected wave superimposes the wave launched by IDT 1, which results in a standing wave. It would be interesting to perform ADFMR experiments with standing waves instead of travelling waves, as this allows for spatially confined excitation and thus for spatially resolved ADFMR and spin pumping.

For ADFMR applications, it is essential to be able to tune the SAW resonator, which is explained in the following: The condition for constructive interference of incoming and reflected wave (*resonance condition*) is – independent of the type of resonator – given by[1]

$$2d = N\lambda, \qquad N \in \mathbb{N}, \tag{4.1}$$

where λ is the wavelength of the resonator wave and d the (effective) distance between the reflectors [25]. An additional load in the resonator changes the propagation speed of the wave and thus the wavelength λ (for fixed frequency). Such a load can be e. g. an additional capacity in an electromagnetic oscillating circuit, a magnetic solid in a microwave cavity or a ferromagnetic film on a SAW resonator. In particular, this implies that a SAW resonator well tuned in its "empty" configuration will not be appropriately tuned if a ferromagnetic thin film is evaporated onto it. Thus, the resonance condition Eq. (4.1) may not be satisfied any more in SAW resonators loaded with a FM. Therefore, we need a possibility to tune the resonator in-situ, i. e. to vary its acoustic length slightly, in order to satisfy Eq. (4.1).

Depending on the specific type of resonator, there are different ways of tuning. For electromagnetic oscillating circuits, e. g., this can be done by changing the capacity/inductivity of the circuit, and in a laser cavity, the distance between the mirrors can be adjusted. In a SAW resonator, however, the reflectors consist of lithographically defined gratings on the crystal surface and therefore the distance between the reflectors is fixed. A possibility to tune a SAW resonator would be to vary outer parameters like the temperature Θ, as the stiffness constants of the crystal and therefore also the sound velocity v changes with temperature. An estimation of the needed $\Delta\Theta$ is given in the outlook (Sect. 5.2).

[1] Here, we have assumed that the SAW reflectors cause a phase shift $\Delta\phi_{\mathrm{refl}} \in \{0, \pi\}$ each so that the total phase shift of the SAW pulse at both ends of the resonator is $\Delta\phi_{\mathrm{refl,ges}} = \Delta\phi_{\mathrm{refl},1} + \Delta\phi_{\mathrm{refl},2} \in 2\pi\mathbb{N}$.

The disavantage of tuning via temperature is that nearly all relevant material constants show a certain temperature dependence and so not only the speed of sound of the SAW but also the elastic and magnetoelastic properties of the ferromagnetic film change. Therefore it is desirable to work at constant temperature and vary the distance between the reflectors without changing any other material property, as realized in the present work.

Within the scope of this diploma thesis, it has been shown that a SAW resonator can be designed such that the reflectors are patterned on two independent crystals which are then assembled on a chipcarrier with an air gap of some millimeters in between, as indicated in Fig. 4.1. One of the crystals is fixed to the chipcarrier, while the other one can be moved with a piezoelectric actuator by some microns. To enable SAW propagation from one crystal to the other (across the air gap), a third, blank *bridge crystal* is added on top (see Fig. 4.1b). In the following, we will show that this design of a mechanically tuneable SAW resonator works and allows to tune the transmission $|S_{21}|$ over a wide range.

The outline of this chapter is as follows:

- First, we show that a SAW can effectively couple from one ferroelectric crystal into another which lies on top of the first.
- Then, a tuneable delayline is presented which allows the direct measurement of the distance variation via vector network analysis.
- Last, the tuneable SAW resonator is characterized. We observe strong variations in transmission amplitude and phase dependent on the voltage applied to the piezoelectric actuator.

The samples and experiments presented in this chapter have been made together with my bachelor student Alexander Späh. In his bachelor's thesis [69], the complete set of experimental data is shown whereas here only the most important results are presented.

4.2 Flipchip delayline

As a first step, we demonstrate that SAWs effectively couple from one ferroelectric crystal to another which is on top of the first as illustrated in Fig. 4.1. To this

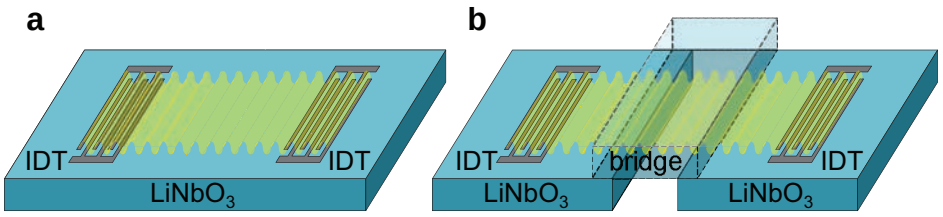

Figure 4.1: Schematic view of (**a**) a conventional delayline and (**b**) a flipchip delayline.

end, a delayline with two IDTs was fabricated on a YZ-$LiNbO_3$ crystal, which was subsequently cut in two equal pieces[2]. The crystal halves were aligned parallel and fixed on a chipcarrier, such that an air gap of about 1.1 mm separated them. Then another Y-cut $LiNbO_3$ crystal with dimensions 5×7 mm was set on top of the air gap with the polished side downwards and its Z-axis aligned parallel to the Z-axes of the crystal halves. The overlap of this bridge crystal with the delayline halves was approximately 2 mm on each side.

We refer to this unconventional delayline as the *flipchip delayline* in the following.

The flipchip delayline was characterized by measuring the complex transmission coefficient S_{21}, and compared to a standard delayline with the same fabrication parameters and $d_{\mathrm{IDT}} = 5.8$ mm. Electromagnetic crosstalk, triple transit and other spurious signal components were eliminated by application of a time gate, as described in Sect. 3.3.1. In Fig. 4.2, $|S_{21}|^2$ is plotted for both flipchip and conventional delayline at the fundamental SAW frequency 172 MHz and its 5^{th} harmonic.

Compared to the reference delayline, the transmission of the flipchip delayline is lower by about 2 dB and 4 dB at the fundamental frequency and its 5^{th} harmonic, respectively. Considering, that the SAW has to couple twice between two crystal surfaces lying on top of each other, the obtained transmission is remarkably high.

In conclusion, we see that the flipchip design works and that the loss of transmission compared to a conventional delayline is surprisingly low. This lays the foundation for further experiments with flipchip delayline and flipchip resonator.

[2]For the cutting process, we covered the crystal with a thick layer of photoresist to avoid damage to the polished surface.

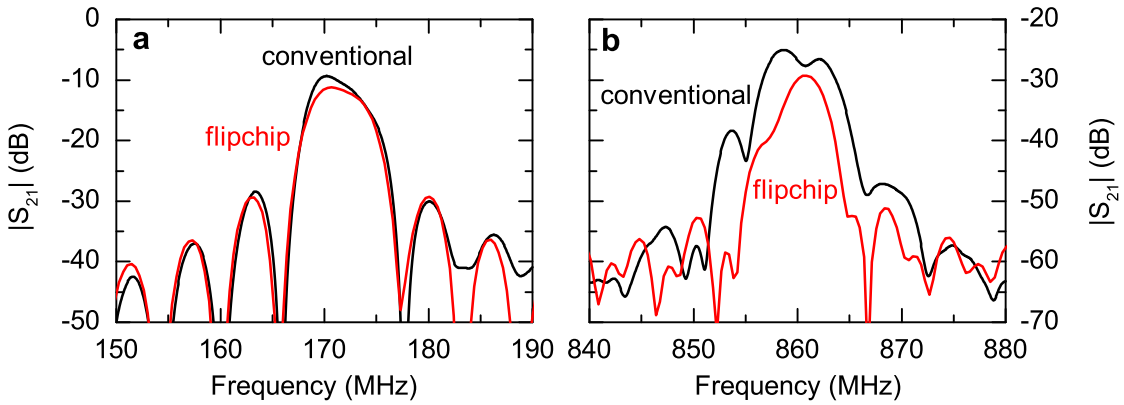

Figure 4.2: Magnitude $|S_{21}|^2$ of the complex transmission coefficient as a function of the microwave frequency for the flipchip delayline (red) and a conventional reference delayline (black). Here, the SAW passbands around (**a**) 172 MHz and (**b**) 860 MHz are shown.

4.3 Tuneable delayline

In order to show that the separation of the IDTs (resp. the air gap length) can be detected by vector network analysis, a tuneable delayline was fabricated (see Fig. 4.3). First, a pair of IDTs was patterned on a $6 \times 9\,\mathrm{mm}^2$ YZ-$LiNbO_3$ crystal, using the same IDT geometry and fabrication parameters as for the flipchip delayline. As above, the delayline was cut in two equal pieces. One of the crystal halves was fixed to the chipcarrier using the two-component adhesive *UHU plus sofortfest 2-K-Epoxidharzkleber*, the other piece was glued with its end face to a brass block fixed to one side of a piezoelectric actuator (*PSt 150/2x3/5* by Piezomechanik München GmbH, see [70]). The other side of the actuator was fixed to the chipcarrier using a second brass block. The bridge crystal was put on top of the 2.4 mm wide air gap, with an overlap of approximately 1.3 mm to the crystal halves, and pressed downwards using a brass clip. The pressure can be adjusted at two screws which connect the clip to the chipcarrier. The voltage V_{piezo} applied to the piezoelectric actuator is provided by a Keithley 2400 SourceMeter.

As in Sect. 4.2, the complex transmission S_{21} of the delayline was measured within the SAW passbands around 172 MHz and 860 MHz. The magnitude and the phase of S_{21} (after time gate) is plotted against the microwave frequency ν for three different piezovoltages in Figs. 4.4 and 4.5. The variation of $|S_{21}|$ with V_{piezo} is rather small, as

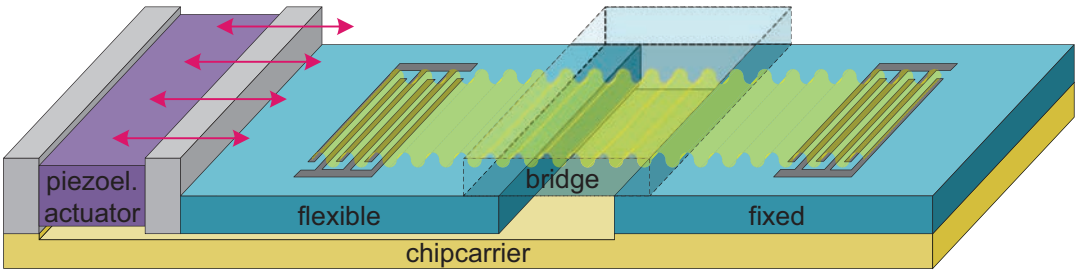

Figure 4.3: Schematic view of the tuneable delayline. For a photograph, we refer to Fig. 4.9, where the tuneable resonator, which is assembled similar to the tuneable delayline, is shown.

expected, while $\arg(S_{21})$ can be adjusted by 50° (at 172 MHz) resp. 240° (at 860 MHz).

To compare this to the stroke of the piezoelectric actuator, we consider that the change Δl in the delayline length is proportional to the phase shift $\Delta\varphi$ of the transmission coefficient S_{21}, and that a variation of l by a full wavelength, $\Delta l = \lambda$, corresponds to $\Delta\varphi = 360°$. Therefore, we have

$$\frac{\Delta l}{\lambda} = \frac{\Delta\varphi}{360°} \,. \tag{4.2}$$

According to its specifications [70], the expected stroke of the piezoelectric actuator is[3] $\Delta l_{\max} := l(V_{\text{piezo}} = 100V) - l(V_{\text{piezo}} = -30V) \approx 4.5\,\mu\text{m}$. Using Eq. (4.2), this corresponds to $\Delta\varphi_1 = 80°$ and $\Delta\varphi_5 = 400°$ for the fundamental frequency and the 5^{th} harmonic, respectively. Experimentally, we thus only observe about 60% of the phase change expected from the simple model.

The deviation between the experimentally determined phase shift and the calculated $\Delta\varphi$ can easily be rationalized as under mechanical load the (some ten microns thick) glued joints between crystal half, brass block, piezoelectric actuator and chipcarrier are deformed elastically by some percent of their thickness. Therefore, the real displacement of the flexible crystal half is less than the stroke Δl of the piezoelectric actuator.

Besides, the translation of IDT 2 can be observed directly using an optical microscope, as shown in [69]. The results obtained optically confirm the specifications of

[3] Strictly speaking, the specification of the maximum stroke $\Delta l_{\max}$, as given in [70], is valid only for vanishing load. Nevertheless, the maximum load force of the piezoelectric actuator is much higher than the estimated force applied in our case, so the stroke will be approximately the same as without load.

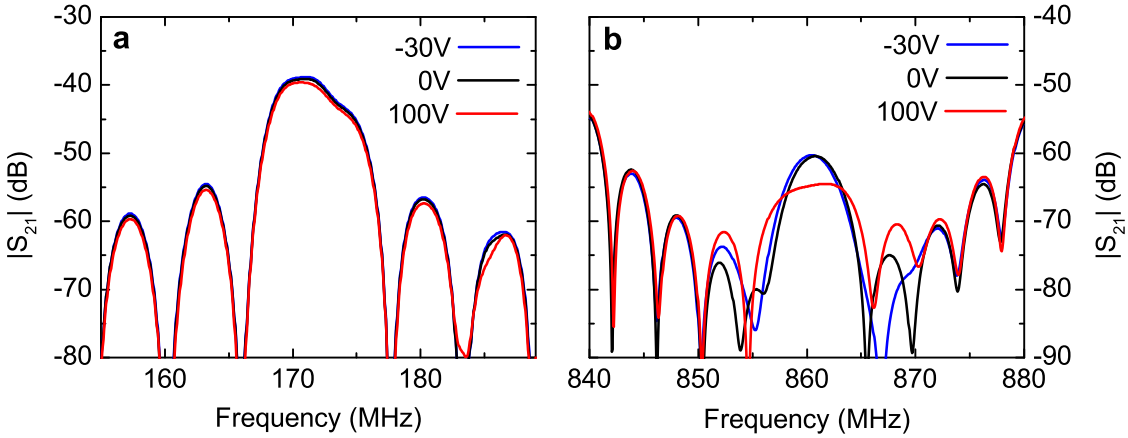

Figure 4.4: Frequency-dependence of the transmission magnitude $|S_{21}|$ for three different piezovoltages $V_{\text{piezo}} = -30, 0, 100\,\text{V}$ around (**a**) 172 MHz and (**b**) 860 MHz.

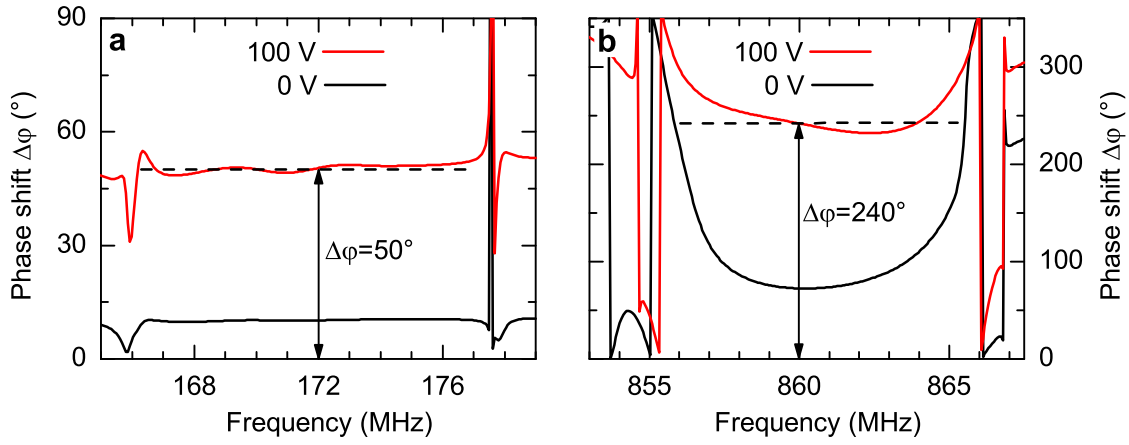

Figure 4.5: Frequency-dependence of the transmission phase shift $\Delta\varphi := \arg(S_{21})(V_{\text{piezo}}) - \arg(S_{21})(-30\,\text{V})$ for piezovoltages $V_{\text{piezo}} = 0\,\text{V}$ and $100\,\text{V}$ around (**a**) 172 MHz and (**b**) 860 MHz.

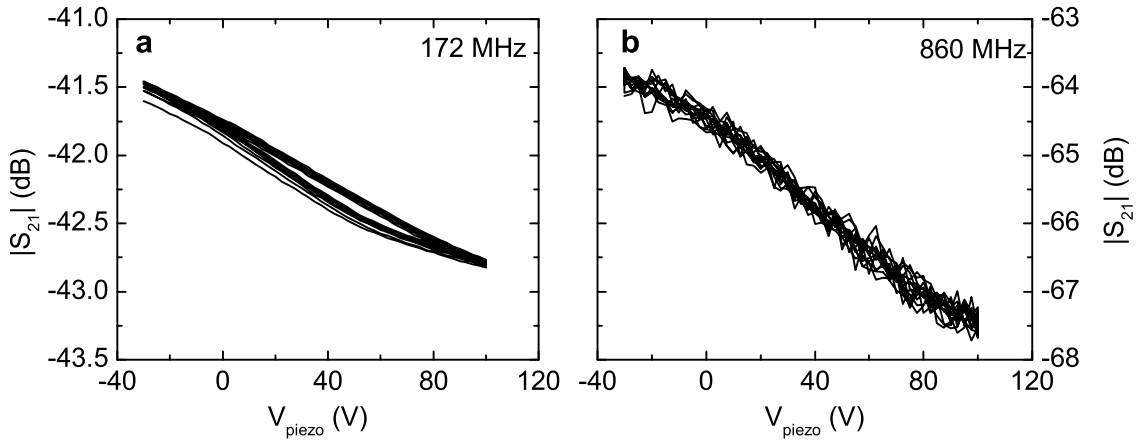

Figure 4.6: $|S_{21}|^2$ as a function of the piezovoltage V_{piezo} at (**a**) 172 MHz and (**b**) 860 MHz.

the piezoelectric actuator mentioned above, but cannot be directly compared to the measured $\Delta\varphi$ as they have been recorded without load. Nevertheless, it shows that the moving mechanism of the ferroelectric crystal works and that the maximum shift is of the expected order.

In order to examine the variation of S_{21} with V_{piezo} in more detail, we choose the center frequencies of the SAW passbands (172 MHz and 860 MHz, respectively) and plot $|S_{21}|$ and $\arg(S_{21})$ against the applied piezovoltage V_{piezo}, as shown in Figs. 4.6 and 4.7. Hereby, V_{piezo} was swept up and down between -30 V and 100 V several times. Figure 4.6 confirms the observation from Fig. 4.4 that $|S_{21}|$ only slightly depends on V_{piezo}. In contrast, the phase, plotted in Fig. 4.7, varies continuously over a wide range and shows a pronounced hysteresis loop, which results from the characteristic hysteretic behaviour of the piezoelectric actuator. This will be discussed later in more detail (see Sect. 4.4.4). Figure 4.7 demonstrates that a variation in the length of the delayline can quantitatively be detected by analysing the phase of S_{21}.

4.4 Tuneable resonator

Having shown the functionality of the tuneable delayline, we now turn to the tuneable SAW resonator. The design of the tuneable resonator, sketched in Fig. 4.8, is the same as for the tuneable delayline except for the lithography structure fabricated on the piezoelectric crystal halves. Here, we used IDTs with $N = 20$ finger pairs and a

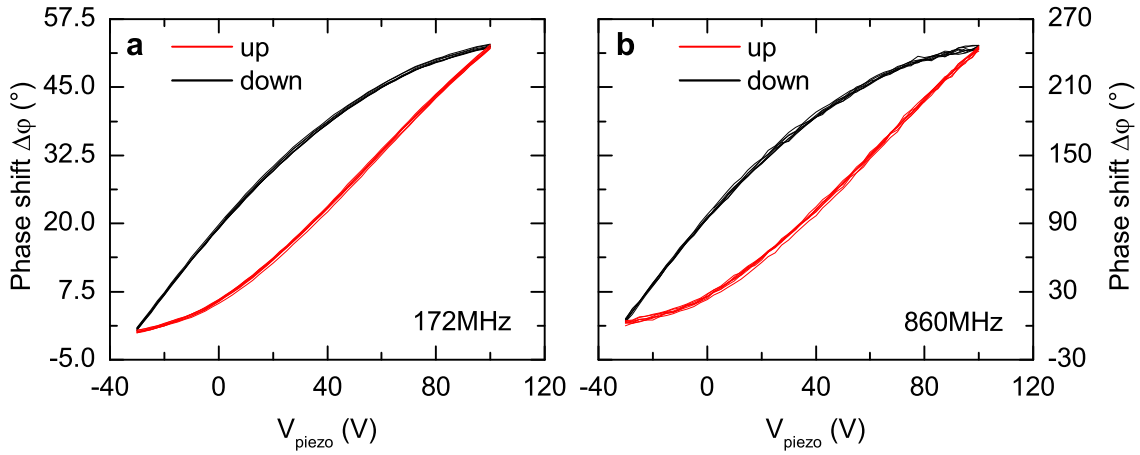

Figure 4.7: $\arg(S_{21})$ as a function of the piezovoltage V_{piezo} at (**a**) 172 MHz and (**b**) 860 MHz. The red and black lines refer to up- and downsweep, respectively.

periodicity $p = 20\,\mu$m and an additional reflective grating consisting of $5\,\mu$m wide aluminum stripes with a periodicity of $p' = 10\,\mu$m. The resonator design is that of a *conventional two-port resonator* [23]. This means that there are two IDTs for launching and detecting the SAW, respectively, located on the delayline *in-between* the reflective gratings[4]. Grating and IDT were fabricated in the same lithographical process. The distance between both is such that the fingers of the IDT are located exactly on the antinodes of the standing wave in the resonator, as explained, e. g., in [60, 69]. The grating stripes are shorted.

Similar to the tuneable delayline, one of the crystal halves is fixed to the chipcarrier, the other half can be moved with a piezoelectric actuator (model *PSt 150/2x3/5*), as can be seen from the photograph in Fig. 4.9. The air gap is about 1.9 mm. A brass clip presses the bridge crystal onto the resonator halves. On the chipcarrier, there are two mini-SMP connectors to which the IDTs are bonded. Using coaxial microwave cables, the sample is connected to a two-port VNA (Rohde & Schwarz ZVB 8). As above, the voltage applied to the piezoelectric actuator is provided by a Keithley 2400 SourceMeter.

[4] Compared to IDTs lying outside the reflectors (called *unconventional design*), the coupling of IDT and standing wave is much better for the conventional design, which simplifies the detection of the wave but slightly decreases the quality of the resonator [23]. For the first experiments with tuneable SAW resonators, however, the main focus was on the understanding of the working principle and not the optimization of the quality factor.

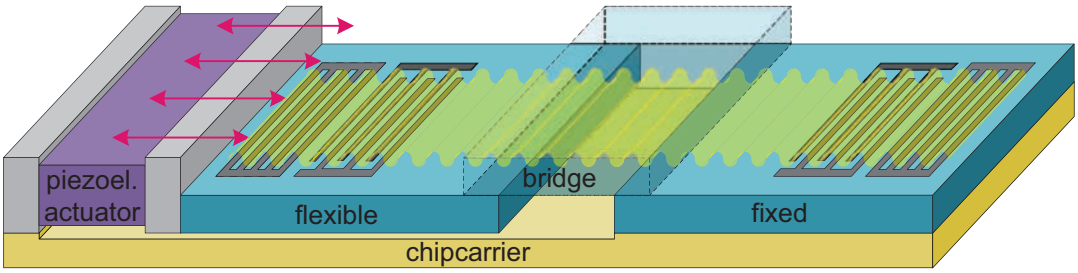

Figure 4.8: Schematic view of the tuneable resonator.

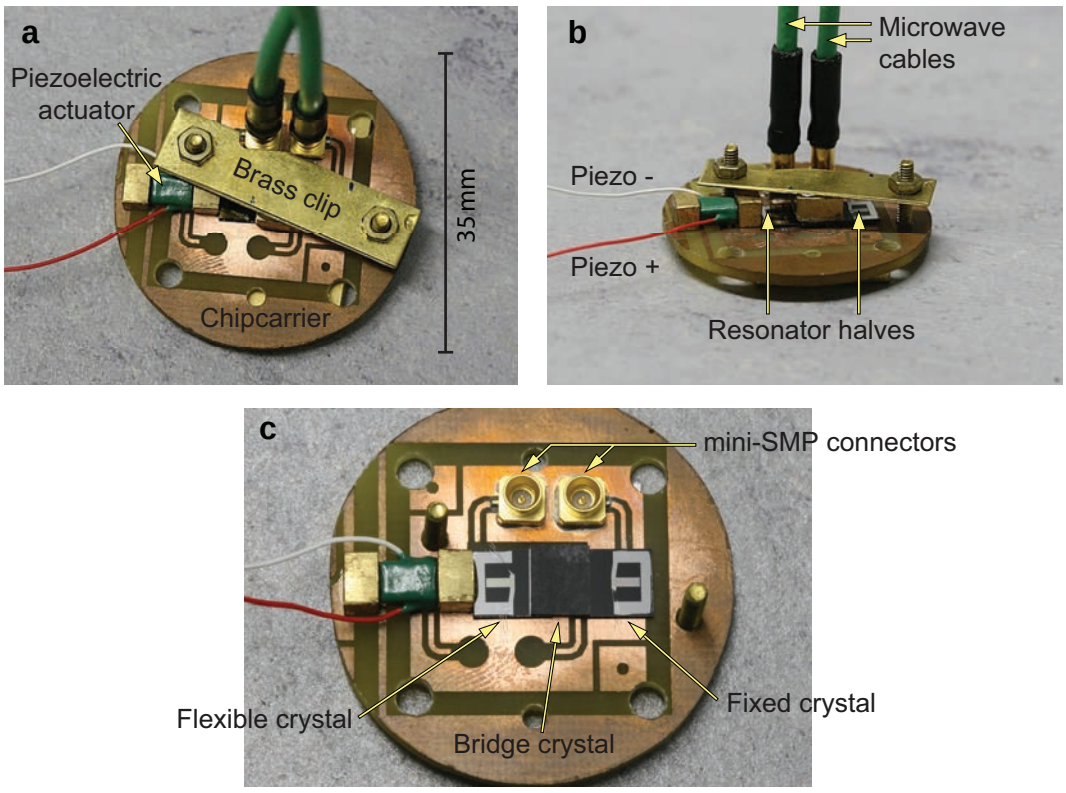

Figure 4.9: Photograph of the tuneable resonator. In (**a**) and (**b**), one can see a top and a side view of the complete assembly. For illustration purposes, (**c**) shows the tuneable resonator without the brass clip.

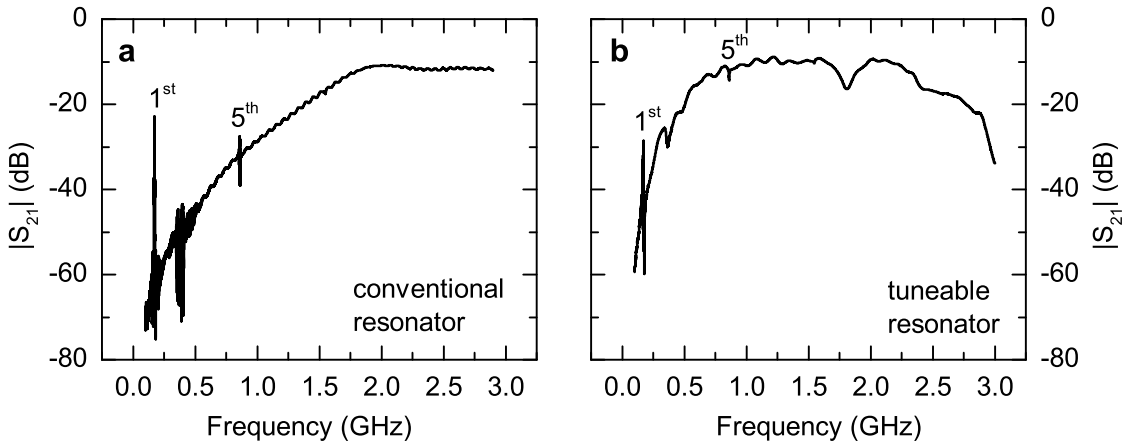

Figure 4.10: Transmission overview for (**a**) conventional and (**b**) tuneable resonator. The strong oscillations at 172 MHz and 860 MHz are assigned to the fundamental SAW frequency (denoted as 1^{st}) and its 5^{th} harmonic.

4.4.1 Transmission overview

For a first characterization, the transmission S_{21} of the tuneable resonator was measured and compared to the transmission of a conventional reference resonator in the same design. This is shown in Fig. 4.10 for a wide frequency range between 100 MHz and 3 GHz. As one can see, the peaks in SAW transmission at the fundamental frequency 172 MHz and its 5^{th} harmonic, 860 MHz, are still visible in the tuneable resonator but less clear than for the conventional resonator.

4.4.2 Application of a time gate

For a more detail study, we regard the SAW passbands around 172 MHz and 860 MHz and apply the time-gate data processing explained in Sect. 3.3.1 to extract the main SAW pulse from the measured transmission data. For two reasons, this is more complicated here than for a conventional delayline. First, in a resonator, reflections of the SAW at the gratings and thus SAW pulses of higher order are desired and may not be excluded by time-gating. Therefore, we have to set $t_{\text{stop}} = \infty$. With that, spurious signals like the electromagnetic crosstalk of a reflected SAW pulse cannot be excluded via time-gating any more. The second issue is that due to the flipchip design, there are a lot of substrate edges acting as SAW reflectors. These reflections are unwanted as they incoherently superimpose the standing resonator wave, but

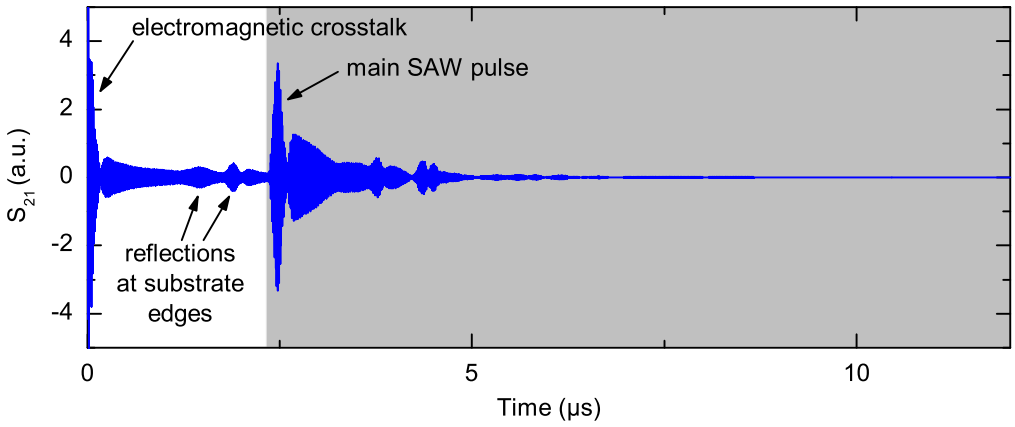

Figure 4.11: SAW transmission S_{21} as a function of time. The shadowed area indicates the time gate applied to the measured data, i. e. only the S_{21} signal for $t > 2.3\,\mu$s is used in the analysis. As one can see, the electromagnetic crosstalk and early reflections of the SAW at substrate edges can be excluded, but there are several more signal components superimposed which can not be separated from the main SAW pulse and the main reflections in time-domain.

cannot be separated from the standing wave in time-domain.

Figure 4.11, showing a timetrace of the tuneable resonator, makes clear that there are a lot of signal components overlapping in time domain, which therefore cannot be separated completely. As a consequence, the application of a time gate improves the measured transmission data S_{21}, but does not allow to eliminate all interfering contributions, as it was the case for the ADFMR experiments.

4.4.3 SAW transmission and comparison to conventional resonator

In Fig. 4.12, the transmission data of conventional and tuneable resonator are compared (after application of the time gate, as explained in Sect. 4.4.2). We can see that especially at the fundamental frequency the difference between tuneable and conventional resonator is fairly small. In particular, the narrow maximum around 171.5 MHz and width of about 1 MHz, which is a characteristic of SAW resonators [23], occurs for the conventional as well as for the tuneable SAW resonator.

At 860 MHz, we observe a more complicated frequency-dependence which presumably has to be described as an interference of the broad SAW passband maximum

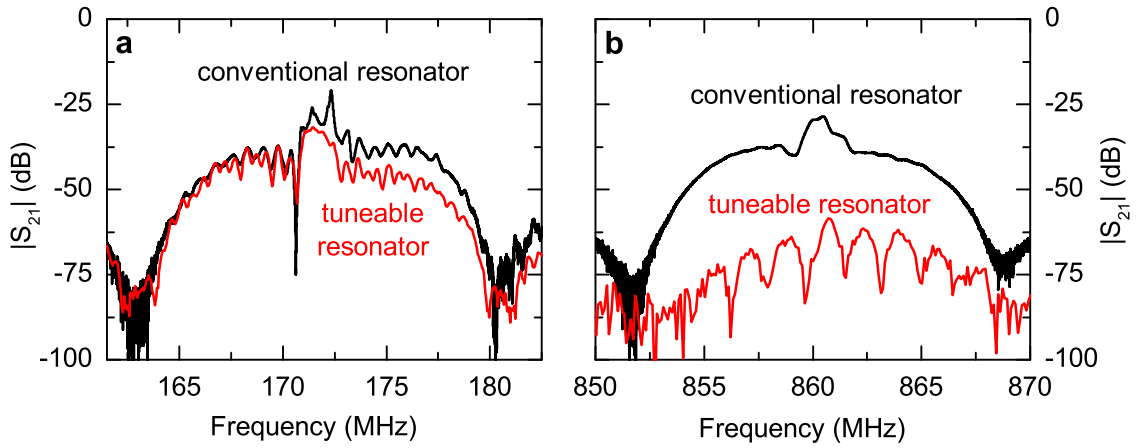

Figure 4.12: SAW transmission of tuneable (red line) and conventional (black line) SAW resonator around (**a**) 172 MHz and (**b**) 860 MHz.

and the narrow resonator maximum with some unwanted reflections.

Regarding the fact that a single SAW pulse has to couple between the bridge crystal and one of the crystal halves four times per oscillation period, the loss in transmission seems fairly low.

4.4.4 SAW transmission as a function of V_{piezo}

In order to study how the SAW transmission changes with V_{piezo}, S_{21} was measured as a function of ν for three different piezovoltages $V_{\text{piezo}} = -30, 80, 150\,\text{V}$ and plotted in Fig. 4.13. For the fundamental SAW frequency (Fig. 4.13a), we observe a slight change in $|S_{21}|$, which is not constant over the whole passband, but depends on the frequency (and even changes sign with ν). At 171.1 MHz, e. g., we have $\Delta|S_{21}| := |S_{21}(150\,\text{V})| - |S_{21}(-30\,\text{V})| = 6 \times 10^{-3}$, whereas at 171.4 MHz and 171.8 MHz, we get $\Delta|S_{21}|' \approx 0$ and $\Delta|S_{21}|'' \approx -3 \times 10^{-3}$, respectively. At the 5^{th} harmonic, $|S_{21}|$ shows a variation in magnitude as well as a shift in frequency when sweeping V_{piezo}. The reason for this shift is most probably an interference of the main SAW pulse and its higher orders with secondary crosstalk and undesired reflections, which can only partially be eliminated by time-gating, as explained in Sect. 4.4.2. It is known, that for the fundamental frequency, the effects of these spurious signal components are less severe than for the higher harmonics (cf. [57]).

To be able to better distinguish between shifts on the frequency axis and varia-

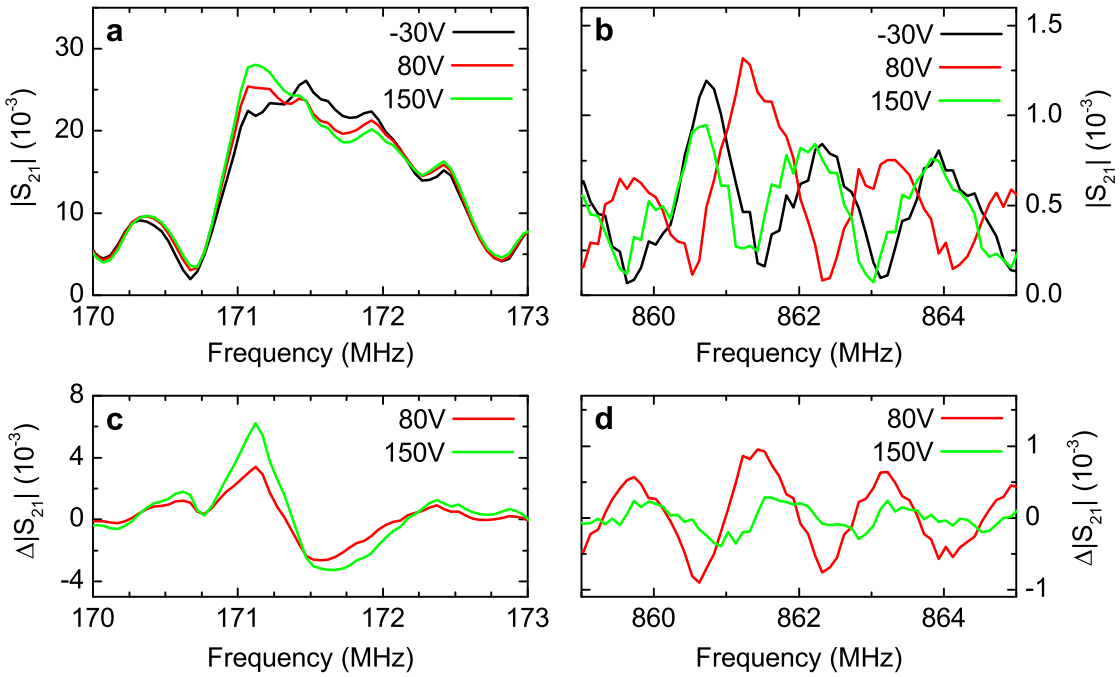

Figure 4.13: Transmission magnitude as a function of ν for $V_{\text{piezo}} = -30, 80, 150\,\text{V}$. Panel (**a**) and (**b**) show $|S_{21}|$ for the fundamental and 5^{th} harmonic SAW frequency. In (**c**) and (**d**), the change in transmission, $\Delta|S_{21}| := |S_{21}(V_{\text{piezo}})| - |S_{21}|(-30\,\text{V})$, is plotted for the two SAW passbands.

tion of amplitude, $|S_{21}|$ is plotted against frequency and V_{piezo} in Fig. 4.14. As one can see from Fig. 4.14a, there is – on top of the broad maximum of the SAW passband from 165 MHz to 177 MHz – another maximum (which is characteristic for a resonator, as explained above) at 170.9 MHz with a width of about 1 MHz. The shape of this maximum changes slightly when varying V_{piezo}: At $V_{\text{piezo}} = -30\,\text{V}$, we observe a maximum in transmission, $|S_{21}|_{\text{max},1} = 26 \times 10^{-3}$, at $\nu_{\text{max},1} = 171.45\,\text{MHz}$, which decreases and finally disappears for increasing V_{piezo}, while at a slightly lower frequency, at $\nu_{\text{max},2} = 171.10\,\text{MHz}$, a new maximum arises, which at $V_{\text{piezo}} = 150\,\text{V}$ reaches $|S_{21}|_{max,2} = 28 \times 10^{-3}$.

For the 5^{th} harmonic, shown in Fig. 4.14b, the behaviour of $|S_{21}|$ seems more complicated. Within the SAW passband between 855 MHz and 867 MHz, we observe a superposition of the broad passband maximum with some reflection/crosstalk contributions resulting in an interference pattern like $|\sin(\nu)/\nu|$. This characteristic pattern shifts to higher frequencies by approximately 1.7 MHz when increasing V_{piezo}

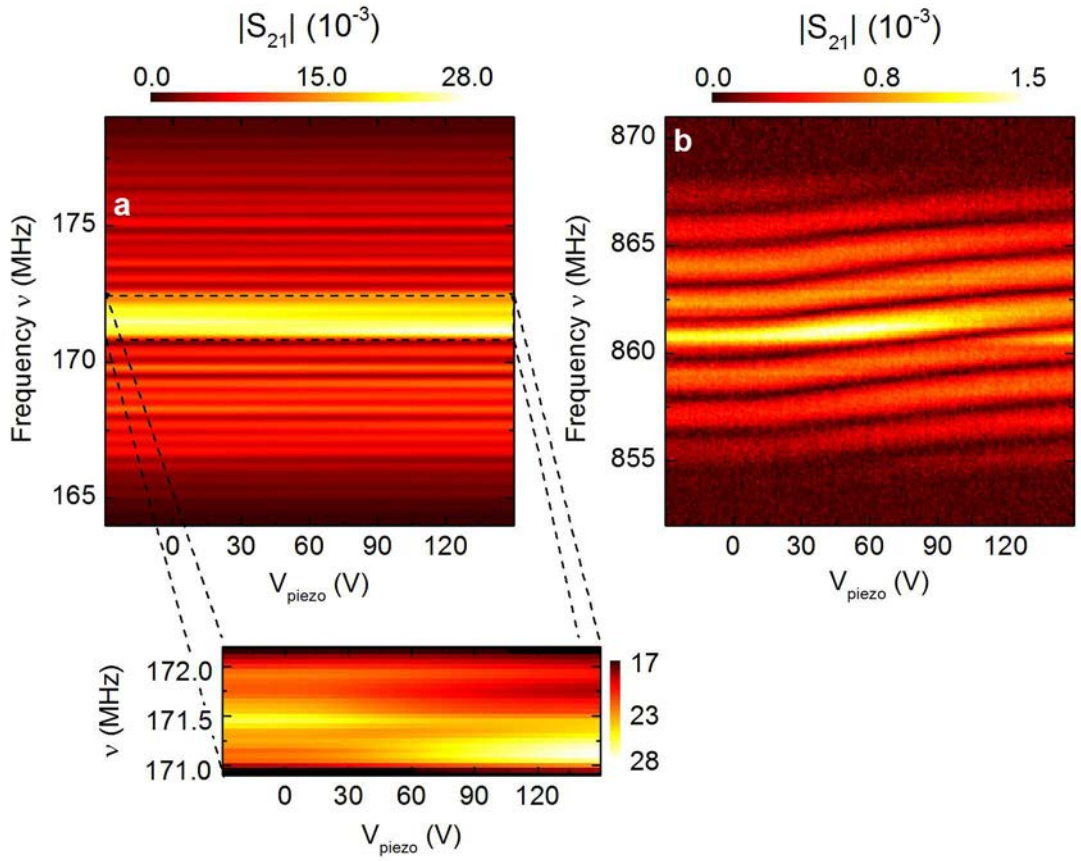

Figure 4.14: Transmission $|S_{21}|$ plotted against frequency ν and V_{piezo} for the SAW passbands around (**a**) 172 MHz and (**b**) 860 MHz.

from $-30\,\text{V}$ to $150\,\text{V}$[5]. The reason for this shift will be discussed below. Besides, we find a pronounced transmission maximum $|S_{21}|_{\text{max}} = 1.47 \times 10^{-3}$ at 861.07 MHz and $V_{\text{piezo}} = 57\,\text{V}$, while towards higher and lower piezovoltage, transmission decreases to $|S_{21}|'_{\text{max},1} = 1.18{\times}10^{-3}$ at $V_{\text{piezo}} = -30\,\text{V}$ and $|S_{21}|'_{\text{max},2} = 9.88{\times}10^{-4}$ at $V_{\text{piezo}} = 150\,\text{V}$, respectively.

In order to show the hysteretic behaviour of $|S_{21}|$ as a function of V_{piezo}, S_{21} has been measured for seven up- and downsweeps of V_{piezo}, covering the range from $-30\,\text{V}$ to $150\,\text{V}$. In Fig. 4.15, the V_{piezo}-dependence of $|S_{21}|$ at the center frequencies 171.12 MHz and 861.03 MHz is plotted, where we have averaged over all upsweeps and all downsweeps, respectively.

As expected, up- and downsweep differ remarkably due to the hysteretic behaviour

[5]Please note that only the interference maxima and minima shift with increasing V_{piezo}, but not the enveloping SAW passband.

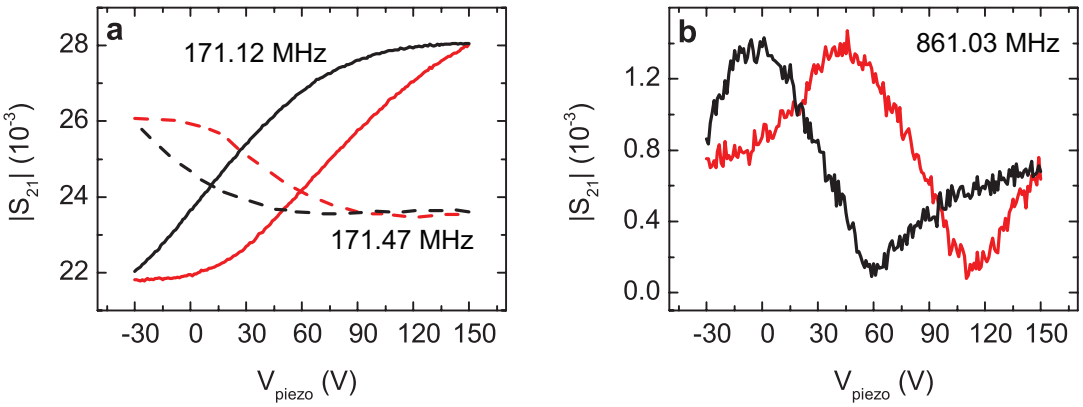

Figure 4.15: Transmission $|S_{21}|$ as a function of V_{piezo} for (**a**) 171.12 MHz (solid line) resp. 171.47 MHz (dashed line) and (**b**) 861.03 MHz. The reason for the different shapes of solid and dashed curve in Panel (**a**) is given in the text.

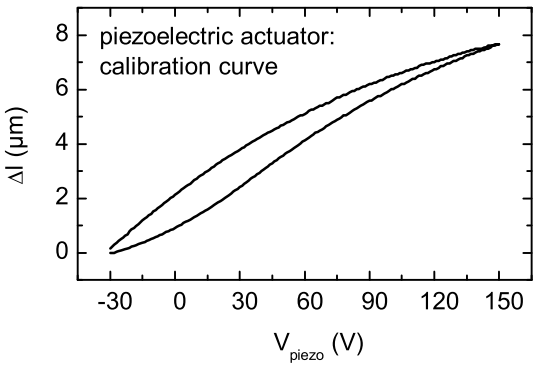

Figure 4.16: Stroke of piezoelectric actuator *PSt 150/2x3/5* dependent on applied voltage V_{piezo} (taken from [72]).

of the piezoelectric actuator: Its stroke Δl as function of V_{piezo} is not unique but depends on the pretreatment of the actuator, in particular on the sweep direction when varying V_{piezo}. The piezoelectric actuator hysteresis loop has been measured by A. Brandlmaier [71, 72], and is shown in Fig. 4.16. Nevertheless, we renounce on a direct comparison of Figs. 4.16 and 4.15 as the hysteresis loop of the tuneable resonator (Fig. 4.15) is additionally broadened by the elastic deformation of the glued joints, as explained above.

Besides, it should be mentioned that the shape of the hysteresis loops in Fig. 4.15 sensitively depends on the particular frequency ν chosen. To illustrate this, Fig. 4.15a also shows the transmission $|S_{21}|$ for a slightly higher frequency, 171.47 MHz (dashed

line). The completely different shape of the solid and dashed curve is not surprising and can be understood as follows:

The ratio $2d/\lambda = 2d \times \nu/c_{\text{sound}}$, which is the number of wave trains in the resonator (cf. Eq. (4.1)), depends on the frequency ν as well as the resonator length d. Therefore, the optimum resonator length d_{opt}, which fulfills the resonance condition $2d/\lambda \in \mathbb{N}$, varies with the frequency ν chosen. As $|S_{21}|(d)$ takes its maximum where the resonance condition is fulfilled, also the maxima of $|S_{21}|(d)$ shift for different ν. Hence, Fig. 4.15a shows different sections out of a full tuning period, with the particular phase of the section depending on the frequency ν.

In the above discussion, we studied the variation of the magnitude of S_{21} with frequency and V_{piezo}. Analogously, the phase $\arg(S_{21})$ can be analysed. A detailed discussion of the phase can be found in [69]. Here, it should be mentioned that plotting $\arg(S_{21})$ as a function of V_{piezo} results in hysteresis loops similar to Fig. 4.15, with the shape of the hysteresis loop depending on the frequency ν chosen.

4.5 Summary

In this chapter, it has been shown that it is possible to fabricate a tuneable surface acoustic wave resonator using the above explained flipchip design. To this end, preliminary experiments have been been performed with a flipchip sample and a tuneable delayline. We could demonstrate that the SAW effectively couples between piezoelectric crystals lying on top of each other, with a loss of transmission which is only 2 dB (at 172 MHz) resp. 4 dB (at 860 MHz). Using the tuneable delayline, we demonstrated that the stroke of the piezoelectric actuator can be detected by vector network analysis, measuring the phase shift of S_{21}. We observed an agreement of the measured phase shift $\Delta \arg(S_{21})$ with the expected stroke of the piezoelectric actuator, considering the fact that the elastic deformation of the glued joints reduces the effective shift of the crystal halves to each other.

Last, a SAW resonator was fabricated which can be tuned electrically via the control voltage V_{piezo}. We demonstrated that the tuning mechanism works, as the transmission maximum can be varied via the control voltage. The tuning range is larger for the 860 MHz passband than for 172 MHz, as the estimated variation in the delayline length of about 2.7 μm corresponds to almost one wavelength at 860 MHz, but only a fifth of a wavelength at 172 MHz.

The shown results lay the foundation for further ADFMR experiments, using tuneable SAW resonators instead of simple delaylines. Thereby, it seems reasonable to use a piezoelectric actuator with a higher maximum stroke in order to extend the tuning range and to guarantee an optimal constructive interference of the resonator mode independent of the resonator load.

Chapter 5

Summary and outlook

In this thesis, resonant magnon-phonon coupling in ferromagnetic thin films was investigated experimentally and theoretically. In addition, a tuneable SAW resonator was designed, fabricated and characterized for future ADFMR experiments with standing instead of travelling waves. This chapter summarizes the work done during this thesis and its main results, and gives an outlook on further studies which are based on the present results.

5.1 Summary

In Chapter 1, a detailed theory of SAW propagation was given, which holds for any piezoelectric crystal and arbitrary crystal cuts. Based on the material parameters of the crystal, i. e. its stiffness tensor, piezoelectric tensor, dielectric tensor and its density, the particular type of SAW, its displacement components and the induced strains as well as its propagation speed can be calculated. The effects of the surface boundary condition – free or metallized surface – on the SAW mode were demonstrated. Besides, it was shown that on 36°YX-$LiTaO_3$, two qualitatively different surface wave types, Rayleigh and shear-horizontal wave, can be excited. All presented calculation results agree perfectly with literature data.

Chapter 2 introduced three approaches to model ADFMR. The LLG approach is a simple but physically very instructive model. It allows to calculate the power absorption by ADFMR and explains the main characteristic features of ADFMR: the four-fold symmetry, which is in contrast to conventional FMR, the qualitative difference between Rayleigh and SH wave driven FMR and the symmetry break due to non-diagonal strain components. The backaction model takes the effects of ADFMR

on the acoustic wave in the ferromagnetic film into consideration and thus allows to determine the complex transmission parameter of the wave. The backaction model could be shown to be consistent with the LLG model, but it only holds for small magnetoelastic interaction strength. The SAW model, finally, extends the backaction model and quantitatively describes the coupled system of a SAW, propagating on the piezoelectric crystal, together with the acoustic wave and the magnetization precession in the FM. It includes the theory of SAW propagation introduced in Chap. 1, and thus inherently considers the different wave types, depending on the used piezoelectric crystal.

Chapter 3 dealt with the experimental study of ADFMR and the comparison of theory and experiment. First, the used samples, the experimental setup and the processing of the measured data were explained. Second, an extensive study of Rayleigh wave driven FMR on YZ-$LiNbO_3$ was shown, including different orientations between external magnetic field and SAW propagation direction as well as three different SAW frequencies. Such a systematic investigation of ADFMR has never before been performed. The experimental data were compared to simulation results, obtained by the LLG and backaction model. It was demonstrated that theory and experiment agree qualitatively and quantitatively. Besides, it was shown that all three ADFMR models are consistent to each other and suited to describe the observed ADFMR characteristics quantitatively. Furthermore, the effects of the SAW type on the ADFMR signature were investigated. To this end, a ADFMR sample on 36°YX-$LiTaO_3$ was fabricated and characterized, in order to be able to excite two different wave types, Rayleigh and shear-horizontal wave, on one and the same sample. The measured ADFMR signatures confirm the theoretical predictions from Chap. 2 and clearly demonstrate the validity of the presented models and the current understanding of ADFMR. However, shear wave driven FMR experiments also showed some interesting features which should be studied in more detail in future experiments.

In Chapter 4, the concept of a mechanically tuneable SAW resonator was introduced. Preliminary experiments with a flipchip delayline and a tuneable delayline showed the functionality of the flipchip design and the tuning assembly, which allows a voltage-controlled change of the acoustic length of the delayline. Based on that, the tuneable resonator was introduced and characterized. The effects of the externally applied control voltage on the transmission were investigated and it was shown that the resonator indeed can be tuned within the expected range. Thus, the foundation

for future ADFMR experiments with SAW resonators instead of simple delaylines are layed, promising an enhanced ADFMR signal as well as the possibility to excite and detect ADFMR with spatial resolution.

5.2 Outlook

Based on the presented results and the current state of the art concerning spin mechanics with SAWs, there are a lot of open questions and several ideas for further studies in order to extend the current understanding of ADFMR and spin mechanics in general. This section gives an outlook on future projects, together with some preliminary calculations.

Tuning SAW resonators via temperature

As mentioned in Chap. 4, a SAW resonator can be tuned by variation of temperature, as almost all material parameters, like stiffness constants, density and geometric dimensions, depend on temperature. For SAW applications, we are particularly interested in the influence of temperature on the propagation time of the SAW pulse. Assuming a distance l between source and receiver IDT, the propagation time (*delay*) of the SAW pulse is $T = l/v$ with the speed of sound v. Variation of the temperature Θ does not only affect v but also the length l of the delayline due to thermal expansion of the crystal. Thus, the *temperature coefficient of delay* is given by [25]

$$\alpha_T := \frac{1}{T}\frac{\partial T}{\partial \Theta} = \frac{1}{l}\frac{\partial l}{\partial \Theta} - \frac{1}{v_0}\frac{\partial v_0}{\partial \Theta} \; . \tag{5.1}$$

Literature values α_T for commonly used SAW crystals can be found, e. g., in [25,31,58].

For ADFMR applications, we have to be able to tune the resonator by at least one wavelength, corresponding to $\Delta T \geq \tilde{T}$, where $\tilde{T} = 1/\nu$ is the period of the oscillation and ν denotes the SAW frequency. In first-order approximation, the temperature coefficient of delay becomes

$$\alpha_T := \frac{1}{T}\frac{\partial T}{\partial \Theta} \approx \frac{1}{T}\frac{\Delta T}{\Delta \Theta} \; . \tag{5.2}$$

Solving this for $\Delta\Theta$ yields

$$\Delta\Theta \approx \frac{1}{\alpha_T}\frac{\Delta T}{T} \; . \tag{5.3}$$

Using $\alpha_T = 9.4 \times 10^{-5}/°C$ [25], $\nu = 1\,\mathrm{GHz}$ and $T = 0.4\,\mu\mathrm{s}$ (corresponding to a $l \approx 1.4\,\mathrm{mm}$) for the typical SAW delayline on YZ-$LiNbO_3$ used in this thesis, we get $\Delta\Theta \approx 27°C$.

As $T \propto l$, the needed temperature variation $\Delta\Theta$ can even be reduced by using a longer delayline of about 6 mm. Then, $\Delta\Theta \approx 6°C$ would be sufficient to tune the resonator by at least one period $\tilde{T}$.

To realize this tuning method in a SAW resonator, the sample has to be mounted on a heating element (Peltier element or Joule heating), which is supplied by an adjustable current source. The transmission is measured with a microwave diode or a vector network analyser. In order to establish an *auto-calibrating SAW resonator*, one could implement a feed-back control loop which uses the measured transmission as a function of the heating current to find the ideal working point at which the transmission of the SAW resonator reaches its maximum.

ADFMR with standing waves

Having shown the functionality of a tuneable SAW resonator, one could perform ADFMR experiments with standing instead of travelling waves[1]. This would allow to *locally* excite FMR, with the spatial resolution given by the SAW wavelength, which is in the order of microns. To this end, the rectangular ferromagnetic film has to be replaced by a meander-like structure in order to account for the wavelength of the standing resonator mode. In contrast to present experiments, where a uniform precession motion was excited in good approximation, one could then selectively excite standing spin wave modes, whose wavelength is given by the standing resonator mode. Thereby, the ferromagnetic exchange interaction, which was negligible up to now, becomes relevant, giving access to a vast and interesting parameter space.

[1] In the case of the mechanically tuneable resonator presented in Chap. 4, the ferromagnetic film can be deposited on the bridge substrate. This allows a very easy investigation of different ferromagnets or the influence of the thickness of the film on the ADFMR signal, as only the bridge substrate has to be changed, while the rest of the assembly remains untouched. It would be reasonable, however, to improve the layout of the tuneable resonator so that the exact positioning of the bridge crystal and the contact pressure can be adjusted using micrometer screws or a XYZ stage.

AC spin pumping

Up to now, spin pumping experiments focused on the detection of DC spin currents [73–76]. Nevertheless, a simple calculation based on the LLG model shows that in addition to the DC spin current, an AC spin current has to occur as well. To derive this, we start with the standard term for the spin current density, which is excited by magnetization precession at a normal metal/ferromagnet interface [17, 77],

$$j_\mathrm{s}\boldsymbol{s} = \frac{\hbar}{4\pi}\mathrm{Re}(g^{\uparrow\downarrow})\left[\boldsymbol{m}\times\frac{\partial\boldsymbol{m}}{\partial t}\right], \tag{5.4}$$

where j_s is the spin current density with polarisation $\boldsymbol{s}$, and $g^{\uparrow\downarrow}$ is the spin mixing conductance [78].

In the $(x_1x_2x_3)$ coordinate system, the magnetization precession can be written as[2]:

$$\boldsymbol{m} = \begin{pmatrix} m_1^0\cos(kx-\omega t) \\ m_2^0\sin(kx-\omega t) \\ 1 \end{pmatrix}. \tag{5.5}$$

Substituting this into Eq. (5.4) yields

$$j_\mathrm{s}\boldsymbol{s} = \frac{\hbar}{4\pi}\mathrm{Re}(g^{\uparrow\downarrow})\,\omega\begin{pmatrix} m_2^0\sin(kx-\omega t) \\ m_1^0\cos(kx-\omega t) \\ -m_1^0m_2^0 \end{pmatrix}. \tag{5.6}$$

Thus, the DC spin current is given by

$$j_\mathrm{s}^\mathrm{DC} \equiv (j_\mathrm{s}\boldsymbol{s})_3 \propto \omega m_1^0 m_2^0, \tag{5.7}$$

while the AC components of the spin current are[3] (cf. [79])

$$j_\mathrm{s}^{\mathrm{AC},1} \equiv (j_\mathrm{s}\boldsymbol{s})_1 \propto \omega m_2^0 \qquad \text{and} \qquad j_\mathrm{s}^{\mathrm{AC},2} \equiv (j_\mathrm{s}\boldsymbol{s})_2 \propto \omega m_1^0. \tag{5.8}$$

[2] As we are interested in product terms of m_1 and m_2 here, we have to use the physically relevant real part of $m_{1,2} = m_{1,2}^0\exp(ikx - i\omega t)$ instead of the commonly used complex exponential function. We assume m_1 and m_2 to be out of phase by $\pi/2$, so the real parts of m_1 and m_2 are proportional to cosine and sine of $kx - \omega t$.

[3] For simplicity, we neglect the x- and t-dependence here and only consider the amplitudes of the AC spin current components.

Assuming a precession cone angle of $\Theta_{\mathrm{res}} = 1°$ (cf. [75, 76]), the magnetization amplitude is $m_{1,2}^0 \approx \sin(\Theta_{\mathrm{res}}) = 0.017$. Then, the ratio between the amplitudes of AC and DC spin current is

$$\frac{j_{\mathrm{s}}^{\mathrm{AC},1}}{j_{\mathrm{s}}^{\mathrm{DC}}} = \frac{1}{m_1^0} \approx 10^2 \qquad \text{respectively} \qquad \frac{j_{\mathrm{s}}^{\mathrm{AC},2}}{j_{\mathrm{s}}^{\mathrm{DC}}} = \frac{1}{m_2^0} \approx 10^2. \tag{5.9}$$

Even if it is more complicated to measure rf than DC signals, it should be possible to detect the AC spin current experimentally, provided that one makes sure that the spatially and temporally oscillating AC signal does not average out, but is enhanced by constructive superposition. To this end, one could use, e. g., the above mentioned meander structure instead of a simple rectangular ferromagnetic film.

If the magnetization precession is assumed to be elliptic instead of circular, and if we consider second-order effects, we also get an AC spin current proportional to $\cos(3kx - 3\omega t)$. This spin current, however, is of the order of $\omega m_{1,2}^3$ and therefore presumably beyond the experimental resolution limit.

Compared to conventional spin pumping via externally driven FMR [74, 75, 77], acoustic spin pumping [76] has a decisive advantage: As the propagation speed of the SAW, i. e. the speed of sound, is about five orders of magnitude lower than the speed of light, the acoustic spin pumping signal can be separated from the electromagnetic crosstalk in time domain using short microwave pulses of about 300 ns, as shown by Weiler *et al.* [76]. In this way, rectification effects and induced AC voltages due to the high microwave power input can be excluded, which is not possible in conventional FMR. This should allow to detect even a tiny AC spin pumping signal at the SAW frequency ν in spite of the high-power input microwave which oscillates at the same frequency.

Unconventional SAW excitation and detection methods

In most applications, SAWs are excited using IDTs on piezoelectric crystals, as this method is comparatively efficient and easy to realize. Besides, SAWs can be generated with short laser pulses directed onto a polished crystal surface [23]. This allows to excite a broad band of SAW frequencies, in contrast to the narrowband IDT response function (cf. [23]). Furthermore, the restriction to specific SAW passbands is dropped as the main SAW frequency is given by the pulse length of the laser which can be

varied.

As an analogue detection mechanism, Fabry-Perot interferometry can be used to measure the normal displacement of the SAW optically. Preliminary experiments using an interferometer built by R. Holländer [80] have already been performed at the Walther-Meissner-Institut. Such an optical ADFMR detection method would be much more reliable than the SAW detection by IDTs, as it allows a direct access to magnitude and phase of the SAW. Besides, interferometry can be used to measure the amplitude of the SAW in a resonator, and thus prove the formation of standing waves and the functionality of the tuning mechanism.

ADFMR with other ferromagnetic materials

Besides conventional ferromagnets like nickel, cobalt or iron, the ADFMR studies could be extended on ferromagnetic insulators like yttrium iron garnet (YIG) or magnetic semiconductors like gallium manganese arsenide (GaMnAs). Both materials play an important role in the field of spintronics: As it is electrically isolating, YIG allows the excitation of pure spin currents without a charge transport, which opens the path for the discovery of new spin-related phenomena (see e. g. [81]). GaMnAs is known to change its crystal structure and its magnetic anisotropy with varying temperature, which should yield a temperature-dependent characteristic ADFMR signature.

ADFMR at higher frequencies

For a systematic study of the damping parameter a, it would be favorable to perform ADFMR experiments at higher frequencies. In particular, it would be interesting to reach a frequency range which is comparable to the one of conventional FMR. This would allow a direct comparison of anisotropy parameters and damping mechanisms in acoustically driven and conventional FMR.

SAWs with a frequency of some GHz can be excited using short laser pulses, as mentioned above, but also via IDTs with a structure size in the sub-micron range. Such structures can be fabricated using electron-beam lithography.

In conclusion, a wealth of promising ideas for future projects and further studies in the field of spin mechanics in ferromagnets just awaits exploration.

Appendix A

Determination of the superposition coefficients A_α and B_α in the surface acoustic wave model

As described above, the interface and boundary conditions Eqs. (2.34) to (2.37) form a homogeneous system of linear equation in the superposition coefficients A_α and B_α, which can be written in matrix form,

$$\begin{pmatrix} M_{11} & M_{12} & \cdots & M_{1,10} \\ M_{21} & & & \\ \vdots & & \ddots & \\ & & & \\ \vdots & & & \\ M_{10,1} & & & \end{pmatrix} \begin{pmatrix} A_1 \\ \vdots \\ A_4 \\ B_1 \\ \vdots \\ B_6 \end{pmatrix} = 0, \tag{A.1}$$

where the matrix coefficients $M_{ij} = M_{ij}(\beta)$, given by Eqs. (2.34) to (2.37), depend on the wave number β. To get a non-trivial solution of Eq. (A.1), $\det(M)$ has to vanish. Because of numerical errors, however, it is impossible to solve $\det[M(\beta)] = 0$ directly. Instead, an iterative algorithm can be applied which minimizes $\det(M)$ as a function of β.

In practice, however, one deals with badly conditioned matrices M_{ij}, as some of the $\gamma^\alpha_{\mathrm{Ni}}$ can be quite similar or even equal, which reduces the number of independent equations and in this way the rank of M, too. In this case, $\det[M(\beta)] = 0$ does not necessarily correspond to a non-zero solution vector $(A_1, \ldots, A_4, B_1, \ldots, B_6)^T$ any more and is therefore unsuitable to find the correct β. A better way to solve Eq. (A.1)

is to fix one of the superposition coefficients, e. g. set $A_1 = 1$, and solve the remaining inhomogeneous linear system

$$\begin{pmatrix} M_{12} & M_{13} & \cdots \\ M_{22} & \ddots & \\ \vdots & & \\ M_{10,2} & & \end{pmatrix} \begin{pmatrix} A_2 \\ \vdots \\ \vdots \\ B_6 \end{pmatrix} = - \begin{pmatrix} M_{11}A_1 \\ M_{21}A_1 \\ \vdots \\ M_{10,2}A_1 \end{pmatrix} \tag{A.2}$$

with a least-squares algorithm. We define the normalized residual

$$\mathcal{R} := \frac{|M\boldsymbol{w}|}{|\boldsymbol{w}|}, \tag{A.3}$$

where $|\boldsymbol{a}|$ denotes the norm of an arbitrary vector $\boldsymbol{a}$ and $\boldsymbol{w}$ is the vector of coefficients

$$\boldsymbol{w} := (1, A_2, A_3, A_4, B_1, \ldots, B_6)^T. \tag{A.4}$$

The residual $\mathcal{R}$ is a measure of how well the interface and boundary conditions, described by Eq. (A.1), can be fulfilled for a given wave number β. The ideal β can be found by minimizing $\mathcal{R}(\beta)$ iteratively. As each iteration step requires the calculation of the matrix coefficients M_{ij}, determined by the boundary and interface conditions, and the iterative solution of the inhomogeneous linear system Eq. (A.2), the numerical costs of the algorithm are rather high. Nevertheless, the complexity of the involved equations and especially the contributions of magnetoelastic coupling in these equations do not allow an analytical solution of the SAW model, such that numerical approaches are the method of choice.

Appendix B

Effective reduction of the magnetoelastic coupling constant b_1 by surface pinning of electron spins

Besides shape and uniaxial anisotropy, in thin films other anisotropy contributions can arise. In particular, there is the so-called *surface anisotropy*, which can fix the electron spins at the surface or partially hinder their precession motion [18,19,63,82]. This phenomenon is known as *surface pinning* and has been investigated in detail, as it is crucial for the excitation of spin waves in a ferromagnet [18, 19, 49, 82–85]. In a rather simple model, the pinning forces only act on those electrons which are located directly at the surface of the FM. Then, the pinning condition can phenomenologically be written as [49, 63]

$$\frac{\partial \boldsymbol{m}}{\partial \boldsymbol{n}} + \frac{K_\mathrm{s}}{A}\boldsymbol{m} = 0, \tag{B.1}$$

where $\boldsymbol{n}$ is the outward pointing surface normal, K_s is a surface anisotropy constant, and $A := M_\mathrm{s} D_\mathrm{s}/2$ is an exchange parameter. For $K_s = \infty$, the electrons are completely pinned, which means $\partial \boldsymbol{m}/\partial t = 0$ at the surface, whereas $K_s = 0$ yields the standard boundary condition $\partial \boldsymbol{m}/\partial \boldsymbol{n} = 0$ without any pinning [49].

Due to the ferromagnetic exchange interaction, not only the electrons at the surface but also the neighbouring electrons are affected by the pinning forces. The relevant lengthscale is given by the exchange length $\lambda_\mathrm{ex} = (2A/\mu_0 M_\mathrm{s}^2)^{1/2}$ [83]. With $M_\mathrm{s} = 370\,\mathrm{kA/m}$ [53] and $D_\mathrm{s} = 2.1 \times 10^{-17}\,\mathrm{Tm}^2$ [64] as above, we get $A = 3.9 \times 10^{-12}\,\mathrm{Jm}^{-1}$ and $\lambda_{ex} = 6.7\,\mathrm{nm}$. This means that for thin layers (e. g. $t_\mathrm{Ni} = 50\,\mathrm{nm}$), as those used in the ADFMR experiments, surface anisotropies can definitely play a role and reduce the magnetization precession. For bulk FM or thick layers, however, surface

pinning can usually be neglected if the exchange length is small compared to the lateral dimensions of the FM.

To consider pinning forces in ADFMR exactly is rather complicated as the algebraic equations of motion as well as the boundary and interface conditions, derived in Chap. 2, then would turn into a system of coupled differential equations, with the independent variable z. This would involve a much higher numerical effort which exceeds common computational capacities.

Nevertheless, the effects of spin pinning can phenomenologically be taken into account by a reduction of the magnetoelastic coupling of acoustic wave and magnetization motion. To this end, we introduce an *effective magnetoelastic coupling constant* $\tilde{b}_1$ with $\tilde{b}_1 < b_1$.

In order to make a rough estimate of the ratio $\tilde{b}_1/b_1$, we perform conventional FMR calculations with and without pinning boundary conditions and study the effects of pinning on the magnetization precession amplitude.

We start with the Landau-Lifshitz-Gilbert equation (Eq. 2.1), including the exchange term:

$$\partial_t \boldsymbol{m} = -\gamma \boldsymbol{m} \times \mu_0 \boldsymbol{H}_{\text{eff}} + a\boldsymbol{m} \times \partial_t \boldsymbol{m} - \gamma D_{\text{s}} \boldsymbol{m} \times \Delta \boldsymbol{m}, \tag{B.2}$$

where γ, a and D_{s} denote the gyromagnetic ratio, the damping parameter and the ferromagnetic exchange constant, respectively. $\boldsymbol{m}$ is the magnetization, normalized to the saturation magnetization M_{s}.

For simplicity, we use the sample coordinate system (x, y, z) for the following calculations instead of the (x_1, x_2, x_3) frame of reference introduced in Chap. 2. We assume a ferromagnetic thin film which is infinitely extended in the xy-plane, with its surfaces at $z = 0$ and $z = t_{\text{Ni}}$. Further, we assume in-plane configuration and neglect shape and uniaxial anisotropy, so that the equilibrium direction of the magnetization, $\boldsymbol{m}_0$, is parallel to the static external magnetic field $\boldsymbol{H}_0$. Without loss of generality, we set $\boldsymbol{H}_0 \parallel \boldsymbol{m}_0 \parallel \boldsymbol{x}$. The external magnetic driving field $\boldsymbol{h}_{\text{rf}}$ is taken to be along $\boldsymbol{z}$. Then, the total external magnetic field is given by

$$\boldsymbol{H} = \begin{pmatrix} H_0 \\ 0 \\ h^0_{\text{rf}} \exp(i\omega t) \end{pmatrix}. \tag{B.3}$$

As the wavelength of the driving field is large compared to the sample size[1], $\boldsymbol{h}_{\mathrm{rf}}$ can be taken x-independent.

As above, we assume the magnetization precession amplitude to be small compared to the saturation magnetization, i. e. $m_{1,2} \ll 1$. Thus, we can write

$$\boldsymbol{m} = \begin{pmatrix} 1 \\ m_y^0 \exp(i\omega t) \\ m_z^0 \exp(i\omega t) \end{pmatrix}. \tag{B.4}$$

We now consider two borderline cases: First, the *unpinned case*, where we neglect any surface anisotropy. Then, there are no pinning forces acting on the electron spins at the surface, which leads to a uniform precession motion of the magnetization $\boldsymbol{m}$. As the exchange energy $\gamma D_{\mathrm{s}} \boldsymbol{m} \times \Delta \boldsymbol{m}$ vanishes for uniform precession, Eq. (B.2) becomes algebraic and can be solved analytically.

In the following, we a assume $\mu_0 H_0 = 5\,\mathrm{mT}$ for the static magnetic field and $\mu_0 h_{\mathrm{rf}}^0 = 35\,\mu\mathrm{T}$ for the driving field[2], with a microwave frequency of $\nu = \omega/2\pi = 1.55\,\mathrm{GHz}$. Furthermore, we set $t_{\mathrm{Ni}} = 50\,\mathrm{nm}$ and $a = 0.1$ as above (see Chap. 3) and use $\gamma = 2.185\mu_{\mathrm{B}}/\hbar$ [55] and $D_{\mathrm{s}} = 2.1 \times 10^{-17}\,\mathrm{Tm}^2$ [64].

Defining the magnetization precession amplitude[3]

$$m_{\mathrm{p}} := \left|(m_y, m_z)^T\right|, \tag{B.5}$$

the calculation for the unpinned case yields $m_{\mathrm{p}}^{\mathrm{unpinned}} = 7.3 \times 10^{-4}$.

In the *fully pinned case*, we assume the pinning forces to be strong enough to cause $m_y^0 = m_z^0 = 0$ at the boundaries of the film, i. e. at $z = 0$ and $z = t_{\mathrm{Ni}}$. Solving the coupled differential equation system Eq. (B.2) numerically using the above listed parameters, we get a nearly parabolic z-dependence of the magnetization precession amplitude m_{p}, as plotted in Fig. B.1.

The average precession amplitude, given by

$$m_{\mathrm{p,av}} = \frac{1}{t_{\mathrm{Ni}}} \int_0^{t_{\mathrm{Ni}}} m_{\mathrm{p}}(z)\mathrm{d}z, \tag{B.6}$$

[1] Due to the high speed of light, we get a wavelength of about 30 cm at a microwave frequency of 1 GHz.

[2] The static and driving field strength have been chosen similar to the respective values obtained in the ADFMR experiments (cf. Fig. 2.2 and Chap. 3).

[3] As above, $|\cdot|$ denotes the (Euclidian) vector norm.

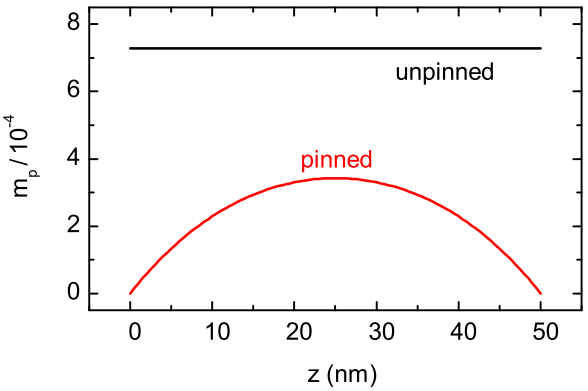

Figure B.1: Calculated magnetization precession amplitude m_p for a $t_\mathrm{Ni} = 50\,\mathrm{nm}$ thin nickel film, assuming free (black line) resp. fully pinned spins (red line). The definition of m_p and the calculation parameters are given in the text.

is then $m_\mathrm{p,av}^\mathrm{pinned} = 2.3 \times 10^{-4}$ for the fully pinned case.

Hence, we get a reduction of the average magnetization precession amplitude m_p by a factor $m_\mathrm{p,av}^\mathrm{pinned}/m_\mathrm{p}^\mathrm{unpinned} \approx 0.3$.

As explained above, in the SAW model, the reduction of the magnetization precession amplitude is phenomenologically modelled by introducing an effective magnetoelastic coupling constant $\tilde{b}_1 < b_1$. To estimate the ratio $\tilde{b}_1/b_1$, we make use of the LLG model: According to Eq. (2.12), we have the proportionality $P_\mathrm{abs} \propto \boldsymbol{h}^\dagger \chi \boldsymbol{h}$. Together with $(m_1, m_2)^T \propto \boldsymbol{h}$ (cf. Eq. (2.10)), we get

$$P_\mathrm{abs} \propto |(m_1, m_2)^T|^2. \tag{B.7}$$

On the other hand, Eqs. (2.8) and (2.9) show that $h_{1,2} \propto b_1$. As the susceptibility tensor χ is independent of b_1, this results in

$$P_\mathrm{abs} \propto \boldsymbol{h}^\dagger \chi \boldsymbol{h} \propto b_1^2, \tag{B.8}$$

if we assume $m_1 \approx m_2 =: m_{1,2} = m_\mathrm{p}/\sqrt{2}$.

Comparing Eqs. (B.7) and (B.8) yields

$$m_{1,2} \propto b_1. \tag{B.9}$$

Thus, an effective reduction of the magnetization precession amplitude m_p by 70%,

as estimated above, can be modelled by a reduction of b_1 by the same percentage,

$$\tilde{b}_1 \approx 0.3\, b_1 \approx 7\,\mathrm{T}, \tag{B.10}$$

as $b_1 = 23\,\mathrm{T}$ (see Sect. 2.3.3). Of course, such a reduction of the magnetoelastic coupling constant is only a rough, phenomenological approximation of the real effects of surface pinning. Moreover, the pinned and the unpinned case, which have been studied here, are two extreme cases, whereas in reality, the spins can be partially pinned so that the effective magnetoelastic coupling constant should lie between the minimum $\tilde{b}_{1,\mathrm{min}} \approx 7\,\mathrm{T}$ and the maximum $\tilde{b}_{1,\mathrm{max}} = b_1 = 23\,\mathrm{T}$.

Nevertheless, the values chosen in the ADFMR calculations, which were $\tilde{b}_1 = 8\,\mathrm{T}$ for the Rayleigh wave driven FMR on $LiNbO_3$ (cf. Sect. 3.4) and $\tilde{b}_1 = 14\,\mathrm{T}$ for the Rayleigh and SH wave driven FMR on $LiTaO_3$ (cf. Sect. 3.5), agree well with the above estimate.

Appendix C

Samples

In this work, several samples for ADFMR measurements have been made using optical lithography, e-beam evaporation and liftoff. Besides, pure delaylines, consisting of a pair of IDTs have been fabricated and characterized. The tuneable delayline and the tuneable resonator presented in this thesis have been fabricated and assembled together with A. Späh [69].

A list of all working samples is given in Tabs. C.1, C.2 and C.3. The used lithography structures are shown in Fig. C.1, and their geometrical dimensions can be found in Tab. C.4.

Table C.1: Delaylines fabricated during this work

Name	**Substrate (Size in mm^2)**	**Structure**	**Material (Thickness in nm)**	**Measured?**
LNO-Y-1	YZ-$LiNbO_3$ (6x9)	MP #9	Cr (3) / Al (70)	✓ > **Flipchip delayline:** S-parameters, various bridge crystals (YZ-$LiNbO_3$, air gap, MgO (100), YX-$LiNbO_3$, GGG (111) and MgO (001))
LNO-Y-2				✓ S-parameters (VNA)
LNO-Y-3			Al (70)	✓ Transmission (dB) at 1st, 3rd, 5th, 7th and 9th harmonics
LNO-Y-4		FG #55&56		✓ Transmission (dB) at 1st, 5th and 9th harmonics
LNO-Y-9		MP #8		✓
LNO-Y-10				✓ > **Tuneable Delayline:** S-parameters overview and detailed (as a function of V_{piezo})
LNO-Y-12				✓ Kerr microscopy (Regensburg)
LNO-Y-13				✓ Kerr microscopy (Regensburg); S-parameters (VNA), overview and detailed (as a reference for tuneable delayline)
LTO-36Y-1	36°YX-$LiTaO_3$ (6x10)	FG #55&56	Al (70)	✓ S-parameters (VNA)
LTO-36Y-6		MP #9	Cr (3) / Al (70)	✓ S-parameters (VNA)
LTO-36Y-8				✗
LTO-36Y-9				✗
LTO-36Y-13		MP #8		✓ S-parameters (VNA)
LNO-128Y-2	128°YX-$LiNbO_3$ (6x10)	FG #55&56	Al (70)	✓ S-parameters (VNA)
LNO-128Y-5		MP #9	Cr (3) / Al (70)	✓ > Flipchip delayline: S-parameters
LNO-128Y-6				✓ Transmission and polarisation microscopy
LNO-128Y-7				✓ S-parameters (VNA)
LNO-128Y-10		MP #8		✗
LNO-128Y-11				✗

Table C.2: ADFMR samples fabricated during this work

Name	**Substrate (Size in mm^2)**	**1st lithography and evaporation**		**2nd lithography and evaporation**		**Measured?**
		Structure	**Material (Thickness in nm)**	**Structure**	**Material (Thickness in nm)**	
LNO-128Y-3	128°YX-$LiNbO_3$ (6x10)	MP #9	Cr (3) / Al (70)	MP #5	Ni (50)	✓ S-parameters (VNA), SAW-FMR in-plane @200 MHz and 979 MHz
LNO-128Y-4					Fe (50) / Au (10)	✓ S-parameters (VNA)
LNO-128Y-9		MP #8			Ni (50)	✓ Kerr microscopy (Regensburg)
LNO-Y-11	YZ-$LiNbO_3$ (6x9)	MP #8	Al (70)	MP #5	Ni (50)	✗
LTO-36Y-14	36°YX-$LiTaO_3$ (6x10)	MP #8	Cr (3) / Al (70)	MP #5	Ni (50)	✓ **SAW-FMR in-plane and out-of-plane**

LNO-128Y-4: tried to measure SAW-FMR, IP and OOP2, but no field-dependence observed.

Table C.3: Resonators fabricated during this work

Name	**Substrate (Size in mm^2)**	**Structure**	**Material (Thickness in nm)**	**Measured?**
LNO-Y-7	YZ-$LiNbO_3$ (6x9)	JM #1	Al (70)	✗
LNO-Y-8		JM #2 (two times)		✗
LNO-Y-14	YZ-$LiNbO_3$ (6x7)	One half of JM #1 each		✗
LNO-Y-15				✓ > **Tuneable resonator:** S-parameters overview and detailed (as a function of V_{piezo})
LNO-Y-17				

Figure C.1: Lithography structures used for the samples listed in Tabs. C.1, C.2 and C.3.

Name	Structure	Dimensions
JM #1	Two-port resonator	$p = 2p' = 20\,\mu\text{m}$, $w_{\text{IDT}} = w_{\text{Res}} = 500\,\mu\text{m}$, $N = 20$, $N' = 200$, $d_{\text{IDT}} = 1.4\,\text{mm}$
JM #2	Two-port resonator	$p = 2p' = 20\,\mu\text{m}$, $w_{\text{IDT}} = w_{\text{Res}} = 500\,\mu\text{m}$, $N = 20$, $N' = 200$, $d_{\text{IDT}} = 1.4\,\text{mm}$
FG #55	Pair of IDTs	$p = 12\,\mu\text{m}$, $w_{\text{IDT}} = 500\,\mu\text{m}$, $N = 50$, $d_{\text{IDT}} = 1.8\,\text{mm}$
FG #56	Pair of IDTs	$p = 20\,\mu\text{m}$, $w_{\text{IDT}} = 500\,\mu\text{m}$, $N = 30$, $d_{\text{IDT}} = 1.8\,\text{mm}$
MP #5	Rectangle	$l_{\text{Ni}} = 1.2\,\text{mm}$, $w_{\text{Ni}} = 4.0\,\text{mm}$
MP #8	Pair of IDTs	$p = 20\,\mu\text{m}$, $w_{\text{IDT}} = 500\,\mu\text{m}$, $N = 30$, $d_{\text{IDT}} = 5.8\,\text{mm}$
MP #9	Pair of IDTs	$p = 20\,\mu\text{m}$, $w_{\text{IDT}} = 500\,\mu\text{m}$, $N = 30$, $d_{\text{IDT}} = 6.8\,\text{mm}$

Table C.4: Design parameters for the lithography structures shown in Fig. C.1. p and p' denote the periodicity of IDTs and reflective grating, respectively (cf. Fig. 3.2), w_{IDT} and w_{Res} are the width of IDTs and reflective grating. N and N' denotes the number of IDT finger pairs and the number of grating stripes, respectively, and d_{IDT} is the effective distance between the IDTs (see Fig. 3.3).

Bibliography

[1] W. Gerlach and O. Stern, Zeitschrift für Physik A (Hadrons and Nuclei) **9**, 349 (1922).

[2] W. Gerlach and O. Stern, Zeitschrift für Physik A (Hadrons and Nuclei) **9**, 353 (1922).

[3] W. Pauli, Physical Review **58**, 716 (1940).

[4] P. Kusch and H. M. Foley, Physical Review **74**, 250 (1948).

[5] W. H. Louisell, R. W. Pidd, and H. R. Crane, Physical Review **94**, 7 (1954).

[6] F. Bloch, W. W. Hansen, and M. Packard, Physical Review **69**, 127 (1946).

[7] F. Bloch, Physical Review **70**, 460 (1946).

[8] E. M. Purcell, H. C. Torrey, and R. V. Pound, Physical Review **69**, 37 (1946).

[9] G. Binasch, P. Grünberg, F. Saurenbach, and W. Zinn, Physical Review B **39**, 4828 (1989).

[10] M. N. Baibich, J. M. Broto, A. Fert, F. N. Van Dau, F. Petroff, P. Etienne, G. Creuzet, A. Friederich, and J. Chazelas, Physical Review Letters **61**, 2472 (1988).

[11] M. Johnson and R. H. Silsbee, Physical Review Letters **55**, 1790 (1985).

[12] S. Datta and B. Das, Applied Physics Letters **56**, 665 (1990).

[13] S. T. B. Goennenwein, Europhysics News **41**, 17 (2010).

[14] S. T. B. Goennenwein and G. E. W. Bauer, Nature Nanotechnology **7**, 145 (2012).

[15] I. Appelbaum, B. Huang, and D. J. Monsma, Nature **447**, 295 (2007).

[16] M. Weiler, L. Dreher, C. Heeg, H. Huebl, R. Gross, M. S. Brandt, and S. T. B. Goennenwein, Physical Review Letters **106**, 117601 (2011).

[17] L. Dreher, M. Weiler, M. Pernpeintner, H. Huebl, R. Gross, M. S. Brandt, and S. T. B. Goennenwein, arXiv:1208.0001 (2012).

[18] C. Kittel, Physical Review **73**, 155 (1948).

[19] C. Kittel, Physical Review **110**, 1295 (1958).

[20] K. Lakin and T. Joseph, *Ultrasonics Symposium, Proceedings*, 269–278 (1975).

[21] W. Tanski, *Ultrasonics Symposium, Proceedings*, 815–823 (1979).

[22] W. Tanski, IEEE Transactions on Sonics and Ultrasonics **26**, 93 (1979).

[23] E. A. Ash, *Rayleigh Wave Theory and Application* (Springer-Verlag, 1985).

[24] J. Bell, D.L.T. and R. Li, Proceedings of the IEEE **64**, 711 (1976).

[25] D. P. Morgan, *Surface-Wave Devices for Signal Processing* (Elsevier, 1991).

[26] B. A. Auld, *Acoustic Fields and Waves in Solids* (Krieger Pub Co, 1990).

[27] R. S. Weis and T. K. Gaylord, Applied Physics A (Solids and Surfaces) **37**, 191 (1985).

[28] *Lithium tantalate properties*, Roditi International Corporation Ltd. URL: http://www.roditi.com/SingleCrystal/Lithium-Tantalate/LiTaO3-Properties.html [accessed October 2012]

[29] L. Rayleigh, Proc. London Math. Soc. **17**, 4 (1885).

[30] C. K. Campbell, Proceedings of the IEEE **77**, 1453 (1989).

[31] M. Feldmann and J. Hénaff, *Surface acoustic waves for signal processing* (Artech House, 1989).

[32] F. Martin, M. I. Newton, G. McHale, K. A. Melzak, and E. Gizeli, Biosensors and Bioelectronics **19**, 627 (2004).

[33] M. J. Vellekoop, Ultrasonics **36**, 7 (1998).

[34] F. Herrmann, M. Weihnacht, and S. Buttgenbach, IEEE Transactions on Ultrasonics, Ferroelectrics and Frequency Control **48**, 268 (2001).

[35] M. Kadota, Japanese Journal of Applied Physics **44**, 4285 (2005).

[36] *Lithium tantalate datasheet*, Roditi International Corporation Ltd. URL: http://www.roditi.com/SingleCrystal/Lithium-Tantalate/LiTaO3-Wafers.html [accessed October 2012]

[37] S. Hunklinger, *Festkörperphysik* (Oldenbourg Verlag, 2009).

[38] R. Gross and A. Marx, *Festkörperphysik* (Oldenbourg Verlag, 2012).

[39] G. Kovacs, M. Anhorn, H. E. Engan, G. Visintini, and C. C. Ruppel, *Ultrasonics Symposium, Proceedings*, 435–438 (1990).

[40] K. Nakamura, M. Kazumi, and H. Shimizu, *Ultrasonics Symposium, Proceedings*, 819–822 (1977).

[41] L. Landau and E. Lifshitz, Phys. Z. Sowjetunion **8** (1935).

[42] T. Gilbert, IEEE Transactions on Magnetics **40**, 3443 (2004).

[43] M. Weiler, *Magnon-Phonon Interactions in Ferromagnetic Thin Films*, Ph.D. thesis, Walther-Meissner-Institut der Bayerischen Akademie der Wissenschaften (2012).

[44] J. Xiao, A. Zangwill, and M. D. Stiles, Physical Review B **72**, 014446 (2005).

[45] D. D. Stancil and A. Prabhakar, *Spin Waves: Theory and Applications* (Springer, 2009).

[46] S. Chikazumi, *Physics of Ferromagnetism* (Oxford University Press, 2009).

[47] T. Kobayashi, R. C. Barker, J. L. Bleustein, and A. Yelon, Physical Review B **7**, 3273 (1973).

[48] C. Kittel, *Einführung in die Festkörperphysik* (Oldenbourg Verlag, 2005).

[49] C. E. Patton, Physics Reports **103**, 251 (1984).

[50] C. Bihler, W. Schoch, W. Limmer, S. T. B. Goennenwein, and M. S. Brandt, Physical Review B **79**, (2009).

[51] A. F. Mills, *Basic Heat and Mass Transfer* (Prentice Hall, New Jersey, 1999).

[52] M. Yamamoto, Physical Review **77**, 566 (1950).

[53] M. Weiler, A. Brandlmaier, S. Geprägs, M. Althammer, M. Opel, C. Bihler, H. Huebl, M. S. Brandt, R. Gross, and S. T. B. Goennenwein, New Journal of Physics **11**, 013021 (2009).

[54] E. Klokholm and J. Aboaf, Journal of Applied Physics **53**, 2661 (1982).

[55] A. J. P. Meyer and G. Asch, Journal of Applied Physics **32**, 330–333 (1961).

[56] H. Söde, *Surface Acoustic Waves at Ferromagnetic Piezoelectric Interfaces*, Bachelor's thesis, Walther-Meissner-Institut der Bayerischen Akademie der Wissenschaften (2009).

[57] C. Heeg, *Spin Mechanics at Radio Frequencies*, Diploma thesis, Walther-Meissner-Institut der Bayerischen Akademie der Wissenschaften (2010).

[58] C. Campbell, *Surface acoustic wave devices and their signal processing applications* (Academic Press, 1989).

[59] S. Datta, *Surface acoustic wave devices* (Prentice Hall, 1986).

[60] J. S. K. Manz, *Paramagnetische Resonanz mit akustischen Oberflächenwellen*, Diploma thesis, Walter Schottky Institut der Technischen Universität München (2010).

[61] W. Robbins, IEEE Transactions on Sonics and Ultrasonics **24**, 339 (1977).

[62] J. Walowski, M. D. Kaufmann, B. Lenk, C. Hamann, J. McCord, and M. Münzenberg, Journal of Physics D: Applied Physics **41**, (2008).

[63] R. E. Camley and D. L. Mills, Physical Review B **18**, 4821 (1978).

[64] R. Pauthenet, Journal of Applied Physics **53**, 8187 (1982).

[65] K. Honda and T. Terada, Philosophical Magazine Series 6 **13**, 36 (1907).

[66] E. W. Lee, Reports on Progress in Physics **18**, 184 (1955).

[67] A. Clark and H. Savage, IEEE Transactions on Sonics and Ultrasonics **22**, 50 (1975).

[68] R. A. Kellogg, *The Delta-E effect in Terfenol-D and its application in a tuneable mechanical resonator*, Master's thesis, Iowa State University (2000).

[69] A. Späh, *Abstimmbare Resonatoren für akustische Oberflächenwellen*, Bachelor's thesis, Walther-Meissner-Institut der Bayerischen Akademie der Wissenschaften (2012).

[70] Piezomechanik München GmbH, Dr. Lutz Pickelmann, *Low voltage co-fired multilayer stacks, rings and chips for actuation* (2011).

[71] A. Brandlmaier, *Magnetische Anisotropie in dünnen Schichten aus Magnetit*, Diploma thesis, Walther-Meissner-Institut der Bayerischen Akademie der Wissenschaften (2006).

[72] A. Brandlmaier, S. Geprägs, G. Woltersdorf, R. Gross, and S. T. B. Goennenwein, Journal of Applied Physics **110**, 043913 (2011).

[73] Y. Kajiwara, K. Harii, S. Takahashi, J. Ohe, K. Uchida, M. Mizuguchi, H. Umezawa, H. Kawai, K. Ando, K. Takanashi, S. Maekawa, and E. Saitoh, Nature **464**, 262 (2010).

[74] Y. Tserkovnyak, A. Brataas, and G. E. W. Bauer, Physical Review Letters **88**, (2002).

[75] F. D. Czeschka, L. Dreher, M. S. Brandt, M. Weiler, M. Althammer, I.-M. Imort, G. Reiss, A. Thomas, W. Schoch, W. Limmer, H. Huebl, R. Gross, and S. T. B. Goennenwein, Physical Review Letters **107**, 046601 (2011).

[76] M. Weiler, H. Huebl, F. S. Goerg, F. D. Czeschka, R. Gross, and S. T. B. Goennenwein, Physical Review Letters **108**, (2012).

[77] Y. Tserkovnyak, A. Brataas, and G. E. W. Bauer, Physical Review B **66**, 224403 (2002).

[78] O. Mosendz, J. E. Pearson, F. Y. Fradin, G. E. W. Bauer, S. D. Bader, and A. Hoffmann, Physical Review Letters **104**, 046601 (2010).

[79] H. Jiao and G. E. W. Bauer, AC Voltage Generation by Spin Pumping and Inverse Spin Hall Effect, to be published.

[80] R. Holländer, *Räumliche Untersuchung nanomechanischer Objekte mit Interferometrie*, Bachelor's thesis, Walther-Meissner-Institut der Bayerischen Akademie der Wissenschaften (2011).

[81] H. Nakayama, M. Althammer, Y.-T. Chen, K. Uchida, Y. Kajiwara, D. Kikuchi, T. Ohtani, S. Geprägs, M. Opel, S. Takahashi, R. Gross, G. E. W. Bauer, S. T. B. Goennenwein, and E. Saitoh, Spin Hall Magnetoresistance, to be published.

[82] J. A. Davis, Journal of Applied Physics **36**, 3520 (1965).

[83] R. D. McMichael and B. B. Maranville, Physical Review B **74**, (2006).

[84] C. Bayer, J. Jorzick, S. Demokritov, A. Slavin, K. Guslienko, D. Berkov, N. Gorn, M. Kostylev, and B. Hillebrands, *Topics in Applied Physics*, vol. 101, 57–103 (Springer Berlin / Heidelberg, 2006).

[85] H. Puszkarski, Progress in Surface Science **9**, 191 (1979).

Acknowledgment

There are several people without whom this thesis would not have been possible. In particular, I would like to thank:

Prof. Dr. Rudolf Gross, for giving me the possibility to accomplish this work at the Walther-Meissner-Institut.

Dr. Sebastian T. B. Gönnenwein, who convinced me to join the "Magnetiker" group in the first place, for his excellent supervision, his enthusiasm and a plenty of stimulating ideas. For the fascinating research I was allowed to participate, a lot of helpful advice, and the careful review of this thesis.

Dr. Mathias Weiler, who was my advisor during the past twelve months, for the great deal of time he spent with me, explaining me LabVIEW programs, discussing theoretical models and experimental methods, for introducing me to the lab and the experimental setup. For the experiments we made together, including the attempts to measure AC spin pumping, which have not been successful yet but taught me a lot about microwave equipment and techniques. For leaving me his ear with everlasting patience, and for lots of constructive and valuable suggestions concerning this thesis.

My bachelor student Alexander Späh, for fabricating and characterizing the samples shown in Chap. 4, his indispensable contribution to this thesis and for the time we spent together.

Lukas Dreher, for explaining me the theory of ADFMR, for valuable ideas and advice, for the joint work on ADFMR theory and simulations, and for his effort concerning the ADFMR manuscript.

Dr. Hans Hübl for advice concerning microwave experiments and for a lot of valuable ideas and fruitful discussions concerning ADFMR and AC spin pumping.

Prof. Dr. Martin Brandt, for interesting and instructive discussions at the "Walt(h)er-Stammtisch" and the "Walt(h)er-Seminar" and for valuable contributions to the work on ADFMR. In particular, I would like to thank him for being my mentor, leaving me his ear whenever I dropped by, and for a lot of helpful advice, as well as for several barbecue evenings at his home.

My colleagues in room 134, Dr. Matthias Althammer and Christoph Zollitsch, and the other members of the "Magnetiker" group, Dr. Matthias Opel, Dr. Stephan Geprägs, Sibylle Meyer, Johannes Lotze, Philipp Ross, Michael Schreier, Stephan Altmannshofer and Moritz Greifenstein, for discussions about physical and unphysical topics and for various support and advice concerning lab and office problems. I also want to mention those, who did the previous work on SAWs and ADFMR: Besides Mathias Weiler and Lukas Dreher, these are the former bachelor and diploma students Hajo Söde, Christian Heeg, Johannes Manz and Frederik Goerg.

Christian Schöppner (University of Duisburg-Essen) for a helpful discussion concerning the surface pinning of electron spins and its effects on the magnetization motion.

Elly Hoffmann and Max Häberlein for support concerning the clean room and the EVAP.

The diploma students of the "Magnetiker" group as well as Nikolai Bittner, Thomas Losinger and Zhaohai Jiang for a great time at the DPG Spring Meeting 2012.

The technical and administrative staff at the Walther-Meissner-Institut, in particular Tom Brenninger, for his tireless work on the deposition system and the EVAP and for valuable support concerning the operation of all the equipment.

My friends, for all the great moments in and outside the university, and for the time we spent together.

My parents, for giving me the opportunity to go to university and for standing behind me in all important decisions.

My girlfriend Carla for her endurance, her understanding and encouragement in any situation.